Damage tolerance and multi-scale simulation of novel 3D composites

Visrolia, Amit

Award date:
2014

Awarding institution:
University of Bath

Damage tolerance and multi-scale simulation of novel 3D composites

Amit Visrolia

A thesis submitted for the degree of Doctor of Philosophy

University of Bath
Department of Mechanical Engineering

November 2013

. . . . . .

Signed on behalf of the Faculty of Engineering and Design

For Dad.

Abstract

Composite materials are experiencing a huge expansion in use on high-value components for their high strength and low weight. To increase damage tolerance, complex architectures such as 3D weaving are being used. Existing analysis techniques are focussed on laminated composites, and are unable to capture the complex behaviour and realize the full potential of 3D weaved material. The aim of this study was to develop a technique by which a 3D weaved component could be simulated to determine damage intiation and growth, and understand the response of the structure. Multi-scale techniques have been employed to achieve this in a practical, accurate and efficient manner. A model has been produced by extending established 'layerwise' finite element methods used for laminated (1D/2D) composites in order to generate globally accurate displacements and selective locally accurate stresses, and combining with models to simulate delamination and transverse tow pullout. Additionally, asymptotic expansion homogenization models are used to resolve stresses to the tow scale, enabling an accurate assessment of damage accumulation at the micro-scale and the resulting effect at the component scale. The model has been implemented in MATLAB, and the constituent parts of the model have been validated against analytical, test and published data. It has been proven to produce good results at a lower computational cost or greater resolution than other equivalent models. The capability of the unified model has been demonstrated by simulating the failure process of a double cantilever beam constructed from a 3D weaved composite.

Acknowledgements

I gratefully acknowledge the contributions and guidance provided by my supervisor, Dr. Michele Meo.

I also gratefully acknowledge the funding provided for this work from Great Western Research, and funding and data provided by Qinetiq.

I am also indebted to all the friends, family and colleagues who have helped me along the whole journey, from the decision to carry out this research, through to its submission.

Portions of this work in Chapter 3 were developed in conjunction with Stefano Angioni.

Thanks Tony.

Contents

List of Figures

Chapter 1

Introduction

1.1 Composite materials

The use of composite materials is wide and varied, seeing applications in large industries such as automotive and aerospace, to personal safety, leisure equipment, and medical prosthetics. This use is continually growing, and replacing more traditional engineering materials such as alloys and polymers. Figure 1.1 shows an example of major structural features on a typical commercial aircraft that have in recent years seen an increase in composite use, where once they would have typically been made of aerospace alloys such as aluminium and titanium.

The reasons for such widespread use and growth in use are the remarkable properties of the fibres that form an integral part of the composite. These result in composite materials that have the desirable properties of being lightweight, and having high specific stiffness and strength. Other properties can be engineered, such as high fracture toughness, fatigue resistance and corrosion/environmental resistance.

A major difference between continuous fibre composite materials and more traditional engineering materials is the ability of the engineer to design the material itself, to assign to it the characteristics that would be desirable in the structure being designed. This has led to a necessity to progress existing analysis methods, which have often been focussed on isotropic or homogeneous materials. This is both a necessity at the design stage, where new structural forms of the composite can be assessed to give the required mechanical properties, and at the post-design stage, where the response of a structure made from such a composite can be ascertained.

1.1.1 Motivation

Recent developments in composite materials have led to the design and increase in use of '3D' composites. This class of materials was designed to alleviate problems of delamination in laminar '2D' and unidirectional composites. Further information on

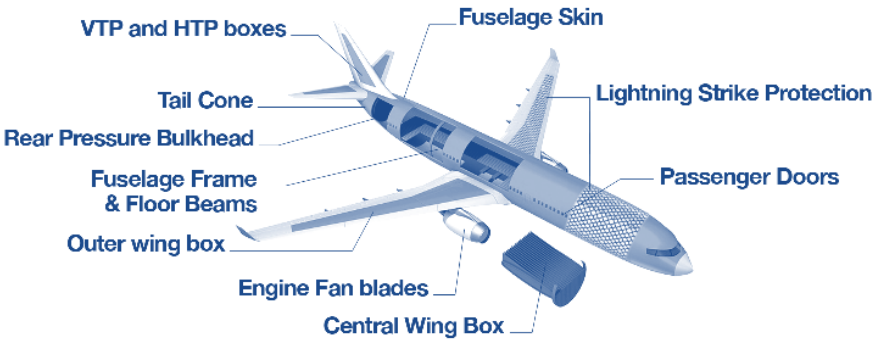

(a) Primary

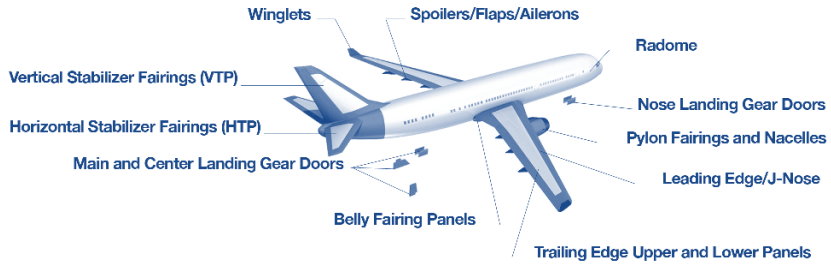

(b) Secondary

Figure 1.1: **Primary and secondary aircraft structures using composite materials** [1]

the development of composites is given in Chapter 2.

There has been much work in the past 10–20 years focussing on methods for the analysis of these and laminar composites, each examining different aspects of the material and its properties. As yet, no single technique has emerged that is of sufficient general applicability and practicality to have gained widespread adoption by industry.

1.2 Aims of the research

The title of this research is:

Damage tolerance and multi-scale simulation of novel 3D composites

This research will focus on a subset of 3D composites, the angle and orthogonal 3D weaved composite (section 2.2.1).

The aim of this research is to develop a mathematical formulation or framework for the simulation of the response of a 3D composite, under static mechanical loading. Simulation takes many forms and has many aims, and some of these are explained in section 2.3.

The initiation and propagation of damage is of particular interest, as is the behaviour of the structure under existing damage. This will enable an understanding of the performance of the materials in service under conditions of damage, and will allow the design of components with the ability to tolerate damage and result in an increased service life.

Multi-scale simulation will be essential to the aim of modelling damage tolerance. This is the ability to model the global response of a structure, such as an aircraft wing, whilst simultaneously having information at smaller scales, such as at individual tows or even fibres, to predict onset and progression of damage, and its effect on the structural response.

The overall aim of this research is to provide the means to predict the behaviour and response of this class of materials, to both facilitate the more widespread adoption of 3D composites, and to enable the design of new classes of 3D composite with desirable properties, such as higher strength/stiffness and greater resilience to the conditions that such components are likely to endure in service.

Much research has been done into these aims for traditional materials, and the wider goal of research on this topic is to bring understanding of and modelling capability for 3D composite materials to parity with that of alloys and polymers.

1.3 Outline of the thesis

This thesis is separated into a number of chapters that develop individual components of a unified model to simulate 3D composite materials and the effect of damage on them.

Chapter 3 develops a two-scale method to link the ply or tow scale and the laminate scale. This allows a seamless transfer of state information between the scales, allowing the benefit of an efficient solution at a coarser resolution, while incorporating the effects of damage at a much smaller scale, and in a localized region. The damage models are developed in the chapters that follow. The two-scale model can be applied in a chain fashion, allowing an unlimited model refinement in the areas of interest.

Chapter 4 develops a method for the simulation of interlaminar damage in the 3D weaved composite. This simulates the effect of the failure of the interlaminar binder tows, whose ability to transfer load through the thickness of the composite is critical to the integrity of the material. The model is incorporated in the two-scale model to sucessfully simulate the separation and stress redistribution that occurs as a consequence of binder tow failure.

Chapter 5 links the weave configuration, incorporating damage, to the laminate and sublaminate scale properties. This is done using an asymptotic expansion homogenization technique, allowing transfer of data between scales in both directions. The mean load at the laminate scale is used to localize the stresses to individual constituents of the weaved composite, which are then used in a continuum damage model developed within. The degraded local material properties are then linked to the effect on the mechanical properties at the larger length scale. The continuum damage model simulates damage in the plane of the laminate in a manner that complements the transverse damage simulated in Chapter 4.

Chapter 6 links the methods developed within into a unified model capable of efficiently simulating damage evolution in 3D weaved composites.

1.4 Publications

Portions of the work contained in this thesis have been published in the following journal articles:

1. S. L. Angioni, A. Visrolia, and M. Meo. A hierarchical multiple plate models theory for laminated composites including delamination and geometrical nonlinear effects. *Composite Structures*, 93:780–791, 2011. doi:10.1016/-j.compstruct.2010.08.003

2. S. L. Angioni, A. Visrolia, and M. Meo. Combining X-FEM and a multilevel mesh superposition method for the analysis of thick composite structures. *Composites: Part B*, 43(12):559–568, March 2012. doi:10.1016/j.compositesb.2011.07.005

3. A. Visrolia and M. Meo. Multiscale damage modelling of 3D weave composite by asymptotic homogenisation. *Composite Structures*, 95:101–113, 2013. doi:10.1016/j.compstruct.2012.07.018

Chapter 2

Background and literature review

2.1 Introduction

This section gives an overview of composite materials, and in particular 3D composite materials and their differences from other composite forms, and the challenges revelant to their simulation. This is a general literature review, separate literature reviews are conducted in the following chapters for the constituent models that make up this thesis.

2.2 Composite materials

Composite materials in the most general sense are materials that are composed of "two or more constituent materials or phases" [5]. The production of a material made of multiple phases allows the selection of constituent materials with different and desirable properties.

One of the most common types of composite material is the fibre reinforced comopsite. In the type of composite material that this research will focus upon, the phases are referred to as:

1. **the fibre** (discontinuous phase); and
2. **the matrix** (continuous phase).

In such a material, the high tensile strength of fibres is exploited and combined with a resin continuous phase, typically a thermoset polymer, to give the fibre reinforcements rigidity and form.

Modern use of fibrous composites was precipitated by the observation that certain materials exhibited remarkable properties when drawn into fibres (see Table 2.1). Initially, fibrous composites were made with short fibres, typically made of a glass, introduced at random orientations within a matrix. These materials were known as

discontinuous or **chopped fibre composites**. These materials combine some of the desirable properties of the fibres and the matrix, such as giving the polymer matrix a higher fracture toughness. For the purpose of analysis, the random nature of the fibres make these materials statistically homogeneous and isotropic.

		modulus/ GPa	**strength/ MPa**
Polymers	PP	1.5	1.3
	PET	3.0	55–75
	ABS	2.4	42
Alloys	Steel	190–210	290–680
	Aluminium	74	276–538
	Titanium	113.8	950
Fibres	Carbon	70–600	1750–3500
	E-Glass	72.4	3500
	Kevlar-49	128	2800

Table 2.1: Tensile properties of some typical polymers, alloys and fibres [5]

More recent (2nd-half of the 20th century) use of composite materials has introduced the continuous fibre composite. This is a composite in which the fibres remain continuous and uncut, and are given specific orientations within the material. In this way, the final composite material retains more of the mechanical properties of the constituent fibres. This use also coincided with the invention of carbon fibres in the 1950s–1960s.

The introduction of the continuous fibre composite also gave for the first time the opportunity to design the structure of the material from which a component could be made: the strength of the fibre was in its longitudinal direction, and this could be exploited with knowledge of the loading conditions in the component being designed.

Continuous fibre reinforced composites have seen a dramatic surge in use in the aerospace industry in recent years. Figure 1.1 gives examples of major structural elements on aircraft that are made of fibre reinforced composite materials on the latest generations of products, such as the Boeing 787 or Airbus A350 aircraft. The reason for the increased use is the remarkable structural properties available from proper design of the composite, combined with a reduction in weight from the existing materials.

The benefits of the use of composite materials can only be fully realised with an adequate understanding of their behaviour, such that they can be apropriately designed and analysed.

2.2.1 The structure of continuous fibre composites

Continuous fibres were first used in laminate structures. Initially, each lamina was composed of fibres oriented in one direction only (Figure 2.1). This structure is known

by a variety of names, including 1D, unidirectional, and uniweave composites.

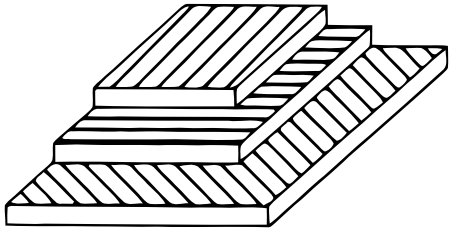

Figure 2.1: **Schematic of 1D laminated composite** [5]

The typical manufacturing process for these continuous fibre composites is by bundling individual fibres into **yarns** or **tows**. The tow is a bundle of 10^3–10^4 fibres, with a diameter of ∼1mm.

In designing a 1D composite, the lamina should have a variety of fibre orientations, to compensate for the lack of strength in the transverse directions in individual lamina. The individual lamina suffer from having very low strength in the in-plane direction perpendicular to the direction of the fibres.

Later development, aimed at increasing the lamina strength in the perpendicular direction, resulted in 2D or weaved composites. These composites are also laminar, but each of the lamina are composed of fibres in two orthogonal directions, interweaved in a manner that is familiar from fabric weaving (Figure 2.2). A number of different weave patterns can be used, such as plain, twill and satin, each with differing mechanical properties, including the ability to be draped over a complex pre-form.

Both the 1D and 2D composites are laminar, i.e. composed of discrete lamina, or layers. Within the lamina, the fibre orientations could be customized to give the laminate the desired properties. However, the very nature of the laminate structure means that between the lamina is a region of only matrix material. This means that the through-thickness strength is limited by the matrix material and the fibre/matrix bonding. Table 2.2 lists typical properties for common fibre/matrix combinations in laminar composites. The result of this is the separation of lamina, or **delamination**, as a failure mechanism.

	In-plane		**Transverse**	
	modulus/ GPa	strength/ MPa	modulus/ GPa	strength/ MPa
carbon/epoxy	145	1240	10	41
e-glass/epoxy	45	1020	12	40
kevlar/epoxy	76	1240	6	30

Table 2.2: Example laminate properties in in-plane and transverse directions [7]

An additional concern of the low through-thickness strength is that of impact resistance. Post-impact, the laminate structure is likely to suffer from internal delamination. This type of delamination has a large effect on structural integrity of the material,

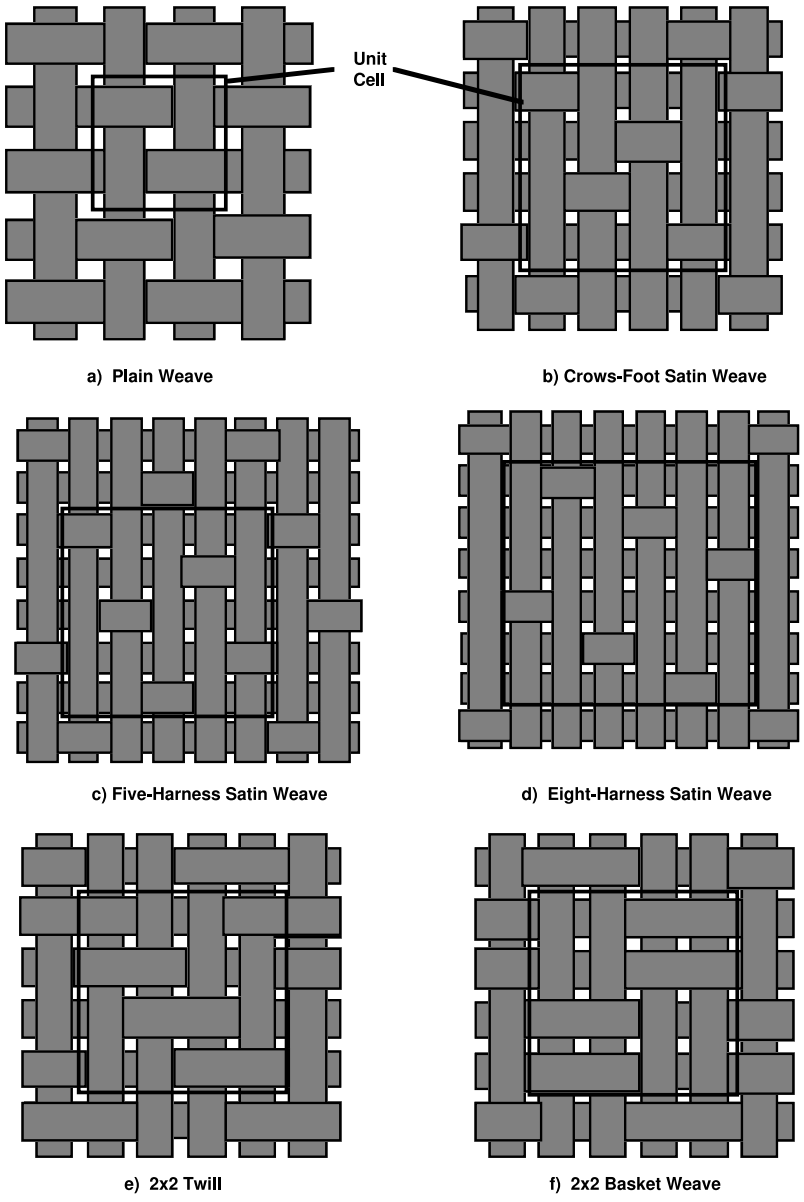

Figure 2.2: **Typical 2D weave structures** [6]

and can be difficult to detect. This limits the use of these materials where impact is possible, and the effects of loss of structural integrity unacceptable. Tong et al. [7] give examples of impact occurring in service of tooling, bird, hail and stone impact on aircraft components; and floating debris or impact with moorings for marine vehicles.

Unidirectional and weaved laminates have seen widespread use in certain applications where the loading on the material is such that delamination is unlikely, or of minimal concern. Alternatively, components have been designed around the limitations of this property, to decrease the tendency to delaminate.

A more complete solution to the problem of delamination is that of introducing reinforcement, in what are known as 3D composites.

'Three-dimensional composite' is a broad term that encompasses a wide range of composite structures that feature a fibre layout that includes some form of 'through-thickness' reinforcing fibre. Some of the more common 3D forms are detailed below.

Stitched composites

Stitching is one of the simplest forms of 3D composites. The composite is formed by sewing fibres through a stack of lamina that would otherwise have formed a unidirectional or weaved laminate. This method can also be used to join together separate lamina to form complex shapes. The stitching thread provides the through-thickness reinforcement that is absent in the laminar composites.

Braided composites

Braiding was one of the earliest forms for 3D composites. The braided composite is created by feeding the tows through a number of rotating yarn carriers that exchange and interweave the tows as they pass along their length, thus creating a detail 3D structure (Figure 2.3). Braiding is a process most suitable to slender or tubular components.

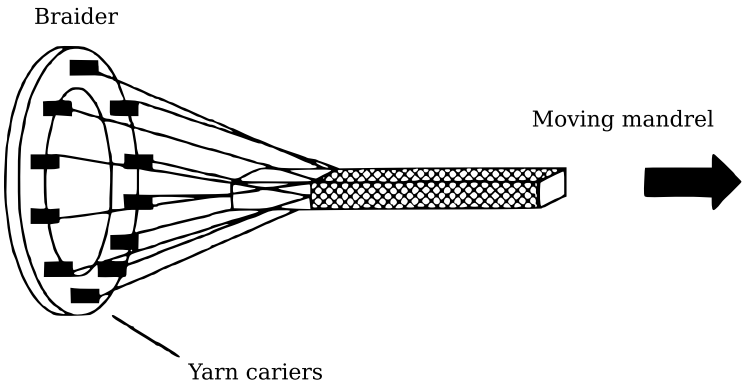

Figure 2.3: **Manufacture of braided composites** [7]

Knitted composites

Knitted composites have a structure very similar to that of knitted fabrics, where the tows are shaped into interlocking 'loops' (Figure 2.4). This form has a high degree of fibre curvature, which reduces the strength of the composite. This high degree of curvature also allows the fibre form to be draped over a complex shape before application of a matrix material, to form a composite with complex geometry.

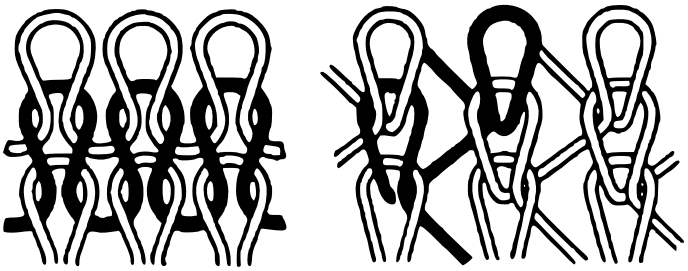

Figure 2.4: **Tow structure in knitted composite** weft (left), and warp (right) knitted fabric [7]

Weaved composites

Three-dimensional, or multilayer weaved composites are an extension of the 2D weaving forms seen in section 2.2.1, by adding fibres that run through the thickness of the composite. They are differentiated from stitched composites by having the through-thickness fibres an integral part of the weave, rather than as an addition to a 2D structure. The 3D weaved structure will form the focus of this research.

The fibres that make up the 3D composite are placed into three categories:

1. the **warp** or **stuffer** - these are the fibres in the direction fed by the weaving machine

2. the **weft** or **filler** - these are the fibres that are orthogonal to the warp fibres, and are fed interweaved between them

3. the **binder warp weaver** - these are the fibres that are also fed by the weaving machine in the same direction as the warp, but as the weave is formed, the binder tows are weaved around the weft fibres in different layers, acting to lock the separate warp/weft layers together

In weaving, the warp and weft fibres are generally constrained to be orthogonal to each other, and in the 0° and 90° orientations to the weave direction respectively. However, there are a number of configurations for the binder tow, as shown in Figure 2.5. An **orthogonal** weave is one in which the binder runs straight through the warp/weft layers, compared to an angle **weave**, in which the binder runs at an angle.

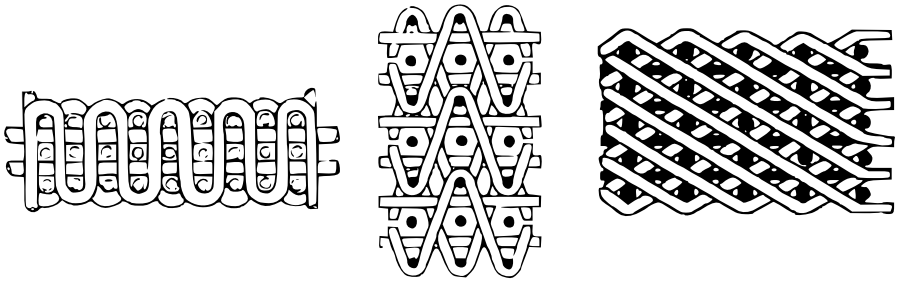

Figure 2.5: **Typical fibre architecture in three-dimensional weaved composite** through-thickness orthogonal (left); angle interlock (centre); and through-thickness angle (right). Warp fibres run in a straight line left to right; weft are perpendicular to the page; and the remainder are binder tows, in the plane of the page. [7]

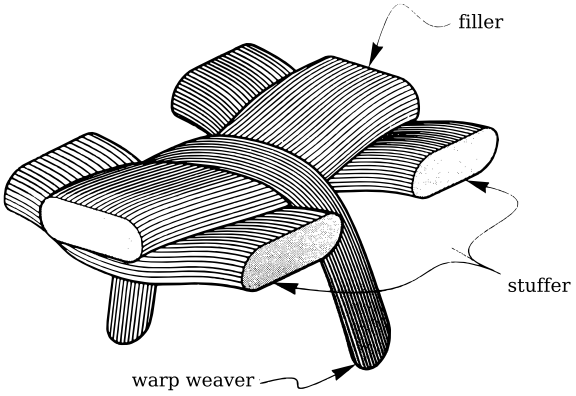

Figure 2.6: **Detail of locking between tows in 3D weave** [8]

The binder can either be **through-thickness**, or if it only passes around a subset of weft layers, **interlock**. These types of 3D woven composites can be considered as 2D woven composites with additional through-thickness strengthening fibres.

The introduction of a 3D structure adds interlaminar strength to the 2D and 1D structures, but there is also an associated cost. Inclusion of through-thickness fibres necessarily reduces the number of in-plane fibres, reducing the in-plane strength and stiffness. Additionally, the more complex tow path in a 3D structure increases the crimp ratio. The crimp ratio is a measure of how straight the fibres are, and is an indicator of a reduction in stiffness from a nominal value had the tow been straight. A number of definitions are defined to measure the crimp ratio, one definition is the ratio of the tow 'amplitude' to its 'wave length'.

The use of three-dimensional composites has been demonstrated for a variety of components. Mouritz et al. [9] conduct a review of applications, and finds that as of the date of their paper, there have been few commercial applications. A number of reasons are given, including the increased complexity and cost for manufacture. One important factor is the ability to predict the behaviour of the material, for which new analysis techniques are needed. A number of researchers resort to mechanical testing (e.g. McIlhagger et al. [10, 11]) in the absence of reliable or simple analysis methods.

2.3 Analysis of composite materials

There are many different types and methods of analysis, each focussed on delivering some specific information that will be of use to the engineer. This may be the deflection of the component under load, the stresses within the component, its natural frequencies or mode shapes, or its failure modes and response to such failure (damage tolerance). The analysis can be used to determine the mechanical properties of a particular configuration of fibres within a composite, or to determine the response of a component when the mechanical properties of its constituent parts are already known.

Of importance is the efficiency of the analysis. The efficiency is some function of the value or accuracy of the analysis, compared to the effort required to determine that information. Typically, the effort is limited by computational capability, and some compromise may have to be made to derive the quantities of interest.

The desired outcomes of analysis include the following:

- Prediction of strength and stiffness from the underlying fibre architecture
- Prediction of the failure and failure mode under loading in service

The information used in or required from an analysis occurs at a variety of length scales. For example, loads are applied on a component scale, such as a pressure load on an aerofoil surface. However, damage is of interest on a much smaller length scale, for example between regions of different weave structure, or even in individual fibres.

An analysis technique suitable for application to 3D composites must therefore account for interactions at all length scales, and be able to simulate the interactions between the length scales.

This section will examine some of the types of analysis that are available, with particular interest into their applicability for the modelling of composites.

2.3.1 Structural response

One of the main objectives of analysis is to determine the structural displacements of a component under loading. The most common method used for non-trivial geometries is the finite element method (FEM). A general background to the FEM will not be detailed here, but it is sufficient to say that it is a method for discretizing a larger structure into smaller elements whose behaviour can be modelled using understood analytical relationships. Many sources of further information on the finite element method can be found, such as Zienkiewicz et al. [12].

The FEM in all its forms has been successfully applied to composite materials. The most general case of the FEM is full 3D analysis, making use of the three-dimensional constitutive relationships. The FEM has no difficulty in allowing for the inherent anisotropy within a lamina.

Spatially variable material properties

The discretized unit of the FEM is the 'element'. Whereas no analytical solution may exist for the complex geometry of the component being analysed, it should be possible to solve for the element. This normally requires the element to have uniform or spatially independent properties. For uniform materials, or materials for which the inhomogeneity is on such a small scale as to render meaningless the distinction between the mechanical properties of multiple phases, this is not a problem. This is also the case for statistically homogeneous materials, i.e. those that are not strictly homogeneous, but are constructed with such a distribution of material properties as to make the 'average' properties uniform.

For composite materials, where there are at least two very distinct phases, a number of approaches can be used. The simplest is to constrain each element to lie within a distinct phase. For example, an element within the tow can be assigned the mechanical properties of the tow, and an element within the matrix can be assigned the mechanical properties of the matrix. This applies some large constraints to the modelling process: the analyst will require detail information on where each individual tow is (which may not be possible), each tow will require modelling to reflect its geometry (which will be labour and time intensive), and the number of elements will be huge (and thus the solution time unacceptably long).

The alternative to this is **homogenization**. This is the process by which the spatially

differing material properties are averaged out, thereby enabling the use of elements that are independent of the underlying distribution of phases.

The techniques of homogenization usually involve the examination of a representative volume element (RVE) or the repeating unit cell (RUC). The terms RVE and RUC are often used interchangeably in the literature, but Pindera et al. [13] make the distinction in Figure 2.7 by separating the concepts of statistical homogeneity and periodic microstructure. Byström et al. [14] give an overview of some of the different models that can be used for the homogenization and prediction of mechanical properties of RVEs in woven composites.

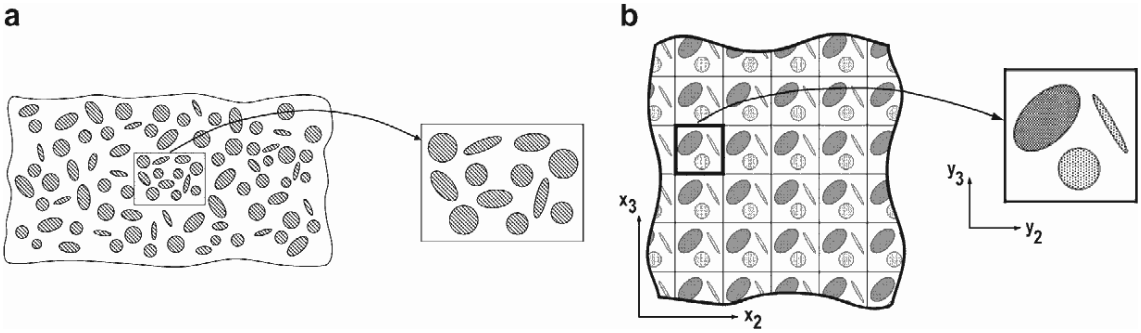

Figure 2.7: **RVE and RUC** Two geometric representations of a material microstructure: (a) statistically homogeneous microstructure characterized by an RVE; (b) periodic microstructure characterized by an RUC. [13]

The simplest level of homogenization is that of fibres oriented in one direction within a matrix. This can be used for determining the properties of individual tows, or of a single lamina in a unidirectional composite.

For a composite composed of two phases, the fibre, f and the matrix, m, the volume fractions, v, of the two phases are given by:

$$v_f = \frac{h_f}{h_f + h_m} \qquad v_m = \frac{h_m}{h_f + h_m} \tag{2.1}$$

where h are the phase volumes. From this, a 'rule of mixtures' can be derived by considering the isostrain or isostress loading and response of a RVE or RUC. The homogenized properties are derived as:

$$E_1 = E_f v_f + E_m v_m \qquad E_2 = \frac{E_f E_m}{E_m v_f + E_f v_m}$$
$$\nu_{12} = \nu_f v_f + \nu_m v_m \qquad G_{12} = \frac{G_f G_m}{G_m v_f + G_f v_m} \tag{2.2}$$

where E is the modulus, G is the shear modulus, ν is the Poisson ratio, and the 1 and 2 subscripts indicate the fibre longitudinal and transverse directions respectively.

The review in Byström et al. [14] classifies this method as a semi-analytic engineering model. On a larger scale, the same approach can be used considering the two phases to be the tow (as homogeneous) and the matrix.

Other semi-analytical models are based on a similar approach, discretizing more complex RVEs (including those for 2D and 3D structures) into essentially unidirectional segments. Other models are summarized in the reviews of Cox and Flanagan [6] and Tan et al. [15], with information on their relative advantages and disadvantages. The simplicity of the 'rule of mixtures' model means that it takes no account of local inhomogeneities, such as matrix rich regions or undulating/wavy tows which are inevitably present in 2D and 3D composites. For this, analysis of the geometry of the tows is required.

The 'mosaic model' by Ishikawa and Chou [referenced in 15] is one of the first attempts at this, considering a 2D (weaved) composite structure to be an assembly of 1D segments. The 1D segments are successively built up and homogenized in either a serial or parallel fashion. In the mosaic model, tows of different orientations are considered separately, so the continuity of the fibres and the inherent undulations are ignored. Ishikawa and Chou later refined this model to the 'fibre undulation model'. This subdivides the RVE into regions of straight tows, undulating tows, and pure matrix. The straight regions are considered in exactly the same way as the mosaic model, and the undulating regions by further subdivision and integration of the properties in the direction of interest. The fibre undulation model only considers the undulations in one of the directions (the warp or weft direction), and does not fully consider the interactions between the undulating regions and the surrounding straight tow regions. This is addressed by the 'bridging model', which considered these interactions.

The 'XY'- and 'YX'-models by Tan et al. [16] essentially take this approach, breaking the RUC down into a number of 'micro blocks', and applying the homogenization successively in different directions. These have been extended to 3D microstructures as the 'XYZ'- and 'YXZ'-models [17], and the technique is also referred to as 'orientation averaging' in Cox and Dadkhah [18] and Wu et al. [19].

The other two homogenization categories identified in [14] are models based on the FEM, and asymptotic expansion homogenization (AEH) methods. The FEM method is to use FEM software to fully model an RVE to determine its effective mechanical properties. The obvious disadvantage in this method is the necessity to develop a detailed geometric model of the tows. Despite the availability of powerful software and hardware, this still a very demanding task for certain 3D configurations. The AEH process [14] is derived from the studies of partial differential equations, using a parameter to describe the fineness of the microstructure. The benefits of such an approach are given as not suffering from the assumptions made in the semi-analytic and FEM methods, and the ability to reverse the homogenization process, i.e. to determine the local distribution of parameters from a macroscopic homogenized value.

Where a homogenization technique has been used to define material properties, the constraints on using the finite element method are greatly reduced. In a 3D finite element analysis, the discretization is no-longer dependent on the length scale of the inhomogeneities. This means that the FEM can be applied in much the same manner that it would have been had the material been homogeneous.

Further simplifications can be made that will be familiar to users of the FEM for the analysis of homogeneous materials. Commonly, for the analysis of thin laminate structures, plate or shell elements are used, producing a model where certain assumptions are made about the displacement field, and the number of degrees-of-freedom are reduced greatly. These are collectively known as the equivalent single layer (ESL) models. The ESL models are capable of adequately modelling overall displacements in most cases, however the assumptions made prevent them from determining accurately the internal stresses, which are of particular importance to damage simulation. The layerwise models solve the problems of the ESL models by assuming that the through-thickness displacement field in a laminar composite can be represented in a piecewise manner. There are advantages and disadvantages to taking either an ESL or a layerwise approach, and these are explored in more detail in the literature review in section 3.2 .

Naturally, these techniques have been developed for application to laminated composites. Thus, they can not be applied as-is to the 3D woven composites of interest here.

2.3.2 Damage tolerance and failure

An important part of determing the behaviour of components is the prediction of the conditions under which it will fail. Beyond this is the understanding of how the structure responds in the presence of damage. This is known as ‘damage tolerance’.

Understanding damage initiation/propagation and damage tolerance is important in considering the entire life of a component. In most applications, catastrophic failure is to be avoided. Without understanding the criteria for the initiation or behaviour of damage, a component would have to be considered unfit for service following any circumstance where damage may have ocurred. Typical examples for an aircraft component may be impact from birds, hail, or tooling—it is clearly uneconomical to scrap a component under all these circumstances.

As well as assessing the effect of damage after it has occurred, damage tolerance can be incorporated into the design stage, to enable components to be designed to withstand certain types of damage.

Types of damage

As mentioned in earlier sections, delamination is a damage mechanism that is particularly associated with laminar composites. 'Delamination' can also occur in 3D weaved structures (where the structure is considered as a type of 'reinforced laminate'), but the presence of through-thickness fibres add strength and place a greater emphasis on other failure mechanisms that play a lesser role in laminar composites.

The most comprehensive reviews on the subject of damage in 3D woven composites is Cox et al. [8]. This built on earlier work into compressive failure [20], delamination, and buckling [21], and was later extended to tensile failure modes [22]. A similar review on tensile failure mechanisms is given in [23], and the results from tensile testing are examined in Quinn et al. [24].

Damage from tensile loading Extensive test programmes were conducted and reported in [8, 22], covering angle interlock, angle through-thickness and orthogonal through-thickness weave forms. Additionally, most weave forms were tested in a 'lightly compacted' and 'heavily compacted' form, where the heavily compacted variant had a substantial through-thickness pressure applied during manufacure. This application of pressure affects the 'waviness' of the tows in the final consolidated form.

Testing involved monotonic loading of dogbone specimens to failure, and the peak load and strain to failure were recorded. Loading was in the warp fibre direction. [8] reports that the primary failure mechanism is the rupture of a tow, which is nearly always the failure of the entire cross section. This is followed by the matrix cracking around the entire circumference of the failed tow, debonding and isolating it from the surrounding material. Subsequently, the surrounding tows take up the load. As the number of failed warp fibres increases, cracks form in the matrix between weft fibres, often leading to ultimate failure. In other instances, the crack is arrested on meeting a delamination, and failure occurs when enough cracks have opened up such that the load carrying capacity of the remaining material is exceeded.

This complex failure mechanism leads to high strains at failure, with the warp fibres being pulled out in excess of 10mm (where typical tow cross section is $\sim 1\text{mm}^2$). The failure mechanism is often described in the literature as 'fibre pullout'.

Damage from compressive loading Similar test programmes to that for tensile loading have been conducted for compressive loading in [8, 20, 21]. Through-thickness and layer interlock angle forms were tested in [20].

Testing involved monotonic loading of cubic and dogbone specimens in the direction of the warp fibres. Maximum compressive stress and strain at failure were recorded. Examination of the specimens revealed that during the 'linear elastic' regime, the warp fibres begin to buckle 'in-plane', between sucessive intersections with binder tows. These are described as producing 'soft spots' of up to 10mm long. At higher

loads, extensive debonding between the warp/binder tows and the matrix occurs, as more of the warp fibres buckle. The buckling is constrained by the surrounding matrix and binders, and does not by itself lead to ultimate failure. Instead, as the warp fibres fail and neighbouring fibres take up the load, the fibres begin to fail from kink band formation, with the deflection being in the same direction as the earlier buckling (Figure 2.8). This also leads to extensive matrix cracking. It is this process of matrix cracking and kink band formation that ultimately leads to failure. [20] observes the behaviour of the material after the formation of the fatal shear band to be like "large separate pieces, each of which move[s] as an almost rigid body, with all strain accommodated over the shear band".

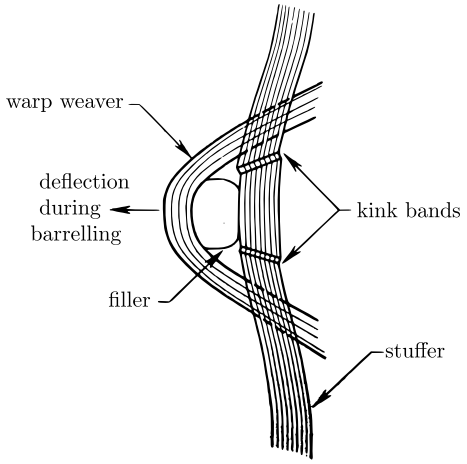

Figure 2.8: **Kink band formation in 3D weave** Load applied in the stuffer direction causes barrelling which forces the filler, constrained by the binder (warp weaver), against the stuffer creating kink bands [20]

The process of buckling and delamination is further explored in Cox [21], where equations are given for the required through-thickness reinforcement in a weaved composite to supress buckling. This relates the critical delamination length to the length between the through-thickness tows. Delamination and bucking can be reduced for a given load, thus making the formation of kink bands the primary initiator for failure.

Similar observations on the failure process are made in Cox et al. [8], additionally noting that heavily compacted specimens suffer more from bucking as a result of the aspect ratio of their structure being more elongated. Additionally, the initial waviness of the tows present during consolidation is identified as contributing to the propensity of the tow to buckle.

Damage from other loading Much less work has been performed to assess the detailed behaviour of 3D composites under other loading modes, such as shear. Where work has been conducted, the focus has been on establishing the mechanical properties, or the influence of the binder tow on the mechanical properties. Such work is presented

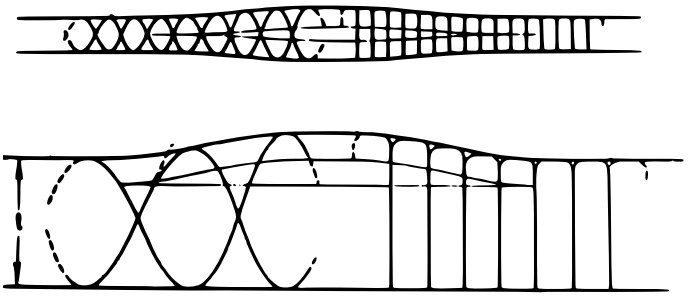

Figure 2.9: **Delamination in the presence of transverse fibres** angle (left) and orthogonal (right) fibres, showing symmetric (top) and biased (bottom) buckling [21]

by McIlhagger et al. [11], where testing revealed no correlation between interlaminar shear strength and the binder tow density. No comments are made in [11] with regards to the details of the damage process. Comments are made regarding the effect of the configuration of the composite on the flexural strength, however, again no detail is given on the failure process. This is clearly a gap in the understanding of the failure mechanisms that govern 3D weaved composites.

The general understanding of the failure process in 3D weave forms from the testing and analysis in [8, 20–22] is summarised well by Cox et al. [8]:

> "Tows in 3D woven composites fail in either tension or compression as discrete units. ... Thus the fundamental unit for modeling failure is the tow. Modeling the response of smaller groups of fibres would appear superfluous to predicting engineering properties, while considering only larger volumes of material, such as layers of stuffers or fillers, would miss the essential physics of failure."

Prediction of damage initiation

To perform successful damage tolerance calculation on a structure, it is first required to determine the condition under which damage occurs. In general, 'damage' could be considered to be any effect that is irreversible, including material or structural plasticity. Here, damage is considered to be any effect that causes significant change in the way that the structure can sustain a load (e.g. change in stiffness or strength), thus requiring some fundamental change to the modelling process to understand the response of the structure.

Much work has been conducted into the determination of failure criteria in composite structures. Most of this work has focussed on laminar composites and their failure mechanisms, but much of this can be applied to 3D weave forms.

The failure theories can be broadly classified into three groups:

1. **Limit** or **non-interactive**, such as maximum stress or strain criteria. These are the simplest criteria, and test the various stress or strain components against an allowed maximum value to determine if failure has occurred.

2. **Polynomial** or **interactive**, allowing for interaction between stress components. These can be considered an analogue of the von Mises criteria in isotropic materials. The most general case is given by Tsai in tensor form as:

$$F_i\sigma_i + F_{ij}\sigma_i\sigma_j + F_{ijk}\sigma_i\sigma_j\sigma_k + \cdots \geq 1 \tag{2.3}$$

Other interactive criteria, such as Tsai-Wu and Tsai-Hill are special cases of (2.3):

Tsai-Hill
$$\left(\frac{\sigma_1}{X}\right)^2 + \left(\frac{\sigma_2}{Y}\right)^2 + \left(\frac{\tau_{12}}{S_{12}}\right)^2 - \left(\frac{\sigma_1\sigma_2}{X^2}\right) \geq 1 \tag{2.4}$$

Tsai-Wu
$$\frac{\sigma_1^2}{X_T X_C} + \frac{\sigma_2^2}{Y_T Y_C} + \frac{\tau_{12}^2}{S_{12}^2} + \sigma_1\left(\frac{1}{X_T} - \frac{1}{X_C}\right) + \sigma_2\left(\frac{1}{Y_T} - \frac{1}{Y_C}\right) + \sigma_1\sigma_2 f_{12} \geq 1 \tag{2.5}$$

where $1,2,3$ subscripts are the fibre, perpendicular in-plane and transverse directions respectively, X, Y, Z, S are limit strengths in the $1,2,3$ and shear directions, subscripts T and C refer to tension and compression, and f_{12} is an experimental coefficient, e.g. to give Tsai-Hahn.

3. **Partially interactive**, a combination of the above two methods. Examples of this are the theories by Puck and Schürmann [25] (shown here in (2.6)), or Cuntze and Freund [26] for matrix failure, using various definitions of stress invariants:

Fibre tensile
$$\frac{1}{\varepsilon_{1T}}\left(\varepsilon_1 + \frac{\nu_{f12}}{E_{f1}} m_{f\sigma}\sigma_2\right) \geq 1$$

Fibre compressive
$$\frac{1}{\varepsilon_{1C}}\left|\left(\varepsilon_1 + \frac{\nu_{f12}}{E_{f1}} m_{f\sigma}\sigma_2\right)\right| + (10\gamma_{21})^2 \geq 1$$

Matrix tensile
$$\sqrt{\left(\frac{\tau_{21}}{R^A_{\perp\parallel}}\right)^2 + \left(1 - \frac{p^{(+)}_{\perp\parallel}}{R^A_{\perp\parallel}} R^{(+)A}_{\perp}\right)^2 \left(\frac{\sigma_2}{R^{(+)A}_{\perp}}\right)^2} + \frac{p^{(+)}_{\perp\parallel}}{R^A_{\perp\parallel}}\sigma_2 \geq 1$$

Matrix compressive
$$\sqrt{\left(\frac{\tau_{21}}{R^A_{\perp\parallel}}\right)^2 + \left(\frac{p}{R}\right)^2 \sigma_2^2} + \left(\frac{p}{R}\right)\sigma_2 \geq 1 \tag{2.6}$$

where $\varepsilon_{1T}, \varepsilon_{1C}$ are the failure strains in tension and compression in direction 1, subscript f refers to the fibre, E and ν are modulus and Poisson's ratio, $m_{f\sigma}$ is a stress magnification factor for the fibre in the matrix, loaded in the 2 direction, p is the slope of the fracture envelope, and R is the fracture resistance (X, Y, Z or S dependent on loading direction) [25].

In the last 20 years, a significant contribution into the prediction of failure in composite materials has been made in the 'World-Wide Failure Exercise' (WWFE). The WWFE sought to conduct a comparative assessment of the capabilities of a wide range of failure theories. This was done by having the authors of the various failure theories apply them to a number of standardized test cases. The result of this is a comprehensive review of 19 different theories, each applied to 14 different test cases, published as Hinton et al. [27]. The results of the exercise were published during the 13 year course of the WWFE, the most useful being [28–30], which are summarized and republished in [27]. One of the conclusions of the WWFE was that the polynomial criteria, in particular Tsai-Wu, proved to have the best agreement with the experimental data for the test cases examined.

Other reviews into the various failure criteria have also been published. Orifici et al. [31] separate out the various criteria into functional groups (fibre, matrix, fibre-matrix interface, and ply failure), and by loading mode (tensile, compressive and shear). Onal and Adanur [32] conduct a similar review, focussing on the suitability of the modelling techniques for 2D (weaved) composites. They consider a number of 'micro-mechanical' models, where the microstructure of the composite is considered when determining stresses and failure. Icardi et al. [33] present a review of many of the same models, and remarks on the differing capability of the models under different loading conditions. The performance of 'physically-based' criteria (accounting for microstructure) are compared to the 'generalized' failure criteria (independent of local phenomena, such as the polynomial criteria) by conducting detail 3D finite-element analysis. The paper attempts to determine some criteria for the applicability of the various models, based on the loading conditions and the material configuration. A general conclusion is reached that relative accuracy of the physical and general failure models is dependent on specific conditions. Daniel [34] conducts another review, again with special consideration for weaved laminates. The conclusions are much the same as [33], and the author's guidance is that in practice, a number of failure criteria should be applied, and the most suitable based on considerations of safety factor should be used.

LaRC03 is a set of failure criteria for unidirectional laminate composites developed in [35] in an attempt to define a single set of criteria (as opposed to the approach in [34]). The approach was developed in response to the observation that the methods trialled in the WWFE produced predictions that varied by up to an order of magnitude. The LaRC03 criteria are phenomenological criteria based on the Mohr-Coulomb effective stress, a method traditionally used where fracture under tensile loading is different to that under compressive loading. The plane stress assumptions of LaRC03 were extended to a full 3D formulation later in LaRC04 [36], and the authors claim the model is a significant improvement over the Hashin criteria, though provide no comparison to polynomial criteria such as Tsai-Wu. In general, the limitations of these methods are that the damage criteria have been developed for use on unidirectional plies. Some work on 2D woven composites has been conducted, but application to 3D

woven materials would be limited to application at the tow scale, where the tow is considered a unidirectional region.

Analysis of damage effect and growth

As described in the previous section, damage is considered to be an effect that changes the response of the structure. To account for this change, the model has to change beyond that used for predicting the onset of damage.

Damage modelling can be categorized into one of two approaches:

1. **explicit**, where individual instances of damage are explicitly incorporated into the model, e.g. by modification to the geometry or mesh; and
2. **continuum**, where the effect of all damage in a given volume is averaged, and the effective properties modelled in a continuum manner.

The choice between the two approaches is both a question of the detail of the information required, and the computation expense involved. van der Meer and Sluys [37] observe that while initiation and propagation is a phenomenon that acts on the microscale, a mesoscale approach (assuming homogeneous lamina with orientation dependent orthotropic material properties) tends to be adopted for reasons of computational efficiency. The issue of scale is introduced here to explain the differing approaches of damage modelling, however multiscale analysis will be explored further in section 2.3.3.

The literature in continuum damage modelling is explored in section 5.2.2. The literature in explicit damage modelling and cohesive modelling is explired in section 4.2.

Progressive damage models

The methods of modelling the effect of damage described in section section 2.3.2 can easily be incremented succesively to simulate progressive damage. For example, in the continuum model of Reddy et al. [38], after the failure criteria is met the stiffnes is reduced, the equilibrium recalculated, and the load increased to meet the failure criteria again. This process is repeated until the stiffness of the element is close to zero. In the cohesive models that explicitly incorporate the discontinuity, a cohesive law is used to model the progression of damage. In Remmers et al. [39], the appearance of cohesive segements can even model the growth of the crack (Figure 4.3).

This iterative method forms the core of most of the approaches in the literature to model damage progression (e.g. Robbins and Reddy [40]). The simplicity in this allows for ease of implementation in FE codes. A good overview of how a continuum damage model is implemented in the commercial FE package ABAQUS using the 'user material' routines is given by Knight [41]. Chen et al. [42] use a similar implementation of interface elements to explicitly model the delamination.

Tay et al. [43] implement a progressive damage model using an element failure method (EFM), similar to the REFM of [44]. The implementation of their iterative process is well illustrated in a flow chart diagram presented in their paper. The method is shown to give near identical results when a model with EFM is compared to a standard FE model with missing elements, simulating the zero-traction condition. Further work comparing iterative element failure with test data reveals a good correlation. A novel approach is taken in the latter part of the paper, termed by the authors as 'EFM-CE', a hybrid EFM and cohesive element method. Here, solid elements are used to model a laminate, and the in-plane damage modes (fibre or in-plane matrix failure) are modelled using EFM, whereas the out-of-plane damage modes (delamination) are modelled using a cohesive law. This combination of models is demonstrated on a double notched cross-ply specimen, and the model predicts the post-initial failure response well, although not the ultimate load.

Bednarcyk and Arnold [45] present a continuum damage model as part of a larger, multi-scale system. The model presented has novelty in that the model is stochastic, where the material properties are assigned using a Weibull distribution, and a statistical fibre failure model. This was demonstrated to show a realistic failure mode on a unidirectionally reinforced metal matrix composite (MMC).

Lapczyk and Hurtado [46] develop a simplified progressive model for the brittle failure of composites. The model behaves in a linear elastic manner until initiation, determined by Hashin's failure criteria. From there on, the damage variable is calculated using a displacement interpolation:

$$D = \frac{\boldsymbol{u}^F(\boldsymbol{u} - \boldsymbol{u}^I)}{\boldsymbol{u}(\boldsymbol{u}^F - \boldsymbol{u}^I)} \tag{2.7}$$

where $\boldsymbol{u}$ is the displacement, and the superscripts I and F refer to the displacments at damage initiation and ultimate failure respectively. The interpolation form is chosen to give a linear softening response under uniaxial loading. The displacement at ultimate failure is predicted using the critical fracture energy, G_{IC}. This model is simple to implement in FE code, and the results presented show good correlation to testing of notched GLARE specimens.

Key et al. [47] develop a 'multicontinuum theory' progressive damage model for a weaved laminate. Here, the RUC is decomposed into three constitutive parts: the warp tows, the weft tows, and the matrix, and the loads within each are distributed appropriately. In this way, the failure (using a continuum damage model) is modelled separately in the constitutive components, whilst simultaneously making use of the homogenized variables in the global solution. This provides a novel way of combining the information available at different length scales, and introduces the concept of multi-scale simulation.

From the review of literature on the topic of damage tolerance, it is understood that most work has focussed on unidirectional laminates, followed by that on weaved

(2D) laminates. Amongst this work, most are derivatives of the simple failure criteria developed by Hashin, and the more complex models are always derived from correlation to experimental data rather than a theoretical understanding. The focus on laminate composites has also directed much of the work to investigating and modelling the phenomenon of delamination. Whilst some work has been conducted into understanding the failure mechanisms of 3D (particularly weaved) composites, limited progress has been made into its modelling. The concepts of delamination modelling from laminar composites can be applied to 3D weaved composites if the effects of the through-thickness reinforcement fibres are included and the remainder is treated as a laminate; this would also allow continuum damage calculation on the homogenised 'plies'. To understand in more detail the interaction between the tows, it is required to model at a smaller length scale.

2.3.3 Multi-scale simulation

In the analysis of fibrous composites, it is clear that different information is available at the different length-scales for use as an input. Additionally, it has been shown in preceding sections that different information at differing length-scales is required as an output dependent on the use of the information. A typical definition of the various length scales are shown in Figure 2.10.

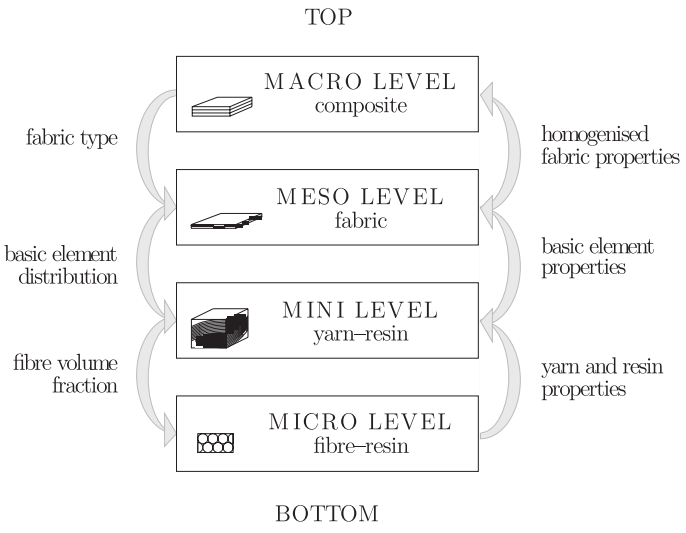

Figure 2.10: **Length scale definitions in multiscale modelling** [48]

macro scale analysis for information on the global properties, such as structural deflection. Homogenization is the process used to describe the global material properties using information from smaller length scales, and can feed into a model such as an ESL model.

meso scale analysis at the ply level (in laminar composites). This is necessary to determine the stresses that contribute to failure mechanisms such as delamination. Typically, a homogenization method is used (such as those described in section 2.3.1) to determine the lamina properties, and either a full 3D analysis with one element per lamina, or a layerwise analysis is performed.

mini scale analysis that explicitly accounts for the tows to determine their interactions with each other and the matrix.

micro scale analysis at the sub-tow level, considering the difference in modulus between the individual fibres and the pre-preg matrix. The homogenized tow properties can be determined using a process such as the rule of mixtures (2.2)

The definitions here are only an example, the literature tends to define the terms as appropriate for the problem being examined. The key to the multiscale analysis process is the passing of information up and down the 'hierarchy' of scales, as illustrated in Figure 2.10.

Broadly, multiscale methods can be split into two categories:

1. **sequential** or **multistep**, where one 'level' of the calculation is performed, and the output is passed on as the input to the next level. Most of the methods presented in this review have been sequential, e.g. the tow (micro-) or lamina (mini-) scale properties are homogenized, and then used in the determination of the lamina (meso-) or laminate (macro-scale) response.

2. **simultaneous** or **concurrent**, where the scales are solved simultaneously, thus maintaining displacement and load continuity across the scales.

The concepts introduced already in this review can be trivially incorporated into a sequential multiscale model. The remainder of this section is primarily concerned with the use of these concepts (homogenization for moving 'up' the hierarchy of scale (reviewed by Allen [49]), decomposition for moving 'down') in simultaneous multiscale analysis.

When performing analysis of composite materials, it it typical that detail modelling is only required in some regions—those where stresses are high, damage is progressing, or simply where the designer is most interested. This can be done by application of a different model in the locality of the region of interest. The use of different models gives the technique the name 'multi-model', and their use in different regions gives 'global-local'. This approach is simple, and relies on the definition of suitable boundary conditions between the degrees-of-freedom in the various models. The displacement

field is described as:

$$\begin{aligned} \boldsymbol{u} &= \boldsymbol{u}^G && \text{on } \Omega_G \\ \boldsymbol{u} &= \boldsymbol{u}^L && \text{on } \Omega_L \\ \boldsymbol{u}^L &= \boldsymbol{u}^G && \text{on } \Gamma_{GL} \\ \Omega &= \Omega_G \cup \Omega_L \end{aligned} \tag{2.8}$$

where Ω is the problem domain, and G and L superscripts refer to the global and local domains respectively, and Γ_{GL} represents the boundary between the global and local domains.

A more advanced application of the global-local approach is using superposition, or *s-refinement* in FEM terminology. Using superposition, selected regions of the model are represented by multiple meshes. Fish and Markolefas [50] describes the use of *s*-refinement for multilayered laminates. In addition to considerations at the boundaries, explored in Park et al. [51], the model requires a unified strain formulation, including the coupling terms between the two displacement fields. The displacement field in a local region is given by:

$$\begin{aligned} \boldsymbol{u} &= \boldsymbol{u}^G && \text{on } \Omega_G - \Omega_L \\ \boldsymbol{u} &= \boldsymbol{u}^G + \boldsymbol{u}^L && \text{on } \Omega_L \subseteq \Omega_G = \Omega \\ \boldsymbol{u}^L &= 0 && \text{on } \Gamma_{GL} \end{aligned} \tag{2.9}$$

The displacement-strain relationship is $\varepsilon = \nabla \boldsymbol{u}$, from which the constitutive relationships can be derived.

This method was presented in [50] and developed further in Fish and Guttal [52]. Here, the authors used an ESL plate model for the global domain, and a full 3D model with elements representing each layer for the local domain. The model showed superior results to other models enhanced by *p*-refinement (increase in the polynomial order in the elements). The resulting model demonstrated that an efficient ESL model using regions enhanced by 3D elements could be used to predict accurate interlaminar stresses in those regions, which could then be used in failure prediction (e.g. for delamination).

The use of *s*-refinement also introduces the concept of hierarchy. When *s*-refinement is used with different models, the local model is normally the 'more refined' model. In the example above, the 3D elements are capable of describing a more refined displacement field than the global ESL plate model. If a number of displacement fields are available for use in analysis, they can be placed into a hierarchy, where each level is more capable than the previous. Then each level can be added to the problem as the required information increases.

This is the basis of the *variable kinematic model* proposed by Robbins and Reddy [40, 53]. In it, the authors use a FSDT model, a layerwise model and a discontinuous field model (for delamination) in that order in a single formulation to model a laminar composite (Figure 2.11).

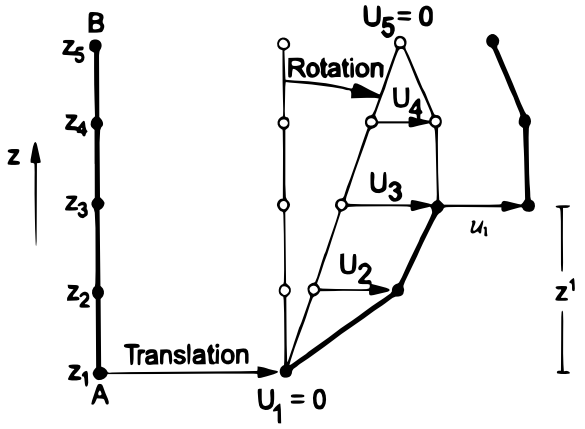

Figure 2.11: **The variable kinematic model** Through the thickness of the plate (A-B), the FSDT field defines the macro scale translation and rotation, superimposed are displacements $\boldsymbol{U}_i$ from a layerwise field, and a displacement discontinuity $\boldsymbol{u}_1$ for delamination [53]

This work was based on earlier work by Barbero [54], Barbero and Reddy [55], where delamination using a field with Heaviside step functions was incorporated into a Generalized Laminated Plate Theory, itself developed by Barbero and Reddy [56].

An overview of the concept of hierarchic models is given in Actis et al. [57]. The definition of hierarchic modelling is clarified as "a sequence of mathematical models, the exact solution of which constitute a converging sequence of functions . . . for the objectives of analysis". This is useful, since the concept of hierarchy is also used for related concepts such as *hierarchic finite element spaces* or *h*-refinement, where the converging sequence of approximate solutions is achieved by reducing the length scale of the discretization; and *hierarchic basis functions* or *p*-refinement, where convergence is achieved by increasing the complexity (often polynomial order) of the basis functions. The latter two examples of hierarchy are methods of reducing the discretization errors, whereas hierarchical modelling as used here is a systematic method of refining the mathematical model used.

Models based on this concept began to emerge during the 1990s, under a variety of names. Where Barbero viewed it as a natural extension of the layerwise plate theories, Robbins and Reddy described the model as 'variable kinematic', in reference to the ability to use different mathematical models. Fish and Markolefas, Fish and Guttal used the term 'superposition', where the superimposed domain used an identical mathematical model to the underlying domain. Li and Liu [58] developed a laminate plate model using 'double superposition', where the underlying model is linear, and second- and third-order fields are superimposed.

The introduction of the concept of hierarchy of displacement fields is described by Zohdi et al. [59], who describe their aims as attempting to use homogeneous displacement fields to represent a heterogeneous domain. The authors achieve this by using an error estimate for a given field, and a hierarchical family of material

descriptions at scales intermediate to the macro- and micro-scales. The use of an error measure is also essential in adaptive models that automatically define the domains for the different levels in the hierarchy, as in the superposition models proposed by Yue [60], Yue and Robbins [61].

In Fish and Shek [62], the authors identified the similarities between the approaches of *multiscale* and *global-local* modelling, and used it to develop a three-scale simultaneous multiscale model. Instead of an error measure, the local domains are adaptively included using a refinement process called spectral decomposition.

Takano et al. [63] develop a four-scale hierarchy, with the lower scales represented using a 3D FEM periodic RUC on a much smaller length-scale than the higher scales:

$$u_i = u_i(\boldsymbol{x}, \boldsymbol{y}) = u_i^0(\boldsymbol{x}) + \varepsilon u_i^1(\boldsymbol{x}, \boldsymbol{y}) \tag{2.10}$$

where $\boldsymbol{x}$ is a location in the domain on the macro-scale, $\boldsymbol{y}$ on the periodic microscale, related by the scale factor $\varepsilon = \boldsymbol{x}/\boldsymbol{y}$. u^0 can be considered the averaged, smooth displacements, and u^1 the micro-scale perturbations.

This approach is useful, since the analyst is only required to mesh the larger length-scales; knowledge of the position of the constituents at the fibre/matrix scale is not required. The power of this method is demonstrated by modelling a 2D weave lamina and a 3D knitted structure to the mesoscopic level. The authors incorporate anisotropic damage into their model at the mini-scale (fibre-matrix scale). The process for transition to a shell/plate macro-scale is developed later in [64].

Cox et al. [65] propose a 'binary model' specifically for 3D composite structures that can be considered a multiscale or superposition model. In the model (Figure 2.12), a three-dimensional orthotropic continuum mesh is used to model the *effective medium*, a homogenized representation of the matrix and all properties of the tows other than in the axial direction. The axial properties of the tows are represented by a superimposed network of beam elements.

As already seen in [47], decomposition can be used on a homogenized model to apply damage criteria at the tow scale. Similarly, the effect of damage can be incorporated on the smaller length scales of multiscale models to account for the differing damage mechanisms on different length scales. Talreja [66] develops a model that separates matrix and fibre damage, and includes the effect of *fibre-bridging*, the process where a discontinuity in the matrix is constrained by the fibres yet to fail. This is typical in a 3D weaved composite, where the through-thickness fibres act to reinforce against delamination. The author proposes a model where continuum damage is used at the longer length scales and discrete damage on the shorter scales. Mishnaevsky and Brøndsted [67] give a good overview of micromechanical modelling of damage, and in [68], develop a model for unidirectional composites with damage and statistical variability in fibre strengths. Souza et al. [69] perform similar work for impact analysis

The process of homogenization (i.e. the use of information at the micro-scale to determine macroscale properties) has already been mentioned in earlier sections.

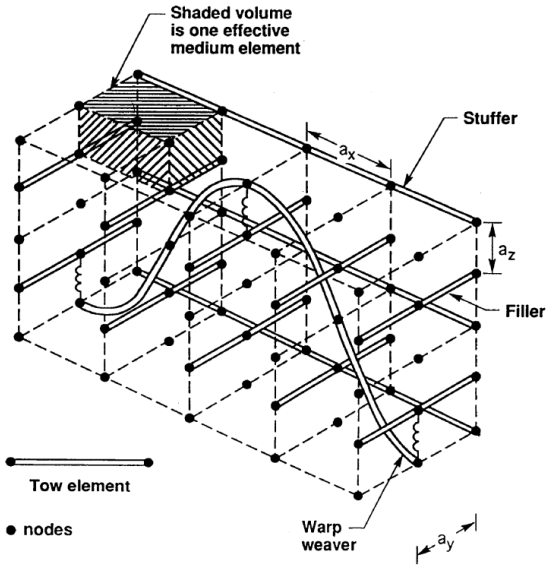

Figure 2.12: **The binary model** superposition of tow elements onto an effective medium continuum [65]

In addition to the previously mentioned work, it is worth mentioning the work of Sherburn [70], who developed geometric models for the tow scale, incorporating changes at the micro scale from interactions between adjacent tows. This was used in a multi-scale model of 3D weaved composites up to the RUC scale, where the effect of tow distortion was observed. Wang et al. [71] also attempt to define a geometric model for the periodic RUC, using Hermite splines to model the tow path in 3D weaves.

2.3.4 Conclusions

The literature review has examined a number of methods for material homogenization, structural analysis, damage modelling, and multi-scale simulation, and it is clear that each method has its own objectives. The majority of the research has focussed on laminated forms, especially in the area of damage modelling. With some exceptions, most work on 3D weaved composites has focussed on homogenization techniques. As yet, no single technique has emerged that is capable of modelling components at the macroscale, with consideration for the microstructure and damage present in the complex 3D weave form. To achieve this, the key is likely to be the use of automatic model adaptivity to provide detailed modelling where necessary, and maintain efficiency wherever possible.

For the purpose of modelling the behaviour of 3D weaved composites, it would seem appropriate to build upon the body of research on laminated composites. This should be possible since the structure of the 3D weave is very similar to the laminate form, with the addition of transverse reinforcement fibres.

Chapter 3

A two-scale layerwise method

3.1 Introduction

For the developement of a general purpose numerical method for multiscale analysis, a capable and efficient mesoscale process is essential. This can provide a foundation upon which the microscale analysis (tow/matrix scale), macroscale analysis (structural scale) and damage modelling can be added.

Three-dimensional weaved composites can be considered, as seen in the literature, as a form of laminated composite with additional through-thickness strengthening fibres. Since much work has been performed in the analysis of laminated composites, the first stage of this research is focussed on developing the existing methods in preparation for extension to use on 3D weave forms.

The model that is developed here is based on the layerwise 'variable kinematic' model developed by Robbins and Reddy [53]. The model as presented in [53] is a plate model, combining an FSDT displacement field with a Lagrangian interpolated layerwise field and a discontinuous field using the Heaviside function to represent delamination.

In this research, a model is developed to allow the superposition of any two arbitrary displacement fields (and thus any number of displacement fields by repeated application). The use of plate models is appropriate due to the nature of the structure of 3D weave composites (thickness dimension $h \ll a$, the in-plane dimension), and the dimensional reduction achieves an increase in efficiency over full 3D models.

It is described here as a two-scale model as it allows the combination of a model homogenizing the plies into an equivalent single layer (termed the macro-scale in this work), and a ply- (or meso-) scale model to accurately determine interlaminar stresses.

Here, the model is presented as an extrinsic enhancement (addition of extra degrees of freedom) to the finite element method, an approach common in XFEM analysis.

3.2 Literature review on laminate theory and multiscale methods

Typically for the analysis of thin structures, plate or shell elements are used, producing a model where certain assumptions are made about the displacement field, and the number of degrees-of-freedom are reduced greatly from a full 3D analysis. These are collectively known as the equivalent single layer (ESL) models. Classical plate theory is extended to laminar forms to give classical laminate theory (CLT). Here, the assumption is made that for a thin laminate structure, there is zero transverse (through-thickness) strain, and the in-plane displacement components can be represented by a linear through-thickness function (Figure 3.1):

$$\begin{aligned} u(x,y,z) &= u_0(x,y) - z\frac{\partial w}{\partial x} \\ v(x,y,z) &= v_0(x,y) - z\frac{\partial w}{\partial y} \\ w(x,y,z) &= w_0(x,y) \end{aligned} \tag{3.1}$$

where u, v, w are the displacements in the x, y, z-directions respectively, and the subscript 0 indicates the value of the displacement on an arbitrary plane (e.g. the midplane).

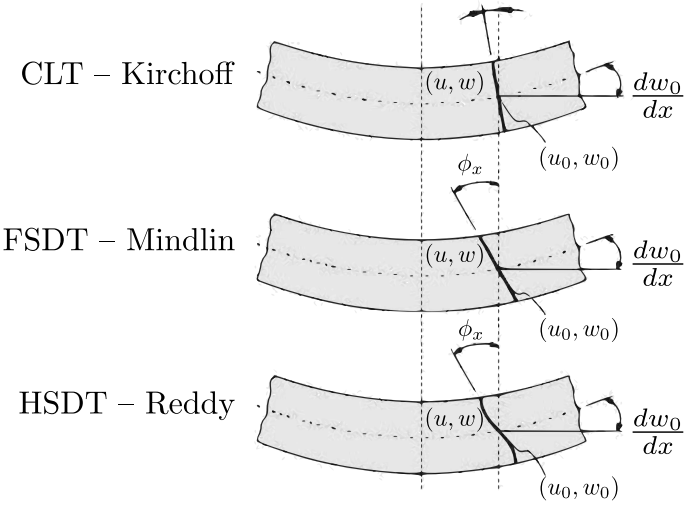

Figure 3.1: **Equivalent single layer models** (a) classical laminate theory; (b) first order shear deformation theory; (c) higher order shear deformation theory

From this definition of the displacement field, the strain field can also be derived. It should be noted that the assumptions made on the displacement field constrain the strain to be a continuous function across the thickness, despite not having made any constraint on the nature of the lamina.

Using the familiar principle of virtual displacements, or the equilibrium of the work done by the internal and external forces, equations can be derived for the

CLT. Such derivations can be found in a number of texts, such as Ochoa and Reddy [72], Reddy [73, 74]. This reduction of a 3D elasticity problem to a 2D problem greatly increases the efficiency of the FEM, both in terms of the time required to set up the model, and the computational cost involved in solving the model. This is because the displacement of any point within the laminate is a function of just three degrees of freedom (u_0, v_0, w_0), regardless of number of lamina.

The cost of such a simplified solution is the inability of the model to provide some of the information that a more complete solution would. In the case of CLT, the assumption of $\varepsilon_{zz} = 0$ leads to a solution with no transverse direct stress, i.e. $\sigma_{zz} = 0$.

A common refinement to the CLT is the first-order shear deformation theory (FSDT) or Mindlin plate theory. This adds two degrees of freedom to give the displacement field:

$$\begin{aligned} u(x,y,z) &= u_0(x,y) + z\phi_1(x,y) \\ v(x,y,z) &= v_0(x,y) + z\phi_2(x,y) \\ w(x,y,z) &= w_0(x,y) \end{aligned} \tag{3.2}$$

The additional degrees of freedom, ϕ_1 and ϕ_2 represent the rotation of the normal to the plate about the y and x axes respectively. The addition of these two variables enable the resolution of a constant through-thickness shear strain. Whilst this is additional information compared to CLT, the FSDT remains unable to resolve direct transverse strains, and the value of an averaged transverse shear strain is questionable.

Higher order versions of the FSDT exist (higher order shear deformation theory, HSDT), but a fundamental shortcoming of this and all the ESL models remains: the constraint for a continuous through-thickness strain.

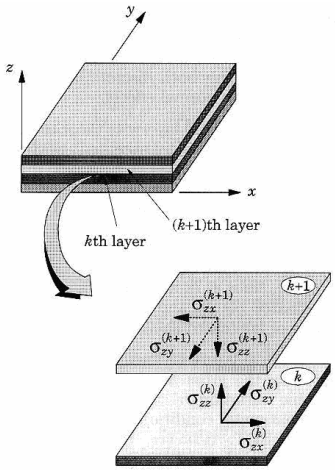

Figure 3.2: **Continuity of transverse stresses at lamina interfaces in laminar composite** [75]

In general, we expect continuity for the through-thickness stresses at the interfaces

(Figure 3.2). In a layered composite:

$$\begin{Bmatrix} \sigma_{xz} \\ \sigma_{yz} \\ \sigma_{zz} \end{Bmatrix}^{(k)} = \begin{Bmatrix} \sigma_{xz} \\ \sigma_{yz} \\ \sigma_{zz} \end{Bmatrix}^{(k+1)} \tag{3.3}$$

In layer k, the stresses are given by

$$\{\sigma\}^{(k)} = \left[C\right]^{(k)} \{\varepsilon\}^{(k)} \tag{3.4}$$

Since, in general, $\left[C\right]^{(k)} \neq \left[C\right]^{(k+1)}$, we get:

$$\begin{Bmatrix} \gamma_{xz} \\ \gamma_{yz} \\ \varepsilon_{zz} \end{Bmatrix}^{(k)} \neq \begin{Bmatrix} \gamma_{xz} \\ \gamma_{yz} \\ \varepsilon_{zz} \end{Bmatrix}^{(k+1)} \tag{3.5}$$

i.e. the transverse strains will be discontinuous. The strains are given as the derivatives of the displacements, and the form of the displacement field given in (3.1) for CLT and (3.2) for FSDT are both continuous and continuously derivable. Thus, the ESL models can not accurately model the discontinuous transverse strain.

To overcome this, separate displacement fields are required in each layer. The requirement for continuity of the displacement at the interfaces remains, but there is no requirement for the field to be continuously differentiable, i.e. it should be C^0-continuous. This condition forms the basis of a class of methods known as **'layerwise'**.

Before progressing, it is worth mentioning that despite the inability of ESL models to accurately model transverse stress or strain, the models are acceptable where this information is not required, and the assumptions made on through-thickness strains hold true. Reddy [75] mentions that this is the case for 'thin' laminates, ones with a ratio of $a/h > 10$, where a is an in-plane dimension and h is the thickness of the laminate.

Layerwise models

The layerwise models solve the problems of the ESL models by assuming that the through-thickness displacement field in a laminar composite can be represented in a piecewise manner. Thus, the displacement field can maintain inter-laminar continuity, yet the derivatives of the displacement field can be discontinuous where necessary. In the case of a laminate, the piecewise structure of the displacement field will coincide with the lamina structure (Figure 3.3).

The requirement for a piecewise field immediately increases the complexity of the model to give a number of degrees-of-freedom in the model that is proportional to the

through-thickness discretization. In general, the form of the displacement field is:

$$u^{(k)}(x,y,z) = u_0^{(k)}(x,y) + \sum_{j=1}^{n} u_j^{(k)}(x,y) f^{(k)}(z)$$
$$v^{(k)}(x,y,z) = v_0^{(k)}(x,y) + \sum_{j=1}^{n} v_j^{(k)}(x,y) g^{(k)}(z)$$
$$w^{(k)}(x,y,z) = w_0^{(k)}(x,y) + \sum_{j=1}^{n} w_j^{(k)}(x,y) h^{(k)}(z) \tag{3.6}$$

where k represents the mathematical layers (ordinarily coinciding with the physical layers in the laminate), u_0, v_0 and w_0 are displacements on an arbitrary plane, u_j, v_j and w_j are the discrete displacements on interface j at location (x,y), and f, g and h are functions of the thickness coordinate z to achieve the required C^0-continuity.

A number of methods for defining a C^0-continuous field exist, as referenced by Reddy [76], Reddy and Robbins [77]. Most of these theories use constraint equations to enforce the displacement continuity. One method, described in Robbins and Reddy [78], uses a one-dimensional Lagrangian interpolation polynomial (Figure 3.3) to achieve the required properties.

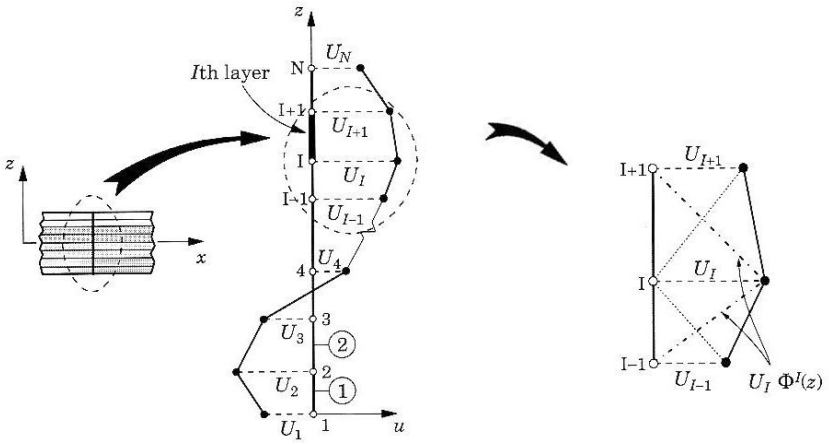

Figure 3.3: **Layerwise discretization using Lagrange interpolation** showing linear approximation functions Φ^I [75]

The layerwise field described by Reddy [75] is a special case of (3.6):

$$u(x,y,z) = \sum_{I=1}^{n} U_I(x,y)\Phi^I(z)$$
$$v(x,y,z) = \sum_{I=1}^{n} V_I(x,y)\Phi^I(z)$$
$$w(x,y,z) = \sum_{I=1}^{m} W_I(x,y)\Psi^I(z) \tag{3.7}$$

where U, V and W are nodal values of u, v and w, and Φ and Ψ are global interpolation functions for the in-plane and transverse displacements respectively. The example of a linear Lagrange interpolation is given:

$$\begin{aligned} \Phi^I(z) &= \psi_2^{I-1}(z), & z_{I-1} \leq z \leq z_I \\ \Phi^I(z) &= \psi_1^I(z), & z_I \leq z \leq z_{I+1} \end{aligned} \tag{3.8}$$

$$\psi_1^{(k)} = 1 - \frac{\bar{z}}{h_k}, \qquad \psi_2^{(k)} = \frac{\bar{z}}{h_k}, \qquad 0 \leq \bar{z} \leq h_k \tag{3.9}$$

where z is the through-thickness coordinate, z_I and z_{I+1} are the lower and upper extents of layer I, h_k is the thickness of layer k and $\bar{z}$ is the local z-coordinate within a layer.

This layerwise method is developed into a finite element formulation using von Kármán strains and the principle of virtual displacements. Reddy demonstrates this model to be equivalent in terms of accuracy to a full 3D FEM solution whilst being more computationally efficient [75].

This type of layerwise model has been extended in a number of ways, e.g. by Kassegne [79] to account for stiffening members, by Reddy et al. [38] to model progressive damage, and by Robbins and Reddy [53] to model delamination and to incorporate a multiscale-type approach. Further extensions are given by Dakshina Moorthy and Reddy [80], who develops a layerwise element with enhanced strains, and by Carrera and Demasi [81, 82], who use the Reissner mixed variational theorem as an alternative to the principle of virtual displacements to impose directly the continuity condition for the transverse direct and shear streses.

Another common method for modelling the discontinuous field in a layered composite is to use the zig-zag function[1]. Murakami [83] introduced a zig-zag function, shown in Figure 3.4, of the form [84]:

$$M(z) = (-1)^k \xi_k \tag{3.10}$$

where $-1 \leq \xi_k \leq 1$ is a non-dimensional thickness coordinate for layer k. The exponent k alternates the sign of the Murakami zig-zag function in each layer (and thus the derivative with respect to z, M'). The zig-zag function meets the criteria for a C^0-continuous field.

The function can be augmented to other theories with the addition of a suitable number of degrees-of-freedom, e.g. to the FSDT [85]:

$$\begin{aligned} u(x,y,z) &= u_0(x,y) + z\phi_1(x,y) + M(z)u_M \\ v(x,y,z) &= v_0(x,y) + z\phi_2(x,y) + M(z)v_M \\ w(x,y,z) &= w_0(x,y) \end{aligned} \tag{3.11}$$

[1] In some of the literature, the term *zig-zag* is used to denote any theory that implements a piecewise form for the transverse displacement field. In this review, zig-zag is reserved for the theory of Murakami.

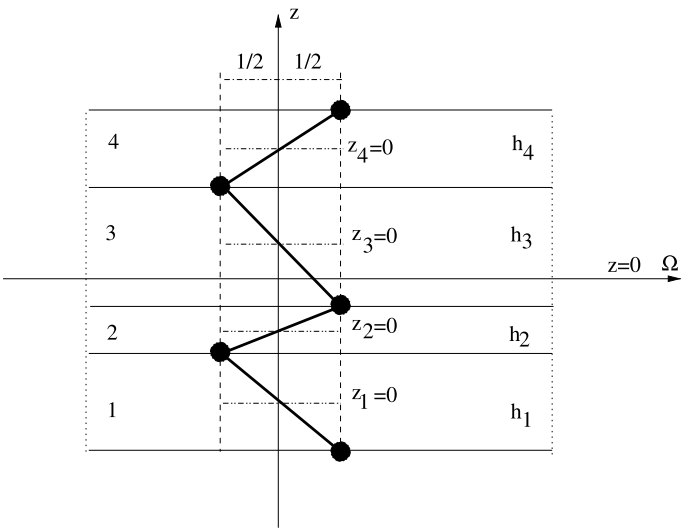

Figure 3.4: **Murakami zig-zag function** Example given for a 4-layered laminate [85]

Carrera [84, 85] has reviewed the use of Murakami zig-zag functions in both the simple forms as described above, and in mixed-variational formulations, and has found it to be superior to the ESL models. The conclusions are that the incorporation of zig-zag functions are more effective than the introduction of higher order functions (often referred to as *p*-refinement) in an ESL model. This is consistent with the understanding of the limitations of the ESL models. Demasi [86] also conducts a review, and additionally concludes that for better approximation of local effects, and in particular for the study of thick plates, full 3D or more advanced layerwise models are required.

A number of reviews have been published into the various displacement formulations available for plate models of laminar composites. Among the more recent are Mohite and Upadhyay [87] and Rohwer et al. [88]. Both these reviews cover all the models summarized here. Carrera [89] focusses on the implementation of these models using a Reissener mixed variational approach to derive the governing equations. Reddy and Robbins [77] also review many of the same models, and focusses on models such as 'partial layerwise theory' and 'generalized layerwise theory' that would go on to become the 'layerwise theory of Reddy'. [77] also devotes much space to 'simultaneous multiple methods' and 'variable kinematic formulations', methods of combining ESL and layerwise models.

3.3 Aims

The aim of the process developed here is to produce a model capable of simulating the component or macro-scale, whilst resolving ply-scale displacements and stresses in

regions of interest, thereby improving the quality of the results from the CLT method, without increasing the problem size to the extent of using a complete layerwise or full 3D model.

3.4 Method

3.4.1 Displacement field definition

The displacement field in the composite is defined as the summation of two separate displacement fields:

$$\boldsymbol{u} = \boldsymbol{u}^{\alpha} + \boldsymbol{u}^{\beta} \tag{3.12}$$

where $\boldsymbol{u}$ is the vector displacement at an arbitrary point within the three-dimensional analysis domain Ω, and the superscripts α and β refer to the components of the different displacement fields. It will be shown later that by deriving the coupling terms between two displacement fields is sufficient to allow, by a chain process, the addition of any number of further displacement fields.

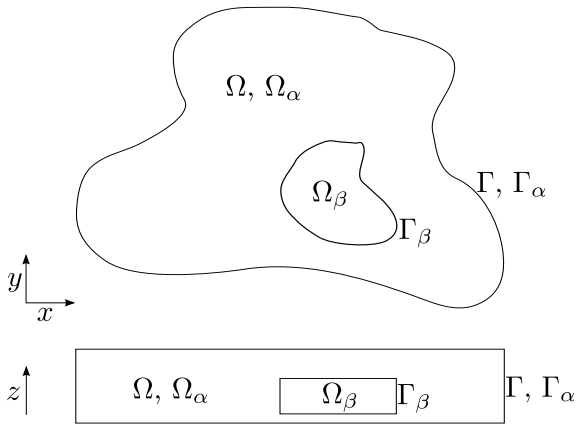

Figure 3.5: **Representation of domains** Domain Ω, bounded by Γ, represented by mathematical domain Ω_α (Γ_α), and the superimposed domain Ω_β (Γ_β), shown in plan and in section

As is the nature of plate fields, the through-thickness variation of the displacement fields are assumed to conform to a given form. Additionally, the displacement field is assumed to be piecewise in the through-thickness (z-) direction:

$$\boldsymbol{u}^{\alpha} = \sum_{I=1}^{N^{\alpha}} \boldsymbol{U}_I^{\alpha}(x,y)\phi^{\alpha}(z) \tag{3.13}$$

where α represents the displacement field (α or β), N^{α} is the piecewise discretisation of field α, $\boldsymbol{U}_I$ is the value of $\boldsymbol{u}_I$ on the two-dimensional analysis domain ω_I, and ϕ^{α} is

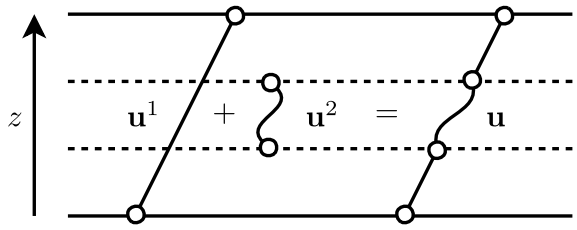

Figure 3.6: **Superposition of multiple displacement definitions** Displacement $\boldsymbol{u}^1$ is locally enhanced by a higher order displacement definition $\boldsymbol{u}^2$ to give total displacement $\boldsymbol{u}$

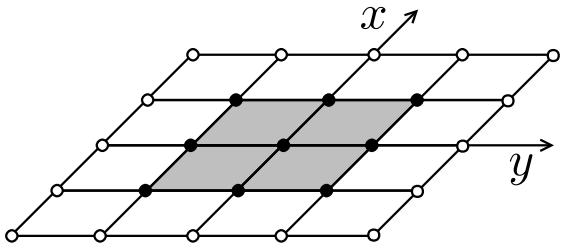

(a) In-plane 2D discretization, where filled nodes are expanded with a transverse displacement function illustrated in 3.7(b)

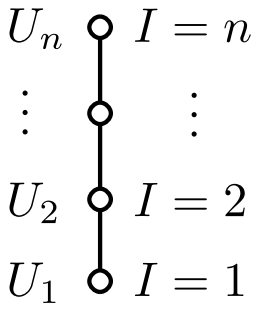

(b) Out-of-plane discretization, representing transverse expansion of the filled nodes in 3.7(a)

Figure 3.7: **Separation of in-plane and out of plane displacements**

the through-thickness function of z. The separation of the discretization is illustrated in Figure 3.7.

In this XFEM implementation, the value of the displacement field in domain ω_I is given by a finite element discretization in-plane:

$$\boldsymbol{U}_I^\alpha = \sum_{J=1}^{M} \boldsymbol{a}_J^\alpha \psi^\alpha(x,y) \tag{3.14}$$

where $\boldsymbol{a}$ are nodal values of the displacement on ω_I, and ψ are 2D interpolation functions.

3.4.2 Strain formulation

The displacement field of (3.12) is used to derive the strains using the relationship $\boldsymbol{\varepsilon} = \nabla \boldsymbol{u}$, and the von Kármán non-linear strain definition:

$$\begin{aligned}\varepsilon_{xx} = &\sum_{I=1}^{N^\alpha} \frac{\partial U_I^\alpha}{\partial x}\phi_I^\alpha + \frac{1}{2}\left(\sum_{I=1}^{N^\alpha} \frac{\partial W_I^\alpha}{\partial x}\phi_I^\alpha\right)\left(\sum_{J=1}^{N^\alpha} \frac{\partial W_J^\alpha}{\partial x}\phi_J^\alpha\right) \\ &+ \sum_{I=1}^{N^\beta} \frac{\partial U_I^\beta}{\partial x}\phi_I^\beta + \frac{1}{2}\left(\sum_{I=1}^{N^\beta} \frac{\partial W_I^\beta}{\partial x}\phi_I^\beta\right)\left(\sum_{J=1}^{N^\beta} \frac{\partial W_J^\beta}{\partial x}\phi_J^\beta\right) \\ &+ \left(\sum_{I=1}^{N^\alpha} \frac{\partial W_I^\alpha}{\partial x}\phi_I^\alpha\right)\left(\sum_{J=1}^{N^\beta} \frac{\partial W_J^\beta}{\partial x}\phi_J^\beta\right)\end{aligned} \tag{3.15a}$$

$$\begin{aligned}\varepsilon_{yy} = &\sum_{I=1}^{N^\alpha} \frac{\partial V_I^\alpha}{\partial y}\phi_I^\alpha + \frac{1}{2}\left(\sum_{I=1}^{N^\alpha} \frac{\partial W_I^\alpha}{\partial y}\phi_I^\alpha\right)\left(\sum_{J=1}^{N^\alpha} \frac{\partial W_J^\alpha}{\partial y}\phi_J^\alpha\right) \\ &+ \sum_{I=1}^{N^\beta} \frac{\partial V_I^\beta}{\partial y}\phi_I^\beta + \frac{1}{2}\left(\sum_{I=1}^{N^\beta} \frac{\partial W_I^\beta}{\partial y}\phi_I^\beta\right)\left(\sum_{J=1}^{N^\beta} \frac{\partial W_J^\beta}{\partial y}\phi_J^\beta\right) \\ &+ \left(\sum_{I=1}^{N^\alpha} \frac{\partial W_I^\alpha}{\partial y}\phi_I^\alpha\right)\left(\sum_{J=1}^{N^\beta} \frac{\partial W_J^\beta}{\partial y}\phi_J^\beta\right)\end{aligned} \tag{3.15b}$$

$$\varepsilon_{zz} = \sum_{I=1}^{N^\alpha} W_I^\alpha \frac{\partial \phi_I^\alpha}{\partial z} + \sum_{I=1}^{N^\beta} W_I^\beta \frac{\partial \phi_I^\beta}{\partial z} \tag{3.15c}$$

$$\begin{aligned}\gamma_{yz} = &\sum_{I=1}^{N^\alpha} V_I^\alpha \frac{\partial \phi_I^\alpha}{\partial z} + \sum_{I=1}^{N^\alpha} \frac{\partial W_I^\alpha}{\partial y}\phi_I^\alpha \\ &+ \sum_{I=1}^{N^\beta} V_I^\beta \frac{\partial \phi_I^\beta}{\partial z} + \sum_{I=1}^{N^\beta} \frac{\partial W_I^\beta}{\partial y}\phi_I^\beta\end{aligned} \tag{3.15d}$$

$$\begin{aligned}\gamma_{zx} = &\sum_{I=1}^{N^\alpha} U_I^\alpha \frac{\partial \phi_I^\alpha}{\partial z} + \sum_{I=1}^{N^\alpha} \frac{\partial W_I^\alpha}{\partial x}\phi_I^\alpha \\ &+ \sum_{I=1}^{N^\beta} U_I^\beta \frac{\partial \phi_I^\beta}{\partial z} + \sum_{I=1}^{N^\beta} \frac{\partial W_I^\beta}{\partial x}\phi_I^\beta\end{aligned} \tag{3.15e}$$

$$\begin{aligned}\gamma_{xy} = &\sum_{I=1}^{N^\alpha}\left(\frac{\partial U_I^\alpha}{\partial y} + \frac{\partial V_I^\alpha}{\partial x}\right)\phi_I^\alpha + \left(\sum_{I=1}^{N^\alpha}\frac{\partial W_I^\alpha}{\partial x}\phi_I^\alpha\right)\left(\sum_{J=1}^{N^\alpha}\frac{\partial W_J^\alpha}{\partial y}\phi_J^\alpha\right) \\ &+ \sum_{I=1}^{N^\beta}\left(\frac{\partial U_I^\beta}{\partial y} + \frac{\partial V_I^\beta}{\partial x}\right)\phi_I^\beta + \left(\sum_{I=1}^{N^\beta}\frac{\partial W_I^\beta}{\partial x}\phi_I^\beta\right)\left(\sum_{J=1}^{N^\beta}\frac{\partial W_J^\beta}{\partial y}\phi_J^\beta\right) \\ &+ \left(\sum_{I=1}^{N^\alpha}\frac{\partial W_I^\alpha}{\partial x}\phi_I^\alpha\right)\left(\sum_{J=1}^{N^\beta}\frac{\partial W_J^\beta}{\partial y}\phi_J^\beta\right) + \left(\sum_{I=1}^{N^\alpha}\frac{\partial W_I^\alpha}{\partial y}\phi_I^\alpha\right)\left(\sum_{J=1}^{N^\beta}\frac{\partial W_J^\beta}{\partial x}\phi_J^\beta\right)\end{aligned} \tag{3.15f}$$

where U, V and W are the displacement components of $\boldsymbol{U}$ in directions x, y, z.

Examining (3.15), it can be seen that the terms either contain reference to one displacement field only (α or β), or contain 'coupling' terms relating the strain to the interactions between the displacement fields.

3.4.3 Virtual strain energy

To solve for the displacements, a variational approach using the principle of virtual displacments is used. The virtual strain energy in the domain is given by:

$$\delta U = \int_\Omega \left\{\sigma_{xx}\delta\varepsilon_{xx} + \sigma_{yy}\delta\varepsilon_{yy} + \sigma_{zz}\delta\varepsilon_{zz} + \sigma_{yz}\delta\gamma_{yz} + \sigma_{zx}\delta\gamma_{zx} + \sigma_{xy}\delta\gamma_{xy}\right\} \mathrm{d}\Omega \tag{3.16}$$

Performing this integration piecewise by material layers, i.e. for Ne material layers:

$$\int_\Omega \left\{f(x,y,z)\right\} \mathrm{d}\Omega = \int_\omega \left\{\sum_{k=1}^{Ne}\int_{z_b^k}^{z_t^k} \left\{f(x,y,z)\right\} \mathrm{d}z\right\} \mathrm{d}y\,\mathrm{d}x \tag{3.17}$$

the following terms can be defined:

$$\begin{aligned}\left\{N_1^\gamma \quad N_2^\gamma \quad N_4^\gamma \quad N_5^\gamma \quad N_6^\gamma\right\}^T &= \sum_{k=1}^{Ne}\int_{z_b^k}^{z_t^k} \left\{\sigma_{xx} \quad \sigma_{yy} \quad \sigma_{yz} \quad \sigma_{zx} \quad \sigma_{xy}\right\}^T \phi_I^\gamma \,\mathrm{d}z \\ \left\{\tilde{N}_3^\gamma \quad \tilde{N}_4^\gamma \quad \tilde{N}_5^\gamma\right\}^T &= \sum_{k=1}^{Ne}\int_{z_b^k}^{z_t^k} \left\{\sigma_{zz} \quad \sigma_{yz} \quad \sigma_{zx}\right\}^T \frac{\mathrm{d}\phi_I^\gamma}{\mathrm{d}z} \,\mathrm{d}z \\ \left\{M_{1}^{\gamma\delta} \quad M_{2}^{\gamma\delta} \quad M_{6}^{\gamma\delta}\right\}^T_{IJ} &= \sum_{k=1}^{Ne}\int_{z_b^k}^{z_t^k} \left\{\sigma_{xx} \quad \sigma_{yy} \quad \sigma_{xy}\right\}^T \phi_I^\gamma \phi_J^\delta \,\mathrm{d}z\end{aligned} \tag{3.18}$$

where γ and δ are dummy variables representing one of the displacement fields α or β. Using these definitions, the virtual strain energy, (3.16), can be written:

$$\begin{aligned}
\delta U = &\int_\omega \sum_{I=1}^{N^\alpha} \Bigg\{ N_{1}^{\alpha}{}_{I} \frac{\partial \delta U_I^\alpha}{\partial x} + N_{2}^{\alpha}{}_{I} \frac{\partial \delta V_I^\alpha}{\partial y} + N_{4}^{\alpha}{}_{I} \frac{\partial \delta W_I^\alpha}{\partial y} + N_{5}^{\alpha}{}_{I} \frac{\partial \delta W_I^\alpha}{\partial x} + N_{6}^{\alpha}{}_{I} \left(\frac{\partial \delta U_I^\alpha}{\partial y} + \frac{\partial \delta V_I^\alpha}{\partial x} \right) \\
&\qquad + \tilde{N}_{3}^{\alpha}{}_{I} \delta W_I^\alpha + \tilde{N}_{4}^{\alpha}{}_{I} \delta V_I^\alpha + \tilde{N}_{5}^{\alpha}{}_{I} \delta U_I^\alpha \Bigg\} \mathrm{d}y \, \mathrm{d}x \\
&+ \int_\omega \sum_{I=1}^{N^\beta} \Bigg\{ N_{1}^{\beta}{}_{I} \frac{\partial \delta U_I^\beta}{\partial x} + N_{2}^{\beta}{}_{I} \frac{\partial \delta V_I^\beta}{\partial y} + N_{4}^{\beta}{}_{I} \frac{\partial \delta W_I^\beta}{\partial y} + N_{5}^{\beta}{}_{I} \frac{\partial \delta W_I^\beta}{\partial x} + N_{6}^{\beta}{}_{I} \left(\frac{\partial \delta U_I^\beta}{\partial y} + \frac{\partial \delta V_I^\beta}{\partial x} \right) \\
&\qquad + \tilde{N}_{3}^{\beta}{}_{I} \delta W_I^\beta + \tilde{N}_{4}^{\beta}{}_{I} \delta V_I^\beta + \tilde{N}_{5}^{\beta}{}_{I} \delta U_I^\beta \Bigg\} \mathrm{d}y \, \mathrm{d}x \\
&+ \int_\omega \sum_{I,J=1}^{N^\alpha} \left\{ \frac{1}{2} M_{1}^{\alpha\alpha}{}_{IJ} \frac{\partial \delta W_I^\alpha}{\partial x} \frac{\partial \delta W_J^\alpha}{\partial x} + \frac{1}{2} M_{2}^{\alpha\alpha}{}_{IJ} \frac{\partial \delta W_I^\alpha}{\partial y} \frac{\partial \delta W_J^\alpha}{\partial y} + M_{6}^{\alpha\alpha}{}_{IJ} \frac{\partial \delta W_I^\alpha}{\partial x} \frac{\partial \delta W_J^\alpha}{\partial y} \right\} \mathrm{d}y \, \mathrm{d}x \\
&+ \int_\omega \sum_{I,J=1}^{N^\beta} \left\{ \frac{1}{2} M_{1}^{\beta\beta}{}_{IJ} \frac{\partial \delta W_I^\beta}{\partial x} \frac{\partial \delta W_J^\beta}{\partial x} + \frac{1}{2} M_{2}^{\beta\beta}{}_{IJ} \frac{\partial \delta W_I^\beta}{\partial y} \frac{\partial \delta W_J^\beta}{\partial y} + M_{6}^{\beta\beta}{}_{IJ} \frac{\partial \delta W_I^\beta}{\partial x} \frac{\partial \delta W_J^\beta}{\partial y} \right\} \mathrm{d}y \, \mathrm{d}x \\
&+ \int_\omega \sum_{I=1}^{N^\alpha} \sum_{J=1}^{N^\beta} \Bigg\{ M_{1}^{\alpha\beta}{}_{IJ} \frac{\partial \delta W_I^\alpha}{\partial x} \frac{\partial \delta W_J^\beta}{\partial x} + M_{2}^{\alpha\beta}{}_{IJ} \frac{\partial \delta W_I^\alpha}{\partial y} \frac{\partial \delta W_J^\beta}{\partial y} \\
&\qquad + M_{6}^{\alpha\beta}{}_{IJ} \left(\frac{\partial \delta W_I^\alpha}{\partial x} \frac{\partial \delta W_J^\beta}{\partial y} + \frac{\partial \delta W_I^\alpha}{\partial y} \frac{\partial \delta W_J^\beta}{\partial x} \right) \Bigg\} \mathrm{d}y \, \mathrm{d}x
\end{aligned} \tag{3.19}$$

3.4.4 Further expansion of the N and M terms

Using the stress-strain relationship for a given layer k:

$$\begin{Bmatrix} \sigma_{xx} \\ \sigma_{yy} \\ \sigma_{zz} \\ \sigma_{yz} \\ \sigma_{zx} \\ \sigma_{xy} \end{Bmatrix}^{(k)} = \begin{bmatrix} \bar{c}_{11}^{(k)} & \bar{c}_{12}^{(k)} & \bar{c}_{13}^{(k)} & 0 & 0 & \bar{c}_{16}^{(k)} \\ \bar{c}_{21}^{(k)} & \bar{c}_{22}^{(k)} & \bar{c}_{23}^{(k)} & 0 & 0 & \bar{c}_{26}^{(k)} \\ \bar{c}_{31}^{(k)} & \bar{c}_{32}^{(k)} & \bar{c}_{33}^{(k)} & 0 & 0 & \bar{c}_{36}^{(k)} \\ 0 & 0 & 0 & \bar{c}_{44}^{(k)} & \bar{c}_{45}^{(k)} & 0 \\ 0 & 0 & 0 & \bar{c}_{54}^{(k)} & \bar{c}_{55}^{(k)} & 0 \\ \bar{c}_{61}^{(k)} & \bar{c}_{62}^{(k)} & \bar{c}_{63}^{(k)} & 0 & 0 & \bar{c}_{66}^{(k)} \end{bmatrix}^{(k)} \begin{Bmatrix} \varepsilon_{xx} \\ \varepsilon_{yy} \\ \varepsilon_{zz} \\ \gamma_{yz} \\ \gamma_{zx} \\ \gamma_{xy} \end{Bmatrix}^{(k)} \tag{3.20}$$

and defining the following coefficients:

$$\begin{aligned}
A_{ij}^{\alpha\beta}{}_{IJ} &= \sum_{k=1}^{Ne} \int_{z_b^k}^{z_t^k} \bar{c}_{ij}^{(k)} \phi_I^\alpha \phi_J^\beta \, \mathrm{d}z & \bar{A}_{ij}^{\alpha\beta}{}_{IJ} &= \sum_{k=1}^{Ne} \int_{z_b^k}^{z_t^k} \bar{c}_{ij}^{(k)} \phi_I^\alpha \frac{\partial \phi_J^\beta}{\partial z} \, \mathrm{d}z \\
\bar{\bar{A}}_{ij}^{\alpha\beta}{}_{IJ} &= \sum_{k=1}^{Ne} \int_{z_b^k}^{z_t^k} \bar{c}_{ij}^{(k)} \frac{\partial \phi_I^\alpha}{\partial z} \frac{\partial \phi_J^\beta}{\partial z} \, \mathrm{d}z & B_{ij}^{\alpha\beta\gamma}{}_{IJK} &= \sum_{k=1}^{Ne} \int_{z_b^k}^{z_t^k} \bar{c}_{ij}^{(k)} \phi_I^\alpha \phi_J^\beta \phi_K^\gamma \, \mathrm{d}z \\
\bar{B}_{ij}^{\alpha\beta\gamma}{}_{IJK} &= \sum_{k=1}^{Ne} \int_{z_b^k}^{z_t^k} \bar{c}_{ij}^{(k)} \phi_I^\alpha \phi_J^\beta \frac{\partial \phi_K^\gamma}{\partial z} \, \mathrm{d}z & D_{ij}^{\alpha\beta\gamma\delta}{}_{IJKL} &= \sum_{k=1}^{Ne} \int_{z_b^k}^{z_t^k} \bar{c}_{ij}^{(k)} \phi_I^\alpha \phi_J^\beta \phi_K^\gamma \phi_L^\delta \, \mathrm{d}z
\end{aligned} \tag{3.21}$$

where $\alpha, \beta, \gamma, \delta$ superscripts refer to one of the displacement fields, the terms in (3.18) can be expanded:

$$
\begin{aligned}
N_{\substack{i=1,2,6}}^{\gamma}{}_{I} = & \sum_{J=1}^{N^\alpha}\left\{ A_{i1}^{\gamma\alpha}{}_{IJ}\frac{\partial U_J^\alpha}{\partial x} + A_{i2}^{\gamma\alpha}{}_{IJ}\frac{\partial V_J^\alpha}{\partial y} + \bar{A}_{i3}^{\gamma\alpha}{}_{IJ} W_J^\alpha + A_{i6}^{\gamma\alpha}{}_{IJ}\left(\frac{\partial U_J^\alpha}{\partial y} + \frac{\partial V_J^\alpha}{\partial x}\right)\right\} \\
& + \sum_{J=1}^{N^\beta}\left\{ A_{i1}^{\gamma\beta}{}_{IJ}\frac{\partial U_J^\beta}{\partial x} + A_{i2}^{\gamma\beta}{}_{IJ}\frac{\partial V_J^\beta}{\partial y} + \bar{A}_{i3}^{\gamma\beta}{}_{IJ} W_J^\beta + A_{i6}^{\gamma\beta}{}_{IJ}\left(\frac{\partial U_J^\beta}{\partial y} + \frac{\partial V_J^\beta}{\partial x}\right)\right\} \\
& + \sum_{J,K=1}^{N^\alpha}\left\{ \frac{1}{2} B_{i1}^{\gamma\alpha\alpha}{}_{IJK}\frac{\partial W_J^\alpha}{\partial x}\frac{\partial W_K^\alpha}{\partial x} + \frac{1}{2} B_{i2}^{\gamma\alpha\alpha}{}_{IJK}\frac{\partial W_J^\alpha}{\partial y}\frac{\partial W_K^\alpha}{\partial y} \right. \\
& \qquad \left. + B_{i6}^{\gamma\alpha\alpha}{}_{IJK}\frac{\partial W_J^\alpha}{\partial x}\frac{\partial W_K^\alpha}{\partial y}\right\} \\
& + \sum_{J,K=1}^{N^\beta}\left\{ \frac{1}{2} B_{i1}^{\gamma\beta\beta}{}_{IJK}\frac{\partial W_J^\beta}{\partial x}\frac{\partial W_K^\beta}{\partial x} + \frac{1}{2} B_{i2}^{\gamma\beta\beta}{}_{IJK}\frac{\partial W_J^\beta}{\partial y}\frac{\partial W_K^\beta}{\partial y} \right. \\
& \qquad \left. + B_{i6}^{\gamma\beta\beta}{}_{IJK}\frac{\partial W_J^\beta}{\partial x}\frac{\partial W_K^\beta}{\partial y}\right\} \\
& + \sum_{J=1}^{N^\alpha}\sum_{K=1}^{N^\beta}\left\{ B_{i1}^{\gamma\alpha\beta}{}_{IJK}\frac{\partial W_J^\alpha}{\partial x}\frac{\partial W_K^\beta}{\partial x} + B_{i2}^{\gamma\alpha\beta}{}_{IJK}\frac{\partial W_J^\alpha}{\partial y}\frac{\partial W_K^\beta}{\partial y} \right. \\
& \qquad \left. + B_{i6}^{\gamma\alpha\beta}{}_{IJK}\left(\frac{\partial W_J^\alpha}{\partial x}\frac{\partial W_K^\beta}{\partial y} + \frac{\partial W_J^\alpha}{\partial y}\frac{\partial W_K^\beta}{\partial x}\right)\right\}
\end{aligned}
\tag{3.22a}
$$

$$
\begin{aligned}
N_{\substack{i=4,5}}^{\gamma}{}_{I} = & \sum_{J=1}^{N^\alpha}\left\{ \bar{A}_{i4}^{\gamma\alpha}{}_{IJ} V_J^\alpha + A_{i4}^{\gamma\alpha}{}_{IJ}\frac{\partial W_J^\alpha}{\partial y} + \bar{A}_{i5}^{\gamma\alpha}{}_{IJ} U_J^\alpha + A_{i5}^{\gamma\alpha}{}_{IJ}\frac{\partial W_J^\alpha}{\partial x}\right\} \\
& + \sum_{J=1}^{N^\beta}\left\{ \bar{A}_{i4}^{\gamma\beta}{}_{IJ} V_J^\beta + A_{i4}^{\gamma\beta}{}_{IJ}\frac{\partial W_J^\beta}{\partial y} + \bar{A}_{i5}^{\gamma\beta}{}_{IJ} U_J^\beta + A_{i5}^{\gamma\beta}{}_{IJ}\frac{\partial W_J^\beta}{\partial x}\right\}
\end{aligned}
\tag{3.22b}
$$

$$
\begin{aligned}
\tilde{N}_{\underset{3}{I}}^{\gamma} = & \sum_{J=1}^{N^{\alpha}} \left\{ \bar{A}_{\underset{31}{JI}}^{\alpha\gamma} \frac{\partial U_J^{\alpha}}{\partial x} + \bar{A}_{\underset{32}{JI}}^{\alpha\gamma} \frac{\partial V_J^{\alpha}}{\partial y} + \bar{\bar{A}}_{\underset{33}{JI}}^{\alpha\gamma} W_J^{\alpha} + \bar{A}_{\underset{36}{JI}}^{\alpha\gamma} \left(\frac{\partial U_J^{\alpha}}{\partial y} + \frac{\partial V_J^{\alpha}}{\partial x} \right) \right\} \\
& + \sum_{J=1}^{N^{\beta}} \left\{ \bar{A}_{\underset{31}{JI}}^{\beta\gamma} \frac{\partial U_J^{\beta}}{\partial x} + \bar{A}_{\underset{32}{JI}}^{\beta\gamma} \frac{\partial V_J^{\beta}}{\partial y} + \bar{\bar{A}}_{\underset{33}{JI}}^{\beta\gamma} W_J^{\beta} + \bar{A}_{\underset{36}{JI}}^{\beta\gamma} \left(\frac{\partial U_J^{\beta}}{\partial y} + \frac{\partial V_J^{\beta}}{\partial x} \right) \right\} \\
& + \sum_{J,K=1}^{N^{\alpha}} \left\{ \frac{1}{2} \bar{B}_{\underset{31}{JKI}}^{\alpha\alpha\gamma} \frac{\partial W_J^{\alpha}}{\partial x} \frac{\partial W_K^{\alpha}}{\partial x} + \frac{1}{2} \bar{B}_{\underset{32}{JKI}}^{\alpha\alpha\gamma} \frac{\partial W_J^{\alpha}}{\partial y} \frac{\partial W_K^{\alpha}}{\partial y} + \bar{B}_{\underset{36}{JKI}}^{\alpha\alpha\gamma} \frac{\partial W_J^{\alpha}}{\partial x} \frac{\partial W_K^{\alpha}}{\partial y} \right\} \\
& + \sum_{J,K=1}^{N^{\beta}} \left\{ \frac{1}{2} \bar{B}_{\underset{31}{JKI}}^{\beta\beta\gamma} \frac{\partial W_J^{\beta}}{\partial x} \frac{\partial W_K^{\beta}}{\partial x} + \frac{1}{2} \bar{B}_{\underset{32}{JKI}}^{\beta\beta\gamma} \frac{\partial W_J^{\beta}}{\partial y} \frac{\partial W_K^{\beta}}{\partial y} + \bar{B}_{\underset{36}{JKI}}^{\beta\beta\gamma} \frac{\partial W_J^{\beta}}{\partial x} \frac{\partial W_K^{\beta}}{\partial y} \right\} \\
& + \sum_{J=1}^{N^{\alpha}} \sum_{K=1}^{N^{\beta}} \left\{ \bar{B}_{\underset{31}{JKI}}^{\alpha\beta\gamma} \frac{\partial W_J^{\alpha}}{\partial x} \frac{\partial W_K^{\beta}}{\partial x} + \bar{B}_{\underset{32}{JKI}}^{\alpha\beta\gamma} \frac{\partial W_J^{\alpha}}{\partial y} \frac{\partial W_K^{\beta}}{\partial y} \right. \\
& \qquad \left. + \bar{B}_{\underset{36}{JKI}}^{\alpha\beta\gamma} \left(\frac{\partial W_J^{\alpha}}{\partial x} \frac{\partial W_K^{\beta}}{\partial y} + \frac{\partial W_J^{\alpha}}{\partial y} \frac{\partial W_K^{\beta}}{\partial x} \right) \right\}
\end{aligned}
\tag{3.22c}
$$

$$
\begin{aligned}
\tilde{N}_{\underset{i=4,5}{I}}^{\gamma} = & \sum_{J=1}^{N^{\alpha}} \left\{ \bar{\bar{A}}_{\underset{i4}{JI}}^{\alpha\gamma} V_J^{\alpha} + \bar{A}_{\underset{i4}{JI}}^{\alpha\gamma} \frac{\partial W_J^{\alpha}}{\partial y} + \bar{\bar{A}}_{\underset{i5}{JI}}^{\alpha\gamma} U_J^{\alpha} + \bar{A}_{\underset{i5}{JI}}^{\alpha\gamma} \frac{\partial W_J^{\alpha}}{\partial x} \right\} \\
& + \sum_{J=1}^{N^{\beta}} \left\{ \bar{\bar{A}}_{\underset{i4}{JI}}^{\beta\gamma} V_J^{\beta} + \bar{A}_{\underset{i4}{JI}}^{\beta\gamma} \frac{\partial W_J^{\beta}}{\partial y} + \bar{\bar{A}}_{\underset{i5}{JI}}^{\beta\gamma} U_J^{\beta} + \bar{A}_{\underset{i5}{JI}}^{\beta\gamma} \frac{\partial W_J^{\beta}}{\partial x} \right\}
\end{aligned}
\tag{3.22d}
$$

$$
\begin{aligned}
M^{\gamma\delta}_{\substack{IJ \\ i=1,2,6}} = &\sum_{K=1}^{N^\alpha}\Bigg\{ B^{\gamma\delta\alpha}_{i1IJK}\frac{\partial U^\alpha_K}{\partial x} + B^{\gamma\delta\alpha}_{i2IJK}\frac{\partial V^\alpha_K}{\partial y} + \bar{B}^{\gamma\delta\alpha}_{i3IJK} W^\alpha_K \\
&\quad + B^{\gamma\delta\alpha}_{i6IJK}\left(\frac{\partial U^\alpha_K}{\partial y} + \frac{\partial V^\alpha_K}{\partial x}\right)\Bigg\} \\
&+ \sum_{K=1}^{N^\beta}\Bigg\{ B^{\gamma\delta\beta}_{i1IJK}\frac{\partial U^\beta_K}{\partial x} + B^{\gamma\delta\beta}_{i2IJK}\frac{\partial V^\beta_K}{\partial y} + \bar{B}^{\gamma\delta\beta}_{i3IJK} W^\beta_K \\
&\quad + B^{\gamma\delta\beta}_{i6IJK}\left(\frac{\partial U^\beta_K}{\partial y} + \frac{\partial V^\beta_K}{\partial x}\right)\Bigg\} \\
&+ \sum_{K,L=1}^{N^\alpha}\Bigg\{ \frac{1}{2} D^{\gamma\delta\alpha\alpha}_{i1IJKL}\frac{\partial W^\alpha_K}{\partial x}\frac{\partial W^\alpha_L}{\partial x} + \frac{1}{2} D^{\gamma\delta\alpha\alpha}_{i2IJKL}\frac{\partial W^\alpha_K}{\partial y}\frac{\partial W^\alpha_L}{\partial y} \\
&\quad + D^{\gamma\delta\alpha\alpha}_{i6IJKL}\frac{\partial W^\alpha_K}{\partial x}\frac{\partial W^\alpha_L}{\partial y}\Bigg\} \\
&+ \sum_{K,L=1}^{N^\beta}\Bigg\{ \frac{1}{2} D^{\gamma\delta\beta\beta}_{i1IJKL}\frac{\partial W^\beta_K}{\partial x}\frac{\partial W^\beta_L}{\partial x} + \frac{1}{2} D^{\gamma\delta\beta\beta}_{i2IJKL}\frac{\partial W^\beta_K}{\partial y}\frac{\partial W^\beta_L}{\partial y} \\
&\quad + D^{\gamma\delta\beta\beta}_{i6IJKL}\frac{\partial W^\beta_K}{\partial x}\frac{\partial W^\beta_L}{\partial y}\Bigg\} \\
&+ \sum_{K=1}^{N^\alpha}\sum_{L=1}^{N^\beta}\Bigg\{ D^{\gamma\delta\alpha\beta}_{i1IJKL}\frac{\partial W^\alpha_K}{\partial x}\frac{\partial W^\beta_L}{\partial x} + D^{\gamma\delta\alpha\beta}_{i2IJKL}\frac{\partial W^\alpha_K}{\partial y}\frac{\partial W^\beta_L}{\partial y} \\
&\quad + D^{\gamma\delta\alpha\beta}_{i6IJKL}\left(\frac{\partial W^\alpha_K}{\partial x}\frac{\partial W^\beta_L}{\partial y} + \frac{\partial W^\alpha_K}{\partial y}\frac{\partial W^\beta_L}{\partial x}\right)\Bigg\}
\end{aligned}
\tag{3.22e}
$$

3.4.5 Stiffness matrix, and extension to multiple fields

The full form of N, $\tilde{N}$ and M, (3.22), can be substituted into (3.19) to give the variational statement in terms of $A, \bar{A}, \bar{\bar{A}}, B, \bar{B}$ and D. From this form, the terms for the stiffness matrix can be derived, but will not be shown here. The stiffness matrix will take the form:

$$
\boldsymbol{K} = \left[\begin{array}{ccc|ccc}
K^{\alpha\alpha}_{11} & K^{\alpha\alpha}_{12} & K^{\alpha\alpha}_{13} & K^{\alpha\beta}_{11} & K^{\alpha\beta}_{12} & K^{\alpha\beta}_{13} \\
K^{\alpha\alpha}_{21} & K^{\alpha\alpha}_{22} & K^{\alpha\alpha}_{23} & K^{\alpha\beta}_{21} & K^{\alpha\beta}_{22} & K^{\alpha\beta}_{23} \\
K^{\alpha\alpha}_{31} & K^{\alpha\alpha}_{32} & K^{\alpha\alpha}_{33} & K^{\alpha\beta}_{31} & K^{\alpha\beta}_{32} & K^{\alpha\beta}_{33} \\
\hline
K^{\beta\alpha}_{11} & K^{\beta\alpha}_{12} & K^{\beta\alpha}_{13} & K^{\beta\beta}_{11} & K^{\beta\beta}_{12} & K^{\beta\beta}_{13} \\
K^{\beta\alpha}_{21} & K^{\beta\alpha}_{22} & K^{\beta\alpha}_{23} & K^{\beta\beta}_{21} & K^{\beta\beta}_{22} & K^{\beta\beta}_{23} \\
K^{\beta\alpha}_{31} & K^{\beta\alpha}_{32} & K^{\beta\alpha}_{33} & K^{\beta\beta}_{31} & K^{\beta\beta}_{32} & K^{\beta\beta}_{33}
\end{array}\right]
\tag{3.23}
$$

It is clear that the definition of the $K^{\alpha\alpha}_{ij}$ and $K^{\beta\beta}_{ij}$ terms will be identical, with the displacement field α swapped for β, and likewise for $K^{\alpha\beta}_{ij}$ and $K^{\beta\alpha}_{ij}$. From the

variational statement,

$$K_{ij}^{\gamma\delta} = f\left(\overset{\iota\mu}{A}_{ij}^{IJ}, \overset{\iota\mu}{\bar{A}}_{ij}^{IJ}, \overset{\iota\mu}{\bar{\bar{A}}}_{ij}^{IJ}, \overset{\iota\mu\kappa}{B}_{ij}^{IJK}, \overset{\iota\mu\kappa}{\bar{B}}_{ij}^{IJK}, \overset{\iota\mu\kappa\lambda}{D}_{ij}^{IJKL}\right) \tag{3.24}$$

The terms in $K_{ij}^{\gamma\delta}$ where $\iota = \mu = \kappa = \lambda (= \alpha \text{ or } \beta)$, are functions of the degrees-of-freedom of one displacement field only. These terms only occur in K terms where $\gamma = \delta$ (i.e. $K_{ij}^{\alpha\alpha}$ and $K_{ij}^{\beta\beta}$). Where $\iota, \mu, \kappa, \lambda$ are not all equal, the term is a coupling term—it represents the interaction between the degrees of freedom between displacement fields α and β. We can separate the K terms into their components:

$$K_{ij}^{\gamma\delta} = \sum_c K_{ij}^{\gamma\delta} \tag{3.25}$$

where K_c are the 'coupling terms', including the self-coupling terms of one displacement field only as described above. Thus, extending the concept to a total number of N displacement fields, the stiffness matrix is given by:

$$\boldsymbol{K} = \begin{bmatrix} \left[\sum_{\alpha=1}^{N} K_{ij}^{1\alpha}\right] & \left[K_{ij}^{12}\right] & \cdots & \left[K_{ij}^{1N}\right] \\ \left[K_{ij}^{21}\right] & \left[\sum_{\alpha=1}^{N} K_{ij}^{2\alpha}\right] & \cdots & \left[K_{ij}^{2N}\right] \\ \vdots & \vdots & \ddots & \vdots \\ \left[K_{ij}^{N\alpha}\right] & \left[K_{ij}^{N2}\right] & \cdots & \left[\sum_{\alpha=1}^{N} K_{ij}^{N\alpha}\right] \end{bmatrix} \tag{3.26}$$

3.4.6 Solution by heirarchical application

The superposition of two displacement fields will result in a number of variables that are redundant. To determine a unique solution, a number of the variables must be eliminated. This requires the definition of a hierarchy of models, and the imposition of boundary conditions. The lowest level of the hierarchy, α, is the least capable theory, e.g. an ESL model, and is applied to the entire problem domain. Each level up in the hierarchy should be capable of representing the displacement field of the lower order theory, and is applied to a subset of the domain of the parent model (3.27). Thus, variables are eliminated from the problem by imposition of a zero-displacement boundary condition on the boundary of the domain of the more refined theory (3.28).

$$\Omega_\alpha = \Omega \qquad\qquad \Omega_\alpha \supseteq \Omega_\beta \supseteq \cdots \supseteq \Omega_N \tag{3.27}$$

$$\boldsymbol{u}^\beta(\Gamma_\beta) = 0; \quad \cdots \quad \boldsymbol{u}^N(\Gamma_N) = 0 \tag{3.28}$$

3.5 Summary of method

The method represents the displacement field within the composite plate as the summation of a number of independent displacement fields. Each displacement field can be of different order (linear, quadratic etc.), and an appropriate combination of displacement functions can be selected to achieve the desired level of detail in the output results. Enrichment is conducted by adding additional degrees-of-freedom to a layerwise model, enabling localized enrichment in the in-plane discretization aligned with the existing mesh, and an arbitrary enrichment in the through-thickness discretization.

3.6 Results

3.6.1 Reproducing analytical results using classical layerwise models

The code developed to date has been tested against a number of references given in the literature. In this section, results are presented from one model with details taken from [72, Section 3.7, *An example with layerwise elements*, pp89–93].

The model is illustrated in Figure 3.8, and is a simply supported square plate of side length a, composed of three unidirectional lamina in (0/90/0) configuration. The plate is thick with $a/h = 4$. The applied load used in the following example is bi-sinusoidal with peak q_0, i.e. $p(x,y) = q_0(sin(x\pi/a).sin(y\pi/a))$. Material properties are:

$$\frac{E_1}{E_2} = 25 \qquad E_3 = E_2 \qquad \frac{G_{12}}{G_{23}} = 2.5 \qquad G_{13} = G_{12} \qquad \nu_{12} = \nu_{12} = \nu_{12} = 0.25$$

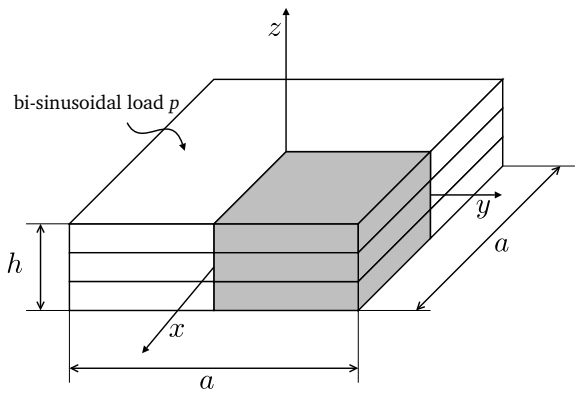

Figure 3.8: **Illustration of loaded plate** with modelled quarter highlighted

The results are also compared here to the exact 3D elasticity solution as presented

Model	in-plane discretization	through-thickness discretization
FSDT	4×4 elements, 8-node quadratic	Linear
1Q	4×4 elements, 8-node quadratic	1 quadratic per lamina
2Q	4×4 elements, 8-node quadratic	2 quadratic per lamina
1C	4×4 elements, 8-node quadratic	1 cubic per lamina

Table 3.1: Layerwise models

in [72]. In Figure 3.10 the nondimensionalized stresses are plotted, given by:

$$\bar{\sigma}_{xx} = \frac{h^2}{q_0 a^2} \qquad \bar{\sigma}_{zz} = \frac{1}{q_0}$$
$$\bar{\sigma}_{yz} = \frac{h}{q_0 a} \qquad \bar{\sigma}_{zx} = \frac{h}{q_0 a} \tag{3.29}$$

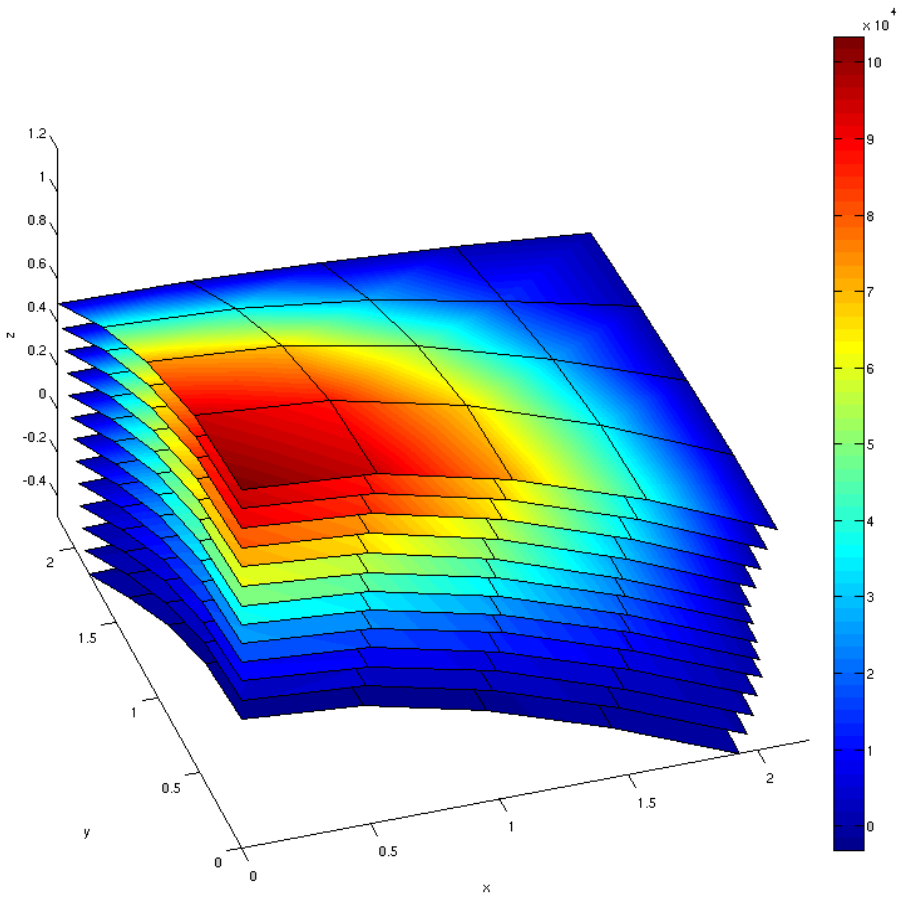

Figure 3.9: **Deflected shape plot of plate model** Quarter model (by symmetry), contours show transverse stress σ_{zz}. Model 2Q interfaces.

From the results plotted here, it is evident that the FSDT method is not capable of accurately resolving the stresses. This inaccuracy is further exaggerated at the interfaces, where accurate stresses are essential to model failure mechanisms such

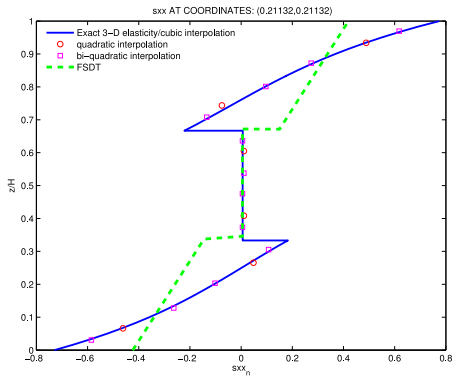

(a) In-plane stress $\bar{\sigma}_{xx}$

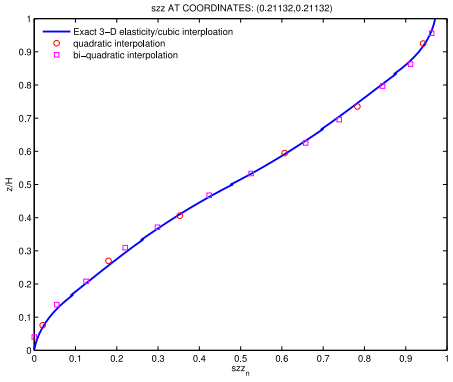

(b) Transverse direct stress $\bar{\sigma}_{zz}$. Note, the FSDT is not capable of resolving through-thickness direct stresses—see (3.2)

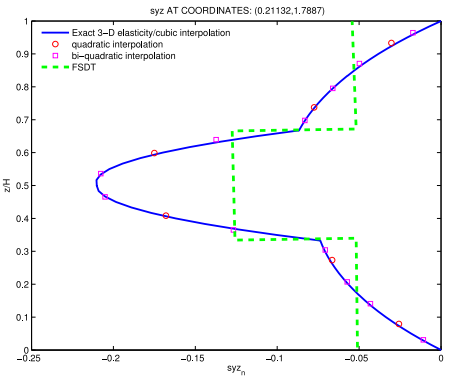

(c) Transverse shear stress $\bar{\sigma}_{yz}$

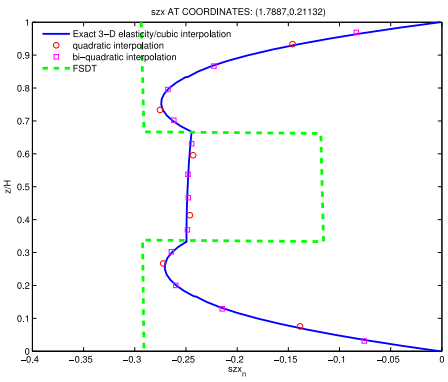

(d) Transverse shear stress $\bar{\sigma}_{zx}$

Figure 3.10: **Stresses plotted through plate thickness**

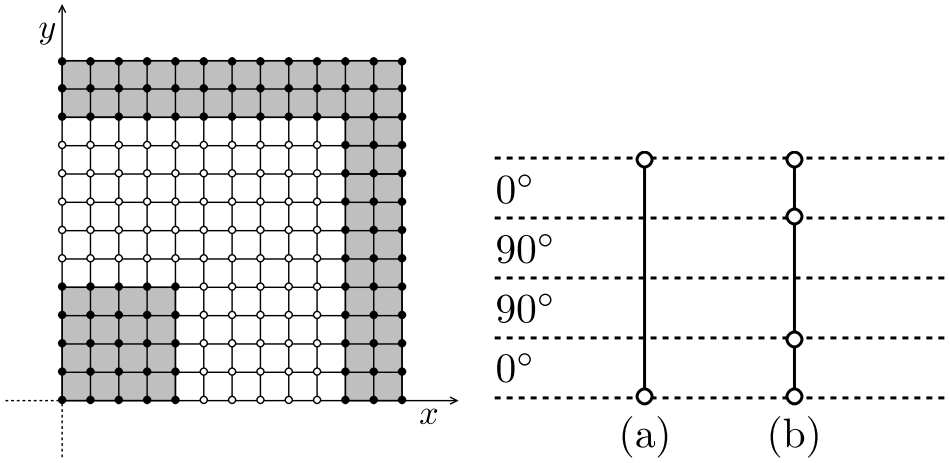

(a) 2D in-plane mesh, 1/4 model—showing enriched regions and nodes (∘: ordinary; •: enriched)

(b) 1D transverse mesh—(a) global mesh: ESL, linear; (b) local enrichment: piecewise, cubic.

Figure 3.11: **Locally enriched plate model**

as delamination. The cubic model, 1C, produces results that are indistinguishable from the exact 3D solution, through the entire thickness. At lesser through-thickness discretizations 1Q and 2Q, the results show a superior accuracy to the FSDT at the integration points (plotted). At other points through the thickness, the accuracy is reduced, but the stresses at the interfaces remain close to the exact solution. This suggests that a cubic displacement variation in the z-direction is not essential to model interlaminar failure (delamination). Similar results are obtained from other analyses that have been run.

3.6.2 Reproducing accurate interlaminar strains with reduced model size

The capability of the method is demonstrated by conducting a similar modelling exercise, using the ability to conduct enrichment in only a localized region of the model. In this model, a simply supported plate of dimensions $a/h = 10$ applied with a bi-sinusoidal load is modelled using an ESL model (Figure 3.11). It is expected that the critical regions (regions of high stress or regions likely to initiate failure) will be either at the centre or the edges of the plate. Consequently, the elements in these regions are enriched by adding extra transversely dependent degrees of freedom to their associated nodes.

This model is compared to similar geometry and loading conditions modelled using an ESL model, and by using a globally defined high order displacement field. The model size is listed in Table 3.2.

The results of the locally enriched model are shown in Figure 3.12, and comparisons of the through-thickness stresses in key locations are plotted in Figure 3.13. It can

model	degrees-of-freedom
equivalent single layer	**5772**
locally enriched model	**8790**
globally high order piecewise	**18759**

Table 3.2: Degrees of freedom, representing computational cost of different models

be seen that while the ESL model is unable to adequately represent the stresses in the selected locations, the locally enriched model is able to represent the values to within 10% of the globally high-order model. This is achieved using a model with approximately 1/2 the degrees of freedom of a globally high-order model (Table 3.2), representing a significant saving in computational cost. Typically for solving a system of equations, the number of computational operations and the memory requirements scale with the square of the problem size, so the example presented here represents a computational cost of only 25% of the more expensive model.

The degree of difference between the results from a locally enriched model and a globally high-order model (i.e. the accuracy) is a function of the proximity of the location to the transition between the ESL region and the local enrichment. In a practical application, a local 'mesh refinement' exercise can be conducted by sequentially expanding the enrichment zone to achieve convergence of the stresses at the point of interest. On a large component, the computational savings will be even higher.

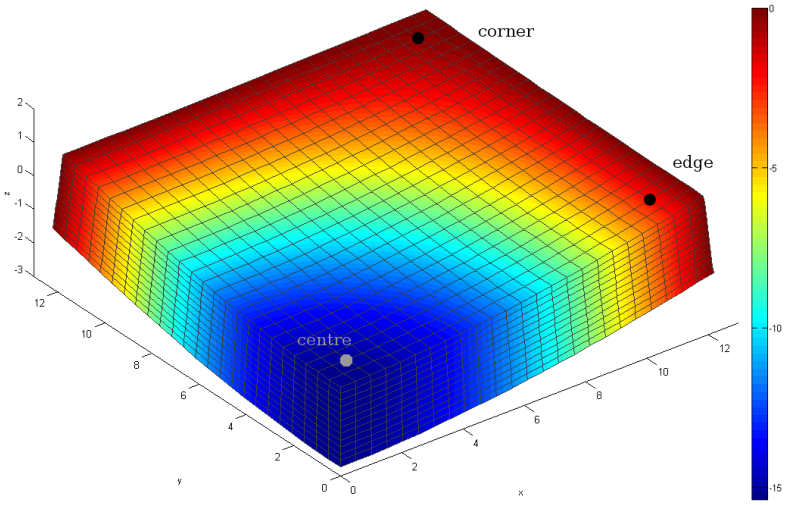

Figure 3.12: **Deflected shape plot of locally enriched plate model** Quarter model (by symmetry), contours show transverse displacement w

Further examples of the two-scale layerwise method are given in Appendix A.

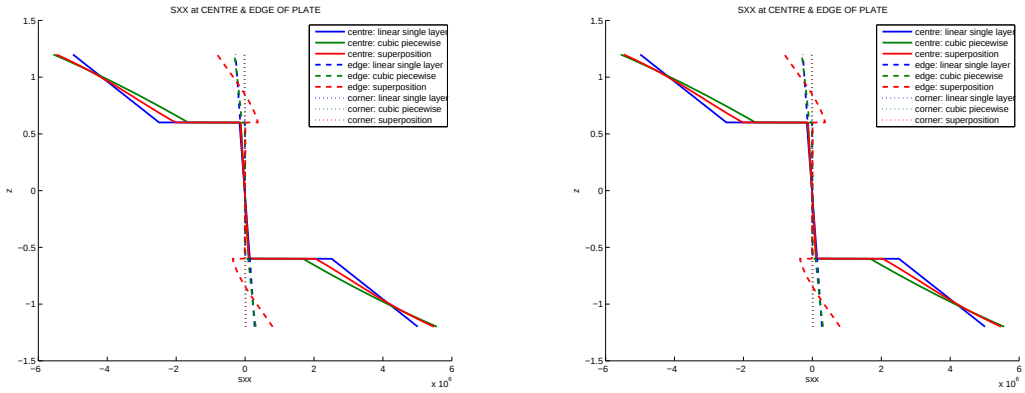

(a) Direct stress σ_{xx}

(b) Transverse shear σ_{yz}

Figure 3.13: **Transverse plots of the stress at the centre, edge and corner of the plate** . Locations refer to those given in Figure 3.12.

3.7 Discussion

The model presented here has demonstrated equivalence with full 3D models and with layerwise models when used with an equivalent number of degrees-of-freedom. In this case, the model will have the same computational cost, and the only advantage to using the present model is reduction of the meshing problem to that of a 2D surface.

The literature has already demonstrated the value of equivalent single layer models in reducing the computational cost of meshing and modelling, and has demonstrated that for certain problem types, the information generated is acceptable. In cases where only the overall displacement is required, an ESL model can be sufficient. For the purpose of this work, where damage tolerance of 3D weaved composites is required, the shortcomings of the ESL approach are apparent in its inability to accurately predict internal and interface stresses.

In section 3.6.2, the model was arbitrarily enriched in the zones where engineering judgement would predict the stresses to be particularly high and of interest to failure modelling. This approach can be used on many typical real-world components, since the approximate failure location can usually be predicted by a number of techniques. In further iterations of this work, it can be imagined that the decision to enrich a certain zone can be made *in-situ*, essentially using the presented model for a coarse displacement analysis and a detailed failure analysis without intervention from an analyst, including the requsite mesh convergence activities.

As presented here, the model is not specific to 3D weaved composites – it is applicable to any composite that can be described in a layered form.

3.8 Conclusions

The presented model has demonstrated the ability to simulate a layered composite with an acceptable level of accuracy at a smaller computational expense than full 3D and full layerwise models. In addition to the reduced cost, the ability to dynamically refine solutions in selected regions of the model enable detailed solutions to be obtained with a minimal extra cost. This has great value in predicting damage initiation and propagation on a typical component application, where damage tends to be highly localized, e.g. at a cantilever root, or at an impact site, whereas the remainder of the component can be at a very low stress.

The model presented here provides a capable and efficient foundation on which to build a unified multi-scale simulation incorporating damage, with applicability to 3D woven composites. Chapter 4 develops an interlaminar damage model that can be used at the larger length scale in the model here, and can be incorporated directly as an additional displacement function. Chapter 5 develops a model that can examine at an even smaller scale than the lamina scale used here, and can transfer information bi-directionally to both take ply scale stresses generated by this model to determine damage within the plies, and to feed back to this model the effective material properties in the presence of damage.

Chapter 4

Discrete interlaminar damage in the layerwise model

4.1 Introduction

Delamination is a key failure mechanism in laminated composites. One of the aims of 3D weaving is to mitigate against this mechanism by introducing through-thickness reinforcing fibres. The resistance to delamination and effective failure strength is increased, but the failure mechanism becomes quite complex to simulate, including fibre/matrix debonding and fibre pullout.

This section details the development of a method to explicitly incorporate the type of cracking that can occur in 3D-weaved composite materials. The method is incorporated in the multiscale method developed in Chapter 4.

4.2 Literature review on explicit damage modelling

As an alternative to a homogenized representation of the effect of damage in continuum damage modelling (CDM), damage in the form of cracking can be explicitly incorporated in the model by modifications to the model geometry or mesh. This is an approach typically used where the damage is easy to define in terms of dimension, shape and location, such as large, macro-scale cracking. The most obvious case in laminar composites is that of interlaminar failure, or delamination.

A number of authors have conducted reviews and presented ideas for incorporating delamination in computational models. de Borst and Remmers [90] conduct a brief review, and note that delamination is a discrete phenomenon best modelled at the mesoscopic level. Tay [91] conducts a review of investigations into the delamination process, and the considerations necessary in modelling it. The author focusses most of his review on considering fracture mechanics approaches—these approaches are typically based on fracture surface energy and strain energy release rates, and are

derived from similar approaches taken in modelling of isotropic media. The second part of the review comes to the approach that is also favoured by [90], that of interface and cohesive models.

Cohesive models usually use a special element at the delamination site, termed the 'cohesive', 'delamination' or 'interface'-element. The response of the element is described by a traction separation law that describes the tractions ($\boldsymbol{t}_d$) as a function of the delamination separation ($\boldsymbol{u}_d$).

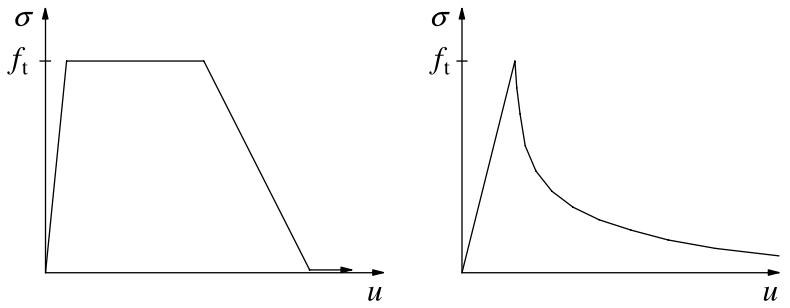

Figure 4.1: **Displacement-traction relationships for cohesive laws** the response is linear to tensile strength f_t, after which increased separation u reduces traction in a ductile (left) or quasi-brittle (right) manner [90]

The constitutive equation for the delamination is developed using the fracture mechanics approach of using the fracture energy or work of separation, G_c:

$$G_c = \int_{u=0}^{\infty} \sigma \, \mathrm{d}u \tag{4.1}$$

where σ is one of the components of the traction across the delamination dependent on which of the mode I, II or III value of G_c is being calculated, and u is the separation. The process is represented in Figure 4.1, and G_c is the area under the graphs. A simpler model is one where linear softening is assumed for the post-crack response, to give a bilinear cohesive law. Additional considerations are made for changes to the cohesive law on unloading. A good review of finite element interface models for delamination is given in Alfano and Crisfield [92]. A more generic overview of the derivation of decohesion laws is given in Scheider [93], where the author derives laws for ductile fracture of metals, a process of void nucleation, growth and coalescence.

As described above, the cohesive law is applied to a 'cohesive element' that sits between ordinary finite elements. However, there are a number of other methods which have been used to implement the models.

Barbero [54] builds on a 'generalized laminated plate theory' (GLPT), a form of layerwise theory, by incorporating delamination between lamina. This is achieved using an extended finite element (XFEM) approach to add a number of degrees of

freedom to the element to represent the discontinuous displacement field across a delamination. The extra degrees of freedom control the parameters of a Heaviside step function added to the ordinary shape functions. Later, in Barbero and Reddy [55] the concept is extended to allow for multiple delaminations within the laminate. Kim et al. [94] implement a nearly identical model in a variant of the layerwise theory using two extra degrees of freedom for each lamina to scale hyperbolic sin and cos functions, representing the 'zig-zag' nature of the displacement field.

Remmers et al. [95] use a similar approach to [55], working at the element level in 3D FE analysis, to allow for delamination within the element. This makes use of the 'partition-of-unity' property of finite element shape functions, and is named by the authors as a 'solid-like shell element' (Figure 4.2). This is later extended in Remmers et al. [39] to a 'cohesive segment', allowing for an arbitrary segment in any element to represent a discontinuity described by a cohesive law. Definition of the behaviour at coalescence allows multiple cohesive segments represent the macro-scale fracture process (Figure 4.3). This work is itself a continuation of the ideas presented in Wells and Sluys [96], Wells et al. [97], where a method was sought to allow an arbitrary discontinuity (a crack, and later a delamination) to be placed in a FE model in such a way that the subsequent behaviour was independent of the meshing. The ideas from all these papers are collected and form the core for a generalized approach to explicit modelling of discontinuities in Remmers [98]. The cohesive segments method does exhibit mesh independence, and this topic is explored in the review by de Borst et al. [99]. This property makes the process particularly suitable for modelling the entire process of crack nucleation, growth and coalescence, including dynamic propagation [100]. Cohesive segments have also been demonstrated within a 'meshless' framework by [101]. The advantages of this approach over the traditional finite element method (using interface elements) are noted, however the advantage over the more recent XFEM methods are not made clear by the authors.

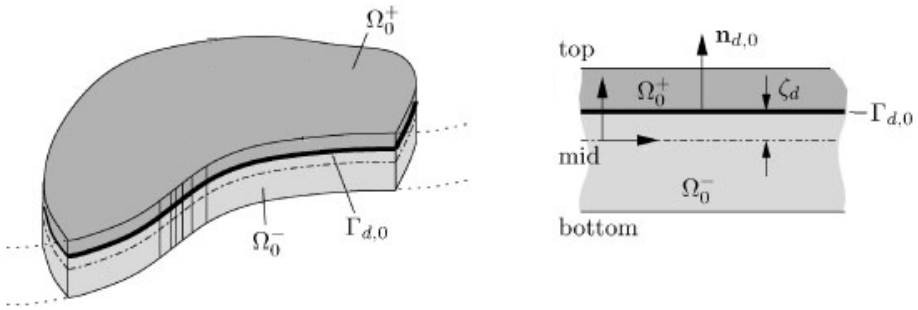

Figure 4.2: **Displacement field for the 'solid-like shell'-element** The shell is separated by the delamination, $\Gamma_{d,0}$, at a distance ζ_d from the centreline. This separates the domain Ω_0 into that below the delamination, Ω_0^-, and that over, Ω_0^+ [95]

Williams and Addessio [102, 103] develop a similar laminated plate model to [54, 55]. The model is developed in a sufficiently general way such that any layer and

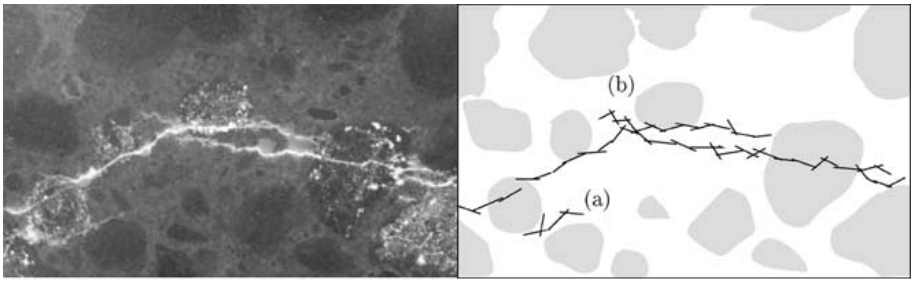

Figure 4.3: **Multiple cohesive segments used to model complex crack path** photo image of real crack (left) and model representation (right) [39]

delamination constitutive behaviour can be incorporated. In a later paper [104], it is recognised that the discontinuous field, or any arbitrary field, can be incorporated in selective regions of the model, and the author terms it a 'multilength scale' plate theory. Here, and in [105–107], the plate theories are taking on characteristics of multiscale analysis and mesh superposition that were examined in Chapter 3.

Camanho and Dávila [108] also develop a zero-thickness decohesion element, designed to be used in a solid element model. The focus of their work is to derive a decohesion law applicable to mixed mode loading. The criteria used to initiate the softening process is given as:

$$\left(\frac{t_{d3}}{N}\right)^2 + \left(\frac{t_{d1}}{S}\right)^2 + \left(\frac{t_{d2}}{T}\right)^2 = 1 \tag{4.2}$$

where t_d is the traction across the delamination and $1,2,3$ subscripts refer to the orthogonal directions, N is the interlaminar tensile strength (direction 3), and S and T are the interlaminar shear strengths (directions 1 and 2). Propagation can be controlled by a number of models, the simplest of which is the 'power law criterion':

$$\left(\frac{G_I}{G_{Ic}}\right)^\alpha + \left(\frac{G_{II}}{G_{IIc}}\right)^\alpha + \left(\frac{G_{III}}{G_{IIIc}}\right)^\alpha = 1 \tag{4.3}$$

where G is the fracture energy (calculated from (4.1) with upper limit u_d, the displacement discontinuity), I, II, III subscripts refer to the fracture mode, and c subscript refers to the critical value (4.1). Later work by Dávila et al. [109, 110] moves this development to shell elements, in line with much of the other research in the field. The use of mixed-mode growth criteria is combined with the solid-like shell element of [95] in Cid Alfaro et al. [111], and demonstrates accurate simulation of the complex fracture process in GLARE (glass reinforced fibre-metal laminate, a laminate composed of alternating aluminium and fibre-epoxy composite lamina).

Implementing decohesion using shell elements is also the preferred approach of Liu and Yu [112]. The authors develop their method by modelling the laminate as a stack of shell elements. The 2D elements are applied an 'offset' from the laminate centreline to represent their position, and delamination can be implemented by using incompatible offsets in the different lamina. Different models are used for the shear

slip modes and opening modes. The opening modes are modelled using 'flexible connectors' account for the traction across the opening.

A recent paper by Aymerich et al. [113] chooses to use separate cohesive elements in a solid element model when investigating the use of cohesive laws in modelling impact induced delaminations in unidirectional composites. The authors do not make it clear why this choice was made over the more typical enhanced plate or shell models, however the work demonstrates a good prediction of the impact response.

Sun et al. [44] take a slightly different approach to modelling the discontinuity in the enriched element failure method, REFM. The REFM is an extended FEM approach, similar to the models above that add the discontinuity to existing elements rather than introducing new interface elements, such as those introduced by Remmers et al. [95]. The difference is that instead of adjusting the material stiffness matrix or engineering constants, an extra compensatory force is added to the element nodes (Figure 4.4). The ability to maintain the stiffness matrix without reformulation is a great advantage for speed and efficiency. The paper only considers the case of a zero traction crack, however it would be possible to enhance this approach to use a cohesive model to represent the traction-displacement relationship. The modelling capability of such an approach would be similar to the methods presented above, but may be more computationally efficient.

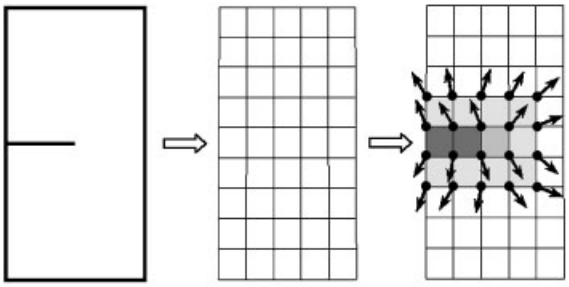

Figure 4.4: **The REFM** The geometry with a discontinuity (left) is modelled using an ordinary FE mesh, independent of the crack (centre). On loading, the effect of the crack is incorporated by applying an additional force to the nodes surrounding it [44]

From the review above, it is clear that there are a number of different approaches to using a cohesive model. Elices et al. [114] present a review of the use of the cohesive model to determine behaviour at the crack tip. The focus of the review is less on the implementation of the law, and more on the softening model that forms the core of the method. A wider review, with more focus on composite materials is given by Yang and Cox [115]. The review notes a general change in strategy in the literature from considering the behaviour at the crack tip as a point process, as in linear elastic fracture mechanics (LEFM) to cohesive zones. This change requires volume integration of the zone over which the traction applies, and avoids problems of traction discontinuities at mesh edges. In summary, the review concludes that the cohesive model is a good

compromise between computational efficiency (when compared to LEFM) and physical reality.

4.3 Aims

The aim of the method developed here is to produce a model capable of simulating the separation of regions in a 3D-weaved composite. This incorporates cracking in the continuous phase, transfer of load to the reinforcement or binder tows, and pullout or fracture of fibres that can bridge across the crack. When incorporated in the multi-scale model developed in Chapter 3, this method will provide a technique to explicitly simulate delamination.

4.4 Method

The delamination in the 3D weaved composite is modelled using a modified piecewise consitutive law to account for the progressive failure. The model is based upon simple bilinear constitutive models (see section 4.2) widely implemented in literature, in the absence of more detail data on the nature of the failure.

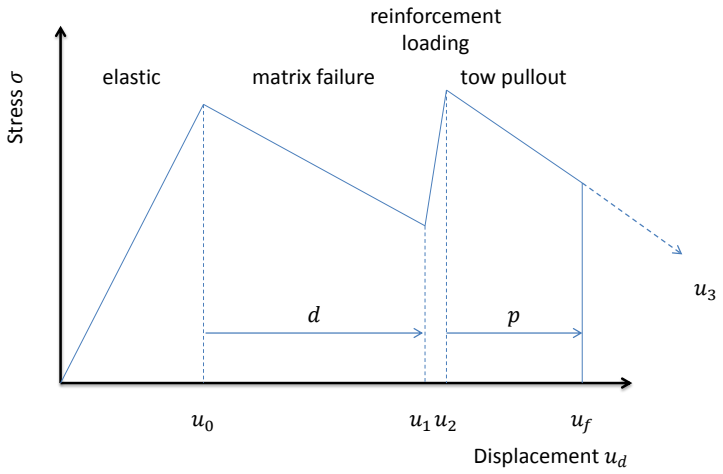

Figure 4.5: **Piecewise linear cohesive law for separation of through-thickness reinforced laminates**

The model relates the traction that acts across a delaminating surface to the relative displacement $\mathbf{u}_D$ of the two sides of the interface. The relative separation results in an effective strain across the interface, denoted ε here.

The behaviour of the model can be described by five phases or regions:

$u_D \leq u_0$ the delamination exhibits linear elasticity, i.e. it is described by the undamaged composite stiffness K. This response also holds for the case $u_D < 0$.

$u_0 < u_D \leq u_1$ The matrix damage softening phase. Once the critical value of $u_D = u_0$ has been reached, the matrix begins to fail and the interface begins to soften. At the end of this phase, the matrix is no longer carrying any load: instead, the load is carried entirely by the through-thickness binder tows. If the stiffness of the system when the load is carried by just the binder tows is given by K_r, the instantaneous stiffness K' is given by:

$$K' = K + (K_r - K)d, \qquad \text{where} \qquad d = \frac{u_D - u_0}{u_1 - u_0} \tag{4.4}$$

The parameter d is a delamination history progression indicator, and does not decrease at any point during any load history.

$u_1 < u_D \leq u_2$ is the phase where the load is carried by the binder tows. This is a linear elastic phase, characterized by the stiffness of the tows. Here, the instantaneous stiffness is given by the stiffness of the binder tows multiplied by their areal density:

$$K' = K_r A_r, \qquad \text{where} \qquad A_r = \frac{a_r}{a} \tag{4.5}$$

a_r is the in-plane cross sectional area of all the binder tows in a plane section of area a. The end of this phase is characterized by the onset of tow pullout, which is typically described by a critical load.

$u_2 < u_D \leq u_f$ is the tow pullout phase. This behaves in a very similar manner to the matrix degradation phase. The instantaneous stiffness is given by:

$$K' = K_r(1 - p), \qquad \text{where} \qquad p = \frac{u_D - u_2}{u_3 - u_2} \tag{4.6}$$

where u_3 is a hypothetical zero traction pullout displacement. Typically, the tow will reach complete pullout or tow fracture before this value, and so a critical failure displacement is specified.

$u_D > u_f$ complete separation, i.e. the delamination is unable to sustain any traction across its surface.

During each phase, unloading follows the same instantaneous stiffness response K'.

Application of a compressive strain across the interface remains linearly elastic, with a stiffness equal to the initial undamaged stiffness K, irrespective of the history of

the delamination. This ensures that in a numerical implementation, interpenetration of the delamination surfaces does not occcur.

The model requires the specification of the points u_0, u_1, u_2, u_3 and u_f to be fully defined.

The initiation of damage u_0 is described using a combined failure criterion:

$$\left(\frac{\sigma_{zz}}{\sigma_f}\right)^2 + \left(\frac{\tau_{xz}}{\tau_f}\right)^2 + \left(\frac{\tau_{yz}}{\tau_f}\right)^2 = 1 \tag{4.7}$$

where z is the laminate through-thickness direction, and x and y are the in plane directions. The critical failure values σ_f and τ_f correspond to the mode I and mode II failure strengths respectively. In a laminate where the delamination fracture occurs wholly within the matrix, these will be the matrix failure criteria. Where the composite has through thickess reinforcements, the values for σ_f and τ_f can be derived from experimental data.

The matrix decohesion condition u_2 is described using the energy of fracture. The area under the curve Figure 4.5 represents the fracture energy. The value of ε_f is chosen to equate the fracture energy to the critical fracture energy G_c for the case where no binder tows are present. The value of G_c is different for the mode I and mode II fracture (G_{Ic} and G_{IIc} respectively) thus in this model, mode I and mode II fracture behave independently after the initiation of the softening. The parameters u_2 and u_f can be determined experimentally, and u_3 by extrapolation of the experimental data. In this model, an energy criteria is not used, since this requires knowledge of the length of binder tow that debonds from the surrounding matrix before it is pulled out. These values could be determined by explicitly incorporating the binder tows in the finite element model, but this would greatly increase the computational cost, so an empirical approach is chosen here.

4.4.1 Incorporation into the two-scale layerwise model

The multi-scale layerwise model developed in Chapter 3 is designed to allow for multiple superimposed displacement fields in any given element. This allows for trivial addition of a displacement field to define a discrete discontinuity in the through-thickess (z) direction.

Six additional degrees-of-freedom, and one state variable are assigned to each node in the in-plane mesh. The state variable, z_D, defines the z-coordinate of the discontinuity in the displacement. The extra degrees-of-freedom, $\mathbf{u}_{Dl}$ and $\mathbf{u}_{Du}$ define the opening displacement of the discontinuity, in each of the x-, y- and z-directions at the upper and lower surfaces respectively. The displacement of the two sides of the delamination are interpolated using a set of discontinuous shape functions:

$$\mathbf{u}_D = \mathbf{N}_D \begin{Bmatrix} \mathbf{u}_{Dl} \\ \mathbf{u}_{Du} \end{Bmatrix} \tag{4.8}$$

where

$$\mathbf{N}_D = \begin{bmatrix} N_D & N_D & N_D \end{bmatrix} \tag{4.9}$$

$$N_D = \begin{cases} \begin{bmatrix} 0 & -\frac{1}{2}(1+\xi) \end{bmatrix} & : \xi \leq \xi_D \\ \begin{bmatrix} \frac{1}{2}(1-\xi) & 0 \end{bmatrix} & : \xi > \xi_D \end{cases} \tag{4.10}$$

and ξ is the natural coordinate ($-1 \leq \xi \leq 1$) running between the lower and upper surface of the composite plate, and ξ_D is the natural coordinate cooresponding to z_D. The shape functions are repeated as the interpolation for the x-, y- and z-discontinuities are identical.

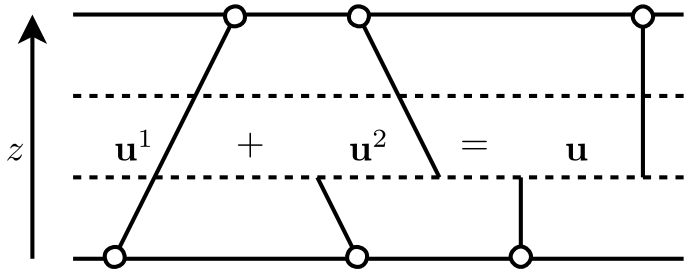

Figure 4.6: **Illustration of discontinuous shape function** u_1 is a continuous displacement using the method described in Chapter 3, i.e. it can be composed of multiple different displacement fields (shape functions). u_2 is the discontinuous shape function described here, and the summation of this field onto the existing displacement shows how the discontinuity is introduced into the model.

The relative displacement between the two sides of the delamination are given by:

$$\mathbf{d} = \mathbf{u}_{Du} - \mathbf{u}_{Dl} \tag{4.11}$$

It is a requirement of the macro/meso-scale layerwise model that sufficient boundary conditions are applied to each displacment field definition to allow a unique solution to de determined. In this model, the discrete delamination field is always applied in addition to a continuous displacement field definition (possibly the summation of a number of other conventional polynomial displacement fields). The model is constrained by applying a boundary condition of $\mathbf{u}_{Dl} = 0$.

On incorporation into the macro/meso-scale layerwise model, the discontinuous displacement field is treated like any other displacement field definition, and multiple delaminations at different through-thickness planes can be applied to any point in the xy-plane of the the composite plate.

4.5 Summary of method

A piecewise cohesive law describing the traction separation relationship between the two sides of a delamination has been implemented. The law incorporates elastic, matrix-degradation, fibre-loaded, fibre-pullout and fibre-fractured modes. The cohesive model is applied to the layerwise model developed in Chapter 4 by the addition of three degrees of freedom (after necessary boundary conditions have been applied) and one state variable to every in-plane node at which delamination is modelled. The incorporation into this model allows for any number of delaminations to be modelled at any point in plane, and any point through the thickess of a composite plate, including overlapping or partially overlapping delaminations.

4.6 Results

In this section, the model and the code implementing the model are demonstrated. To validate the model, it is compared to results in papers by Meo and Thieulot [116] for plain delamination. This source in literature is for a laminate composites without through-thickness reinforcement, thus the part of the model simulating the pullout and fracture of through-thickness binder tows is not tested.

The model is then demonstrated solving for a test case in which through-thickness reinforcement is present. To the author's knowledge, there are no publications with data in the appropriate form to perform a comparative analysis.

4.6.1 Comparison to literature

Meo and Thieulot [116] conducted a review of a number of methods to simulate delamination in a double cantilever beam. Data is provided for the results of experimental testing that the present model will attempt to reproduce. In [116] two models demonstrated are similar to the present model: the cohesive zone model, and the non-linear spring model. Both the models are described by a bilinear traction separation relationship. The same relationship will be applied to the present model, and the additional variables relating to fibre pullout and fracture are set to null values.

The model is of a double cantilever beam. The dimensions of the beam used in the experimental work are 0.185m long, 0.025m wide, and two 0.0025m plies thick, between which the delamination will propagate. Both sides of the delamination are composed of 12-off 0 ° plies. An initial crack of length 55mm is used.

The model of the beam is constructed by an in-plane mesh of 20×4 elements. The through-thickness dimension is modelled with a 4-part linear piecewise function. It should be noted that the XFEM approach used in this model is capable of using a single element, however the interface stresses will be less accurate. A single element

parameter	value
E_{xx}	135 GPa
E_{yy}, E_{zz}	9 GPa
G_{xy}, G_{xz}	5.2 GPa
G_{yz}	1.9 GPa
ν_{xy}	0.34
ν_{xz}	0.34
ν_{yz}	0.46

Table 4.1: Elastic properties for double cantilever beam [116]

parameter	value
Interface element stiffness	5500 GPa
Separation at initiation of damage u_0	7×10^{-6}m
Traction free separation u_1	24×10^{-6}m

Table 4.2: Cohesive element separation properties [116]

thickness discontinuous displacement element is applied across the entire plane of the model to simulate the delamination. The delamination is specified with complete degradation ($d = 1$) for a length of 6 elements from the free end, and pristine material ($d = 0$) for the remainder.

The material properties are described in Table 4.1, where x is the fibre direction, along the length of the cantilever beam, and z is the through-thickness direction.

The separation properties applied to the model developed here are given in Table 4.2.

Figure 4.7 illustrates the bending stresses (i.e. the stresses along the direction of the beam σ_{xx}) in the double cantilever beam model. Figure 4.8 shows a comparison of the results obtained from this model, and the test data presented in [116]. The data is generated by selecting one node centrally positioned at the end of the cantilever.

4.6.2 Simulating separation of through-thickness reinforced laminate

To test the capability of the model to simulate delamination of a through-thickness reinforced composite, a model of a 3D weave is created.

The geometry of the model and the mesh used is as described in section 4.6.1. The material is a 3D weave as supplied by Qinetiq, and described in detail in section 5.6.1. The material properties are as the predicted homogenized properties given in Table 5.6.

The properties applied to the cohesive separation displacement field are described

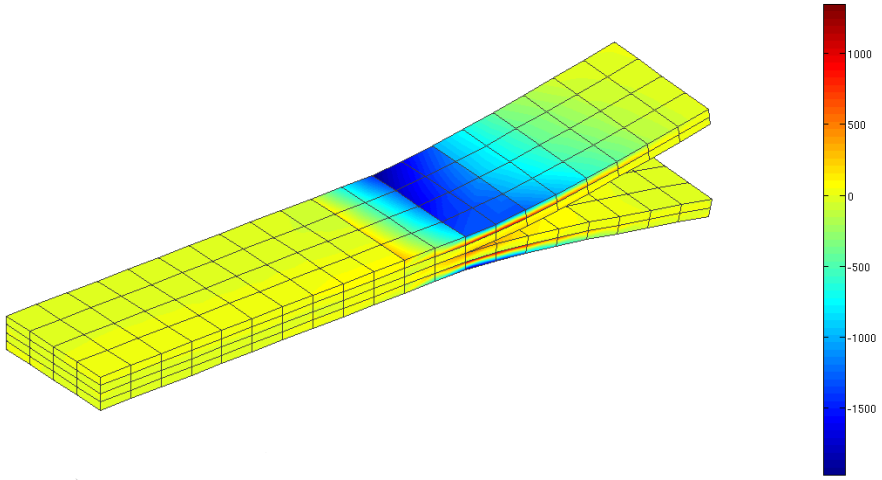

Figure 4.7: **Contour plot of bending stresses (σ_{xx})in double cantilever beam model** . The plot is made at a point shortly after the delamination has begun to propagate. Contour values are in MPa.

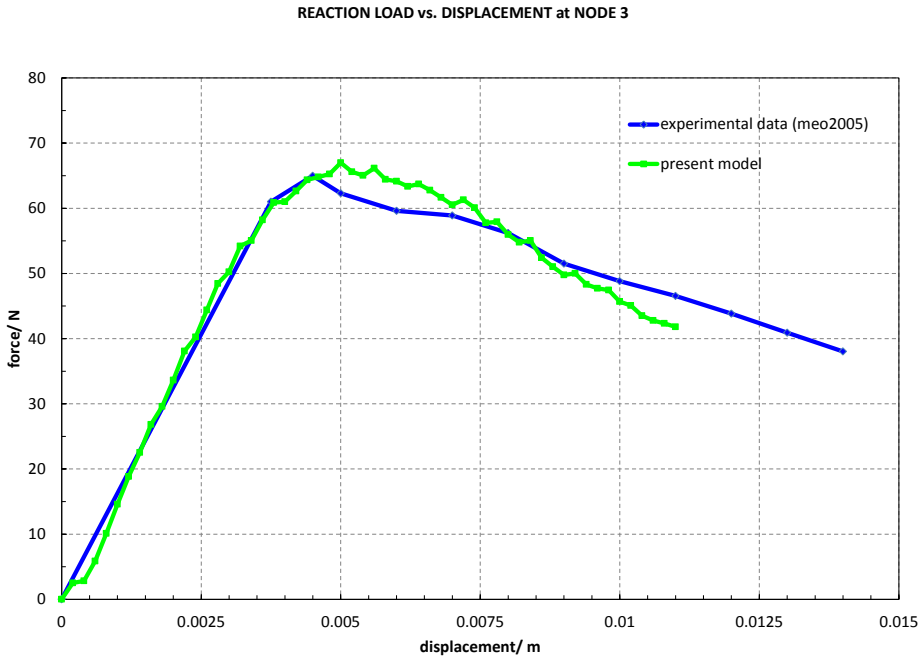

Figure 4.8: **Comparison of present model to test data** . Applied force vs. vertical displacement at end of double cantilever beam; test data taken from [116].

in Table 4.3.

The resulting force versus displacement plot is shown in Figure 4.9.

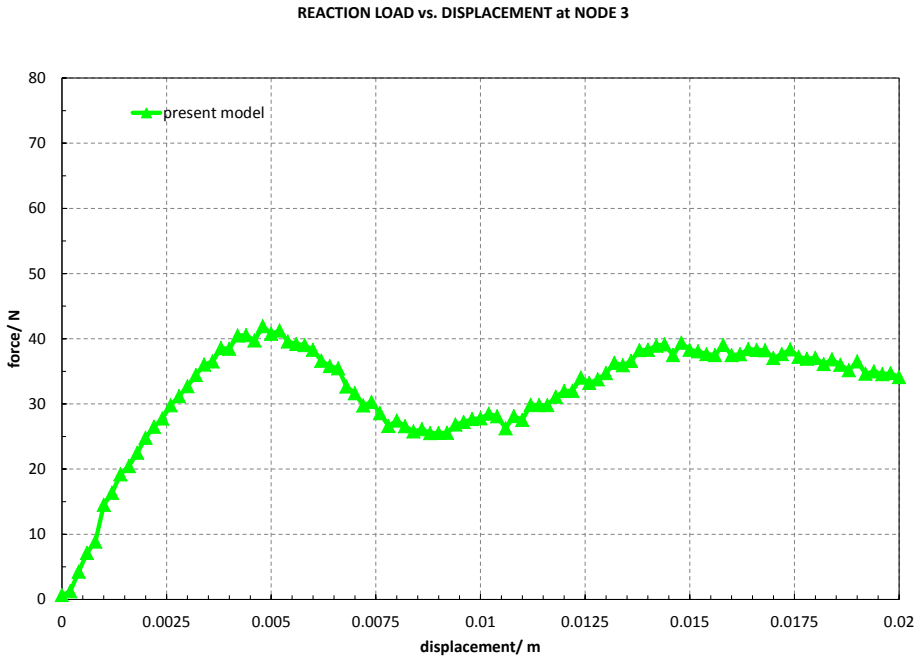

Figure 4.9: **Force vs. displacement data for separation of through-thickness reinforced 3D woven laminate** . Applied force vs. vertical displacement at end of the double cantilever beam.

4.7 Discussion

Figure 4.8 shows the force vs. displacement curve for the end point on a double cantilever beam without through-thickness reinforcement. Also shown on the plot is the experimental data presented in [116].

The model initially exhibits a low stiffness. This part of the curve represents the pre-loading of the beam in the region of the pre-existing delamination. After this point, the stiffness rapidly increases, as the body of the beam takes up load, increasing the stress at the delamination front. The stiffness response in this region is linear, and of a similar magnitude to the experimental data.

As the stress increases at the delamination front, the cohesive element ahead of the

parameter	**value**
Interface element stiffness	5500 GPa
Separation at initiation of damage u_0	7×10^{-6} m
Matrix failure separation u_1	24×10^{-6} m
Initiation of tow pullout u_2	30×10^{-6} m
Complete pullout separation u_3	10×10^{-3} m
Reinforcement fracture separation u_f	4×10^{-3} m
Through-thickness reinforcement areal density	2.04%
Reinforcement effective stiffness	4.86 GPa

Table 4.3: Reinforced delamination separation properties

delamination begins to undergo degradation. The first significant deviation from the linear response is at a deflection of ~0.0038m, and an end load of 61N. This matches the experimental data well.

Beyond this point, the experimental data reaches a peak load of 65N at a displacement of 0.0046m. The experimental data is characterised by a fairly distinct peak load. In contrast, the model presented here reaches a peak load of 68N, at an end displacement of 0.005m. This is a higher load and a greater displacement than the experimental data. Additionally, the shape of the curve is a more gradual 'maximum' than the peak exhibited by the experimental data. It is unclear if the difference is real, or an artifact of the resolution of the experimental data.

The value of the peak load and displacement predicted by the model, as well as the curve shape, indicates that the model may use a very gradual damage accumulation process, whereas the real process may be much more rapid, brittle degradation.

After the peak load, the displacement continues to increase as the reaction force reduces. In the model, this reduction is slightly more rapid than in the experimental data.

The model is illustrated in Figure 4.7. The contours on the model illustrate the bending stresses within the model. Note, in the implementation of the model, the discontinuous displacement field (i.e. the cohesive elements) are not rendered, thus there is still traction across the surface where only a small separation of the plies is illustrated.

The second model, the results of which are presented in Figure 4.9 shows the response of a similar double cantilever beam, but with through-thickness reinforcements (i.e. a 3D weaved construction). The 3D weave is based upon material specifications supplied by Qinetiq, however no test data has been generated to validate this model.

The initial parts of the model exhibit similar behaviour to the unreinforced double cantilever beam, exhibiting initial low stiffness followed by linear behaviour. After the peak load, the matrix failure results in a gradual reduction of the load, until

the separation increases to the point where the binder tows 'catch' and retard the progression of the delamination. This region exhibits a low stiffness: this is because despite the high modulus of the binder tows, there are relatively few of them (i.e. the areal density is low). After an end displacement of 0.015m, a second peak load of ~40N is reached, after which a gradual reduction in the reaction force is observed. This corresponds to the tow pullout phase.

The model is terminated due to inability to solve the system when the delamination front reaches the end of the DCB specimen.

4.8 Conclusions

A model has been developed here to simulate the separation of plies in a 3D woven composite material. To do this, it uses familiar cohesive models from laminate analysis, and incorporates an extra part to the cohesive law to simulate tow pullout and fracture. In this way, it is able to simulate the large distortion to failure that are characteristic of 3D woven materials.

The model has been incorporated into the multi-scale laminate analysis method developed in Chapter 3, by applying the developed cohesive element as a discontinuous through-thickness displacement field that can be superimposed upon all the other displacement fields used. The implementation in the multi-scale model provides a powerful solution, able to simulate complex delamination behaviour including multiple overlapping and partially overlapping delaminations.

Though test data is not available to validate the pullout simulation, the model has been compared to test data of delamination in an unreinforced double cantilever beam. The model results indicate that the model is able to capture the response of the material adequately. A simulation of the failure of a reinforced laminate has indicated that the model responds in a manner that is consistent with the expected behaviour.

This model provides the necessary capability to simplify the simulation of 3D weaved structures incorporating delamination to that of an effective 2D problem. In combination with the model of Chapter 3, an efficient model can be used to predict accurate interlaminar stresses and progress a delamination. However, ply separation and delamination is only one mechanism by which the 3D weaved composite can fail. To simulate damage within plies, or in the interlaminar binder tows, a local damage diffuse damage model is required. A continuum damage model is developed in the following chapter to address this need.

Chapter 5

Modelling damage on the tow scale

5.1 Introduction

The use of 3D composites requires analysis techniques to account for the complex arrangement of the tows which affects the failure mechanisms that it will undergo. Existing analysis methods for 2D composites treat laminates or individual plies as homogeneous, i.e. without direct reference to the underlying tow structure. Some of these methods can be extended to be applied to 3D composites, such as mosaic models, volumetric stiffness averaging, however, these do not account for the effect of the tow structure on the failure mode.

In this section, a model is developed to simulate the effect of progressive failure of the tows on the macroscopic mechanical properties of the 3D weaved composite.

5.2 Literature review

5.2.1 Asymptotic homogenization

A feature of the 3D composite weaves examined here is that they are periodic, i.e. their structure repeats at regular intervals. The ratio of the period length to a typical structural length is small, and the coefficients of a partial differential description of the problem will be periodic.

One appropriate method for analysing such a problem is the asymptotic expansion homogenization method (AEH). AEH is a method used to decompose a function into global (smoothed) and local (oscillating) components. Bensoussan et al. [117] describe the method as 'obtaining by systematic expansion procedures the passage from a microscopic description to a macroscopic description of the behaviour of the system'. An AEH analysis allows the smoothed solution to be determined (homogenization) for use in a macro-scale analysis, and additionally allows determination of the micro-scale state (localization) from the point conditions in a macro-scale analysis. A more

complete description of the method is given in da Cruz et al. [118], and outlined in section 5.4.1.

AEH has been used for the analysis of composite materials with 3D structures [71], structures with embedded sensors (smart materials) e.g. [119, 120], and for various types of multiphase materials [121].

The AEH method assumes that the structure is, and remains, periodic. Thus it is not directly suitable for determining the behaviour of a structure with localized effects. It is however useful to determine the material behaviour within localized regions, possibly for inclusion at a point within a larger structural scale model. An approach similar to this is conducted by Takano and Okuno [122], Takano et al. [123], who combine the AEH method with mesh superposition to give a solution method for a three-scale problem (the tow/matrix scale, the homogenized local scale, and a structural scale).

The ability of the AEH method to simulate periodic structures and transfer information (in this case, the stress state) between two scales in both directions makes it ideal for application to the mechanical simulatio of a 3D woven composite.

5.2.2 Continuum damage modelling

One of the methods to account for the change in behaviour that damage has on a composite structure is the material property degradation method (MPDM). Upon initiation of damage, the material constants (such as modulus and Poisson's ratio) can be changed to some appropriate value. This is a continuum approach, since some assumptions are made as to how the microstructural damage affects the macroscale, homogenized properties.

Stiffness reduction is the simplest implementation of this. Reddy et al. [38] uses this in a layerwise formulation using a stiffness reduction coefficient (SRC). It is noted that in a conventional stiffness reduction scheme, an element is considered failed once any point within it has met the failure criteria, e.g. (2.4)), and the stiffness of the element is set to zero. This type of model is also referred to as 'ply-discount' when applied to the failure of entire lamina. In [38] however, the SRC is a variable in the range 0–1, and indicates the change in stiffness the failure represents within the element. The model is solved by incrementally loading the element until it reaches failure, followed by reducing the stiffness. Loading of the element is then continued, and it is allowed to fail repeatedly, each time reducing in stiffness, thus modelling progressive failure. The solution method imposes solution in a large number of small load steps, and requires an SRC of near unity.

The results show that the method is superior to immediate reduction of stiffness to zero in predicting ultimate failure load, but the load-displacement relationship is highly dependent on the choice of SRC. A similar approach is taken by Praveen and Reddy [124] and applied to a laminate with transverse cracks perpendicular to the loading direction, and an upper bound for the effective stiffness is well described.

In a more advanced continuum damage model, it is assumed that the load carrying capacity of the material is reduced by the presence of defects. Depending on the complexity of the model, the defects can be considered to reduce the load carrying capacity equally in each direction, or differing amount in various directions. Figure 5.1 shows the defects in three perpendicular directions, aligned with the fibres and lamina, to give an orthotropic model. Additional complexity can be added to the model to account for the different behaviour under tensile and compressive loads.

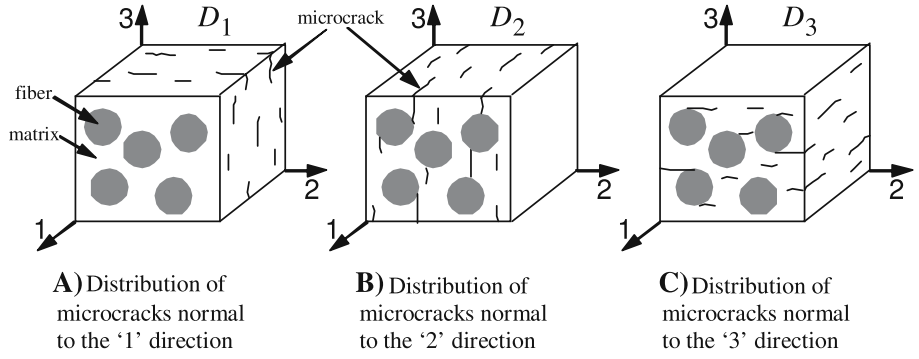

Figure 5.1: **Distribution of microcracks in a RVE** of a unidirectional composite, showing the different orientations as used by an orthotropic damage model [125]

The concept of 'effective stress' is introduced, where the total load is carried on the remaining, undamaged material. In the simplest case, for isotropic damage, a scalar damage variable D is introduced as a volume or area density of the damage:

$$D = \frac{\delta A_d}{\delta A} \tag{5.1}$$

where A is the nominal total area, and A_d is the area of the defects (Figure 5.2).

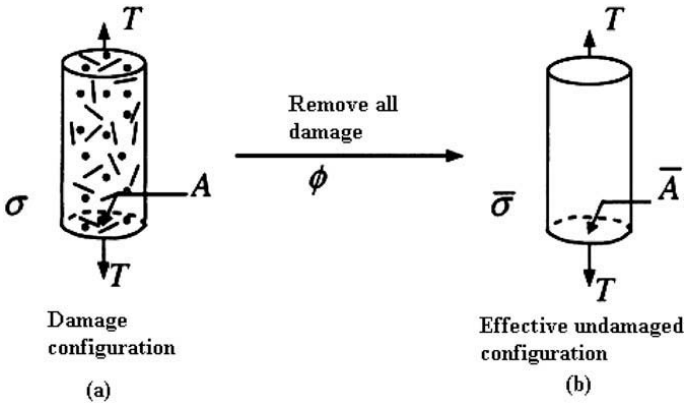

Figure 5.2: **Representation of the damage homogenization process** The real damaged microstructure (a) is homogenized (b) by determining an effective area, $\bar{A}$, over which the load T acts, giving an effective stress $\bar{\sigma}$ [126].

The effective stress, $\hat{\sigma}$ is then given as a function of the nominal stress, σ:

$$\hat{\sigma} = \frac{\sigma}{1-D} \tag{5.2}$$

and then, using a principle of elastic energy equivalence, the effective strain $\hat{\varepsilon}$ and modulus $\hat{E}$ can be shown to be [127]:

$$\hat{\varepsilon} = (1-D)\varepsilon \qquad\qquad \hat{E} = E(1-D)^2 \tag{5.3}$$

Lemaitre and Desmorat [128] show how this can be extended to its most general case for anisotropic damage, using a 4-dimensional damage tensor $\underline{\boldsymbol{D}}$ and damage effect tensor $\underline{\boldsymbol{M}}$:

$$\hat{\sigma}_{ij} = M_{ijkl}\sigma_{kl} \qquad\qquad M_{ijkl} = (\underline{\boldsymbol{I}} - \underline{\boldsymbol{D}})^{-1}_{klij} \tag{5.4}$$

In the case of a composite material with orthotropic material properties, [129] states that a second-order damage tensor with principal directions coinciding with the principal material directions is capable of describing most of the typical crack formation modes (orthotropic damage), as in Figure 5.1. [125] goes on to derive the symmetric effective stress tensor, and the effect on the stiffness matrix:

$$\begin{aligned}
\bar{C}_{\alpha\beta} &= C_{\alpha\beta}(1-D_\alpha) && \text{for } \alpha,\beta = 1,2,3 \\
\bar{C}_{44} &= C_{44}(1-D_2)(1-D_3) \\
\bar{C}_{55} &= C_{55}(1-D_3)(1-D_1) \\
\bar{C}_{66} &= C_{66}(1-D_1)(1-D_2)
\end{aligned} \tag{5.5}$$

where C are the undamaged stiffness coefficients, $\bar{C}$ are the damaged material coefficients, and D_i are the three components of a second-order, orthotropic damage tensor. A very similar model is presented in Camanho and Matthews [130] for progressive damage, where instead of the stiffness coefficients, the engineering constants (E, G) are modified by a 'degradation factor'[1].

Tay et al. [43] provide a good review of the various MPDM and CDM schemes. The authors note that the simplicity of these models, operating on the homogenized variables, make them particularly suited to implementation in FE codes. They also note the shortcomings of the technique for modelling macroscopic cracks, such as delamination. Pavan et al. [126] develop a continuum model by developing a hardening law associated with the damage process, based on experimental results. The model is based upon the familiar process of considering damage in the homogenized variables, but then goes on to account for the microstructure by considering the distribution of the damage D into the consituents of the composite.

[1] The 'degradation factor' used in [130] is a state variable that multiplies the elastic constants, and progresses through the range 1–0. The 'damage factor', more commonly used in CDM, progresses from 0–1. The two concepts are essentially identical.

In the process they note that the damage effect tensor ordinarily results in a non-symmetrical effective stress tensor. Voyiadjis and Park [131] explain that this significantly complicates the theory, and is best avoided. They explore the various symmetrization schemes that have been presented, and notes two commonly used methods for second-order damage tensors:

$$\hat{\sigma}_{mn} = (\delta_{mp} - D_{mp})^{1/2}\sigma_{pq}(\delta_{nq} - D_{nq})^{1/2} \tag{5.6}$$

$$\hat{\sigma}_{mn} = \frac{1}{2}\left[\sigma_{mr}(\delta_{rn} - D_{rn})^{-1} + (\delta_{nr} - D_{nr})^{-1}\sigma_{rm}\right] \tag{5.7}$$

Barbero et al. [132] apply the CDM concept to a 2D plain weaved composite by incorporation into an FE micromechanical model of a RUC. The formulation is based on the strain energy density within the composite, and includes a number of damage evolution parameters and a damage threshold variable, used to tune the model to match experimental data.

Maimí et al. [133] also develop a damage model for orthotropic damage in laminar composites, based on phenomenological failure criteria set out in LaRC03 [35] and LaRC04 [36]. The physically based damage models introduce a more detailed consideration of the microstructure that is lacking in some of the other models that operate on only the homogenized variables. The same approach is also used for transversely isotropic composites [134]. The result is a damage model that is capable of accurately predicting the damage modes and effects caused by the failure modes described by LaRC04.

5.2.3 Spatially averaged effects of tow-scale damage

The effects of damage at this scale are captured by Cox [21]. The diffuse damage initially causes softening of the effective response of the homogenized material, via matrix micro-cracking. This can introduce a significant nonlinearity into the system long before fibre failure and ultimate failure. As the matrix reduces in strength, the tows take up more of the load. This will eventually lead to tow failure, and a step change in the spatially averaged response of the material. At this point, the stress can redistribute amongst the unfailed tows. Depending on the location and nature of the initial tow failures, this can cause not only changes to the direct stiffnesses at the averaged scale, but effects such as tension-bend or tension-twist coupling. Another feature of failure in 3D weaved composites is fibre pullout, by which the composite material can retain a large portion of its strength by means of friction between the tow and surrounding material as the fractured tow is being pulled out. By appropriate choice of stress-separation functions for the tow material, this effect can be captured in the simulation.

The eventual effect of tow scale damage is to reduce the effective properties of the unit cell to such low values as to be considered incapable of sustaining any meaningful load at the macro-scale.

5.3 Aims

The aim of the analysis presented here is to ultimately to understand the behaviour of a 3D weaved component at the structural scale. Ideally, any analysis method will be able to determine structural scale response, without the expense of performing micro-scale analyses at all points in the structure. To do this, a method to determine an overall response from underlying micro-scale features (such as damage) is required, as is a method to transfer loads from a macroscopic scale to the micro-level in order that the damage can accurately be simulated.

To achieve this aim, a damage model based on the asymptotic expansion homogenization scheme is developed. In the wider context of this thesis, this damage model will provide simulation of in-plane damage in a 3D weaved composite, accounting for phenomena such as matrix micro-cracking, fibre failure and fibre-matrix debonding, whereas ply separation and the effect of binder tow pullout are simulated elsewhere.

5.4 Method

5.4.1 Asymptotic homogenization

The unit cell of the composite material is defined as the smallest unit that can be repeated to form the structure of the material. The unit cell is assumed to be much smaller than the global structure, and the displacements are represented over a microscopic length-scale (or coordinate system), y. These displacements are oscillating and periodic, and can be smoothed to the global (macro-) length scale, x. The length scales are related by a scale parameter, ϵ:

$$y = x/\epsilon \tag{5.8}$$

The displacement is composed of the smoothed global displacements, and the local micro-scale oscillations, and is represented with the series expansion:

$$u^\epsilon = u^{(0)}(x,y) + \epsilon u^{(1)}(x,y) + \epsilon^2 u^{(2)}(x,y) + \cdots \tag{5.9}$$

where $u^{(n)}$ represents the displacement on a particular length scale.

This displacement field definition is substituted into the standard equations of elasticity to give the problem definition:

$$\varepsilon^\epsilon_{ij} = (u^\epsilon_{i,x^\epsilon_j} + u^\epsilon_{j,x^\epsilon_i})/2 \tag{5.10}$$

$$\sigma^\epsilon_{ij} = C_{ijkl}(x,y)\varepsilon_{ij}(x^\epsilon) \tag{5.11}$$

$$\sigma^\epsilon_{ij,x^\epsilon_j} + f_i = 0 \tag{5.12}$$

where the subscript $_{,x}$ represents a partial derivative with respect to x. Where derivatives are taken with respect to the 'true' coordinates x^ϵ, the chain rule is applied:

$$\frac{\partial}{\partial x^\epsilon} = \frac{\partial}{\partial x} + \frac{1}{\epsilon}\frac{\partial}{\partial y} \tag{5.13}$$

Substituting (5.9) into (5.10) and (5.11) gives the series expansion:

$$\varepsilon_{ij}^\epsilon = \frac{\epsilon^{-1}}{2}(u_{i,y_j}^{(0)} + u_{j,y_i}^{(0)}) + \frac{\epsilon^0}{2}(u_{i,x_j}^{(0)} + u_{j,x_i}^{(0)} + u_{i,y_j}^{(1)} + u_{j,y_i}^{(1)}) + \frac{\epsilon^1}{2}(u_{i,x_j}^{(1)} + u_{j,x_i}^{(1)} + u_{i,y_j}^{(2)} + u_{j,y_i}^{(2)}) + \cdots \tag{5.14}$$

$$\sigma_{ij}^\epsilon = \epsilon^{-1}C_{ijkl}(x,y)\varepsilon_{kl}^{-1}(x,y) + \epsilon^0 C_{ijkl}(x,y)\varepsilon_{kl}^0(x,y) + \epsilon^1 C_{ijkl}(x,y)\varepsilon_{kl}^1(x,y) + \cdots \tag{5.15}$$

Here, only terms up to ϵ^1 are shown.

Then, substituting (5.15) into (5.12), the terms with the same power of ϵ can be equated to give the following set of relationships:

$$\epsilon^{-2} : \sigma_{ij,y_j}^{(-1)}(x,y) = 0 \tag{5.16}$$

$$\epsilon^{k} : \sigma_{ij,x_j}^{(k)}(x,y) + \sigma_{ij,y_j}^{(k+1)}(x,y) = 0 \text{ for } k = -1,1,2,3,\ldots \tag{5.17}$$

$$\epsilon^{0} : \sigma_{ij,x_j}^{(0)}(x,y) + \sigma_{ij,y_j}^{(1)}(x,y) + f_i = 0 \tag{5.18}$$

where

$$\sigma_{ij,x_j}^{(m)}(x,y) = C_{ijkl}(x,y)\varepsilon_{kl}^{(m)}(x,y) \text{ for } m = -1,1,2,3,\ldots \tag{5.19}$$

The term in ϵ^{-2} (5.16) can be multiplied by $u_i^{(0)}(x,y)$ and integrated by parts to show:

$$\int_{\partial y} u_i^{(0)}\sigma_{ij}^{(-1)}n_j \mathrm{d}\gamma - \int_\gamma u_{i,y_j}^{(0)}C_{ijkl}u_{k,y_l}^{(0)}\mathrm{d}\gamma = 0 \tag{5.20}$$

where γ represents the domain of the unit cell, and $\partial\gamma$ its boundary. Since the unit cell is defined as periodic, the boundary integral (the first term in (5.20)) is zero, hence:

$$u_{i,y_j}^{(0)}(x,y) = 0 \tag{5.21}$$

i.e. the $u^{(0)}$ term in (5.9) is independent of the micro-scale coordinate y, and represents a smoothed global displacement.

The term in ϵ^{-1} (5.17) relates the micro-scale oscillating displacement $u^{(1)}$ to $u^{(0)}$. Substituting in (5.15),

$$[C_{ijkl}(e_{klx}(u^{(0)}) + e_{kly}(u^{(1)}))]_{,y_i} = 0 \tag{5.22}$$

where

$$e_{klx} = \frac{1}{2}\left(\frac{\partial}{\partial x_k} + \frac{\partial}{\partial x_l}\right) \tag{5.23}$$

Using separation of variables on (5.22), the micro-scale displacement is rewritten as:

$$u^{(1)}(x,y) = \chi^{kl}(y) e_{klx}(u^{(0)}(x)) \tag{5.24}$$

where χ is a oscillating function with period equal to the unit cell dimensions. χ is often referred to in the literature as the 'corrector'. Substituting this into (5.15), we get:

$$\sigma_{ij}^{(0)}(x,y) = \left[C_{ijkl} + C_{ijkl} e_{ijy}\left(\chi^{kl}(y)\right)\right] e_{klx}\left(u^{(0)}(x)\right) \tag{5.25}$$

We also note that the first term in (5.15) is zero (since $u^{(0)}$ is a function of x only), and we choose to ignore terms in ϵ^1 and higher powers, since ϵ is small. Thus, $\sigma^{(0)}$ is the approximation of the stress in the unit cell, and is a function of the macro-scale strain, and the derivatives of the corrector χ. The mean stress in the unit cell can be determined by averaging the term in square brackets in (5.25) to give an effective or homogenized property matrix, $\overline{C}_{ijkl}$:

$$\overline{C}_{ijkl} = \frac{1}{\gamma} \int_{\gamma} C_{ijkl} + C_{ijkl} e_{ijy}\left(\chi^{kl}(y)\right) \mathrm{d}\gamma \tag{5.26}$$

The corrector χ is determined from

$$\left(C_{ijkl} + C_{ijkl} e_{kly}(\chi_i^{kl})\right)_{,y_j} \tag{5.27}$$

by using the principle of virtual displacements.

Implementation as a finite element model

In its discretized form, the finite element equation is

$$\mathbf{KX} = \mathbf{F} \tag{5.28}$$

where

$$\mathbf{K} = \int_{\gamma} \mathbf{B}^T C \mathbf{B} \mathrm{d}\gamma \tag{5.29}$$

$$\mathbf{F} = \int_{\gamma} \mathbf{B}^T C \mathrm{d}\gamma \tag{5.30}$$

and $\mathbf{B}$ is the shape function derivative matrix. $\mathbf{X}$ is the discretized form of the corrector χ. Using the corrector, we used the discretized form of (5.26) to determine the effective macro-scale material properties of the unit cell:

$$\overline{C} = \frac{1}{V} \int_{V} C(y) + C(y) \frac{\partial X(y)}{\partial y} \mathrm{d}V \tag{5.31}$$

Similarly, the distribution of the macro-scale load onto the micro scale can be determined from (5.25) to guide the calculation of damage in the individual tows or matrix:

$$\sigma(x,y) = \left[C(y) + C(y)\frac{\partial X}{\partial y}\right]\varepsilon(x) \tag{5.32}$$

where ε is the macro-scale strain at a point in the macro scale.

5.4.2 Continuum damage modelling

Damage can be modelled in a number of different ways. In this work, damage is modelled in each of the constituents (typically tow and matrix) using a continuum damage model. This allows damage to be considered as a series of microcracks within both the tow and the matrix, representing a reduction in the load carrying area of the material. In each of the orthogonal directions, the damage parameter d calculated:

$$d = 1 - \frac{A}{A_0} \tag{5.33}$$

where A is the load carrying area, and A_0 is the initial undamaged load carrying area. The reduction in area results in the increase of stress. The 'effective stress', $\hat{\sigma}$,is given by:

$$\hat{\sigma} = \mathbf{M}\sigma \tag{5.34}$$

where σ is the undamaged stress, and $\mathbf{M}$ is the damage effect tensor. The diagonal terms of $\mathbf{M}$ take the form:

$$\mathrm{M}_{ii} = \frac{1}{1-d_i} \tag{5.35}$$

where $0 \leq d \leq 1$. Depending on the properties of the material being examined, the values of d_i can be independent from each other. For the most general case, the damaged compliance matrix, $\hat{\mathbf{S}}$, can then be given as:

$$\hat{\mathbf{S}} = \begin{bmatrix} \frac{1}{(1-d_1)E_1} & -\frac{\nu_{21}}{E_2} & -\frac{\nu_{31}}{E_3} & 0 & 0 & 0 \\ -\frac{\nu_{12}}{E_1} & \frac{1}{(1-d_2)E_2} & -\frac{\nu_{32}}{E_3} & 0 & 0 & 0 \\ -\frac{\nu_{13}}{E_1} & -\frac{\nu_{23}}{E_2} & \frac{1}{(1-d_3)E_3} & 0 & 0 & 0 \\ 0 & 0 & 0 & \frac{1}{(1-d_4)G_{23}} & 0 & 0 \\ 0 & 0 & 0 & 0 & \frac{1}{(1-d_5)G_{13}} & 0 \\ 0 & 0 & 0 & 0 & 0 & \frac{1}{(1-d_6)G_{12}} \end{bmatrix} \tag{5.36}$$

representing the degradation in stiffness of the material constituent. The effective stiffness matrix, $\hat{\mathbf{C}} = \hat{\mathbf{S}}^{-1}$, i.e.

$$\begin{aligned} \varepsilon &= \mathbf{S}\hat{\sigma} \\ &= \mathbf{S}\mathbf{M}\sigma \\ &= \hat{\mathbf{S}}\sigma \end{aligned} \tag{5.37}$$

Damage evolution

The growth of the damage is described with a damage evolution law, based on the damage energy release rate. The Gibbs free energy is given by:

$$\psi(\sigma, d, p) = \sigma^e(\sigma, d) + \sigma^p(p) \tag{5.38}$$

where the superscripts e and p represent the elastic and plastic components of the energy, and p is the accumulated inelastic strain. Here, inelastic damage is not considered, so the damage energy release rate Y, is given by:

$$Y = \frac{\partial \psi}{\partial d} = \frac{\partial \psi^e}{\partial d}, \text{ where } \psi^e(\sigma, d) = \frac{1}{2}\sigma : \hat{\mathbf{S}} : \sigma \tag{5.39}$$

i.e.

$$Y_i = \frac{\sigma_i^2}{2E_i(1-d_i)^2} \tag{5.40}$$

In this model, the damage growth is a linear function of $\sqrt{Y}$:

$$d_i = \frac{\sqrt{Y_i} - \sqrt{Y_{th,i}}}{\sqrt{Y_{cr,i}} - \sqrt{Y_{th,i}}} \tag{5.41}$$

where the subscripts th and cr represent threshold and critical values of Y respectively.

For the purpose of numerical simulation, the damage parameters d_i are limited to the range $0 \leq d_i \leq 0.999$ to prevent singularity in the stiffness matrix.

The model is solved by using an iterative process to determine the equilibrium for a given loading condition.

5.4.3 Coupled model, and model implementation

The solution process is outlined in Figure 5.3. The macro-scale load, i.e. a point stress state from a model ignoring micro-scale perturbations, is applied incrementally to a finite element model of the repeating unit cell. The homogenization method (section 5.4.1) is used to determine the local correctors, χ. These are used to determine the micro-scale stress state, from which the damage at the tow/matrix scale can be determined, using appropriate damage criteria. The stiffness degradation method (section 5.4.2) is used to determine the effective material properties of each of the elements. A convergence iteration is conducted to achieve equilibrium between the macro- and micro-states. The convergence criteria is that no additional damage is created in the elements on application and distribution of the macro-scale load.

Once equilibrium is achieved, the effective elasticity matrix of the unit cell can be determined (5.26) and the macro-scale load can be incremented to the next load step. In this manner, a stress-strain curve for the material can be derived.

Final failure is determined by an arbitrarily large volume averaged strain during the convergence iteration. In the unit cell case, a large strain indicates that the material properties have degraded such that there is no continuous load path across the unit cell. In this model, a value of 0.1 (10%) has been used.

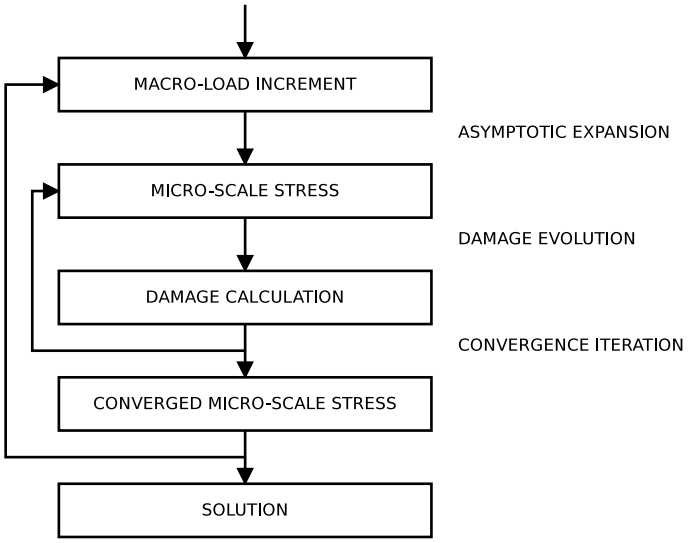

Figure 5.3: Flow diagram of the analysis process

Convergence and termination criteria

The inner convergence loop (Figure 5.3) is iterated until two sucessive iterations differ by less than 1%. This value has been chosen by experimentation to give an acceptable solution without an excessive number of iterations which increase the computational cost of the method.

Termination of the model is done when any of the effective direct stiffnesses reach less than 10% of their initial values. This value is arbitrarily chosen to represent the point at which the unit cell can no longer be considered to provide a larger structure with any practical stiffness.

5.5 Summary of method

An iterative model is developed whereby a point stress from a macro- or component-scale model is applied to a unit cell finite element model. The model is solved by an AEH scheme, whereby the stresses in the constituent components of the unit cell are determined. These are used in a continuum damage model to determine damage initiation and evolution, to simulate effects such as matrix micro-cracking, fibre failure and fibre pullout. These effects are described using a damage energy release rate. the degraded material properties are then used to homogenize the unit cell to determine

test type	loading axis	tested specimens
uniaxial tensile	0°	6-off
uniaxial compressive	0°	6-off
shear	45°	6-off

Table 5.1: Loading conditions for mechanical testing

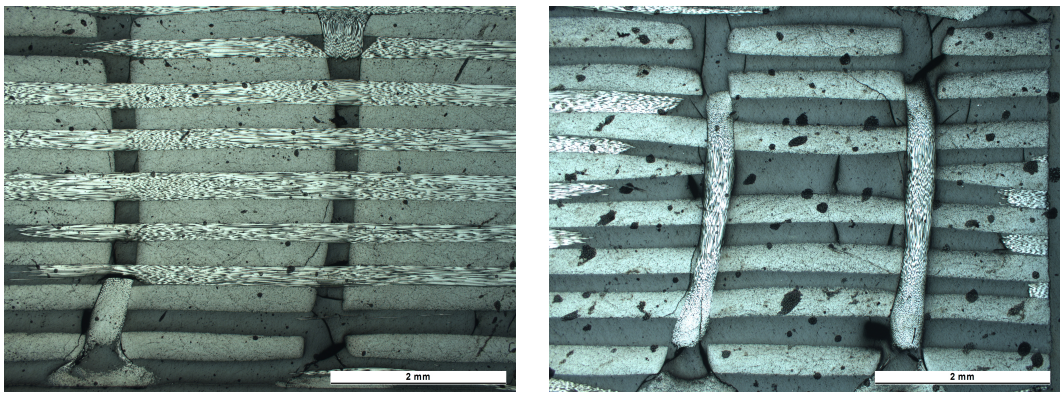

(a) 0° section (b) 90° section

Figure 5.4: **Micrograph images of sectioned weaved composite** , (a) warp direction; (b) weft direction. (Images supplied by Qinetiq.)

the effective material properties, that can be passed up to a longer length-scale model in a complete system.

5.6 Results

5.6.1 Validation against test results

A number of specimens were tested by Qinetiq under one of three monotonic loading conditions—tensile, compressive, and shear. The details of the testing are given in Table 5.1.

Micrograph images of sections taken of the weaved composite (Figure 5.4) are examined to determine the dimensions of the unit cell. The cross sections of a number of tows are measured, and the mean dimensions are used to build the unit cell finite element model. The dimensions are given in Table 5.4, and the resulting idealized model mesh is illustrated in Figure 5.5.

Material properties are applied from Table 5.2 and Table 5.3. The tow material is identical for warp, weft and binder tows. Unless otherwise indicated, the data comes from manufacturer data sheets.

The strengths in Table 5.2 and Table 5.3 are used for the damage model. The load

	tow property	MPa
El	longitudinal modulus	238 600
Et	transverse modulus*	19 800
Gp	in-plane shear modulus*	6 600
Go	out-of-plane shear modulus*	9 900
Xt	longitudinal tensile strength	3 950
Xc	longitudinal compressive strength*	2 620
Yt	transverse tensile strength*	92.5
Yc	transverse compressive strength*	92.5
Sp	in-plane shear strength*	92.5
So	out-of-plane shear strength*	92.5

Table 5.2: tow properties applied to the model. Values indicated with a * have been estimated in the absence of manufacturer data, by scaling data from other materials.

	matrix property	MPa
E	direct modulus	3 100
G	shear modulus	1 150
Xt	tensile strength	77.6
Xc	compressive strength*	77.6
S	shear strength*	38.8

Table 5.3: matrix properties applied to the model. Values indicated with a * have been estimated in the absence of manufacturer data, by scaling data from other materials.

warp tow	height/ mm	0.24
	width/ mm	2.02
	no. of layers	8
weft tow	height/ mm	0.24
	width/ mm	1.87
	no. of layers	9
binder tow	height/ mm	0.29
	width/ mm	0.29

Table 5.4: Mean tow dimensions in weaved composite sample

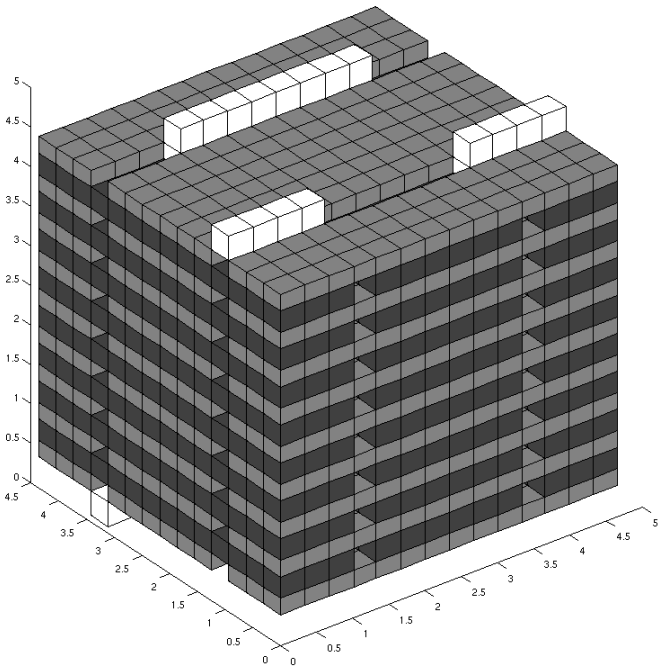

Figure 5.5: **The tow unit cell model** (matrix mesh has been removed to improve clarity). The dark tows are 'weft', the lighter tows are 'warp', and the through-thickness tows (binders) are visible in white.

Tow		**Matrix**	
longitudinal	$0.9X_t$	direct	$0.6X_t$
transverse	$0.9Y_t$		
in-plane shear	$0.9S_p$	shear	$0.6S$
out-of-plane shear	$0.9S_o$		

Table 5.5: Estimated values for damage initiation loads

at which the damage begins to accumulate, used to calculate the threshold damage energy release rate Y_{th}, was not found in literature, and the estimated values listed in Table 5.5 were used. These values were chosen to give the tows a brittle response, and the matrix a more ductile response.

The calculated elastic properties are presented in Table 5.6. These demonstrate that the values can be predicted with an acceptable level of accuracy.

The characteristic displacement diagrams, illustrating the values of the corrector χ and the displacements under unit loading in each of the 6 directions, are shown in Figure 5.6.

elastic constant	predicted	measured
E_1/ GPa	61.6	68.1
E_{45°/ GPa	9.6	11.1
E_2/ GPa	68.4	
E_3/ GPa	12.9	
G_{12}/ GPa	7.2	
G_{13}/ GPa	4.5	
G_{23}/ GPa	4.2	
ν_{12}	0.048	
ν_{13}	0.34	
ν_{23}	0.33	

Table 5.6: Predicted and measured values for elastic constants

parameter	predicted	measured range
Tensile test: Xt/ MPa	439.4	421–592
Compressive test: Xc/ MPa	420.0	377–398
Shear test: failure strength in load direction/ MPa	79.4	76–99

Table 5.7: Predicted and measured values for failure strengths

5.7 Discussion

The stress-strain diagrams in 5.7(a) and 5.7(b) for tensile and compressive loading on the 0/90° composite show that the model predicts a similar response to the tested specimens. The response is characterised by a mostly elastic behaviour, followed by a sudden brittle failure. The failure strength predicted for the tensile loading falls within the range of values from the test specimen. However, the failure mode in compression is predicted to be a greater load than that determined from testing. It is suggested that the compressive failure strength, X_c for the matrix material, may be lower than that used here.

The tensile loading on the ±45° specimen (5.7(c)) exhibits more non-linearity. The shape of the stress-strain curve suggests that the initiation of damage lags behind that in the test specimens, however the damage later 'catches-up', and follows the same stress-strain behaviour. The failure strength is also found to be within the range of the tested specimens.

The damage distribution contour-plot (Figure 5.10) and the damage fraction plots (Figure 5.9) indicates that the damage mechanism primarily responsible for the loss of stiffness when the specimen is loaded in tension is transverse damage. Transverse damage, illustrated in 5.9(b), begins to accumulate at 200MPa in the weft tows. At a load of 400MPa, the weft tows are completely damaged in the transverse directions

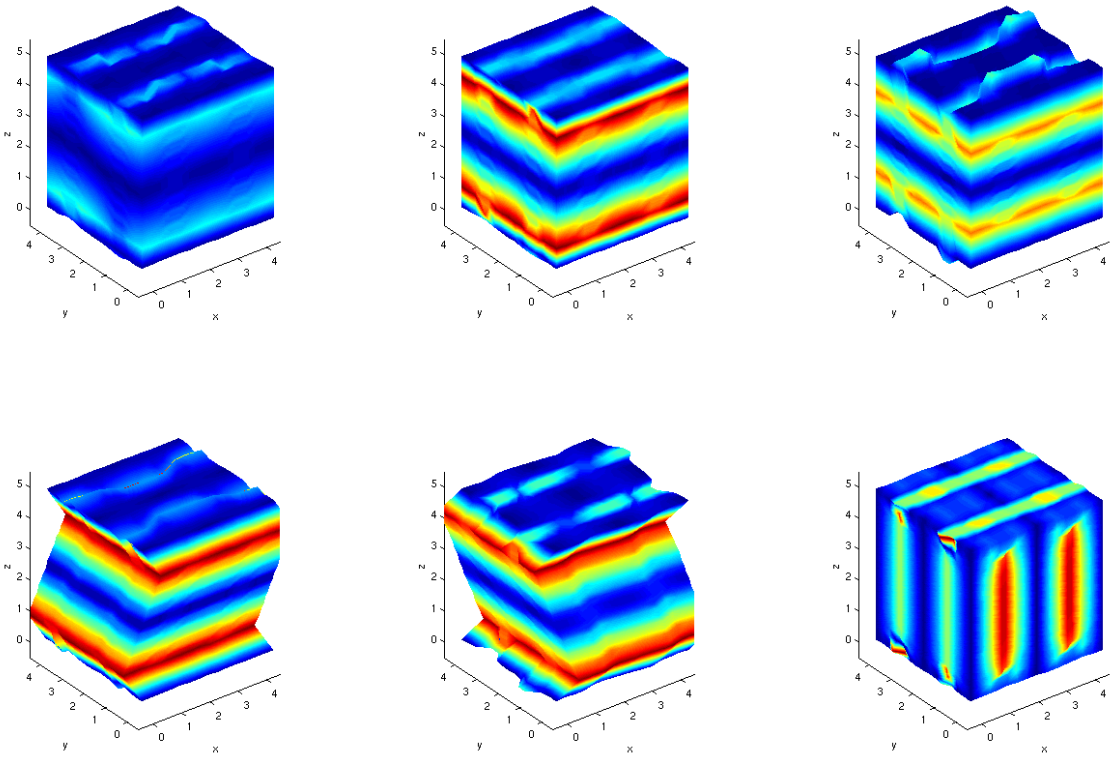

Figure 5.6: **Characteristic displacements (χ) for the unit cell.** From left to right, top row: χ_1, χ_2, χ_3; bottom row: $\chi_{23}, \chi_{13}, \chi_{12}$. The colours represent the magnitude of the displacements under the application of a unit macro-strain, with blue representing zero displacement, and red representing maximum displacement.

(i.e. $d_2 = d_3 = 1$ throughout the tow volume). This is before any longitudinal damage has accumulated in any of the tows. The effect of this transverse damage is revealed in the stress-strain response of the unit cell, 5.7(a), and in the evolution of the material properties, 5.8(a).

The material moduli in 5.8(a) are determined from the homogenized stiffness matrices from the unit cell. The Poisson ratio is calculated to be consistent with the moduli. Because the unit cell undergoes sudden changes in the modulus in individual directions, the Poisson ratio appears to behave in an erratic manner.

To understand how the damage is affecting the unit cell, the damage distribution contour plot, Figure 5.10, shows us that at a load of 220MPa, the location of the damage is concentrated in the parts of the weft tow that not directly under the binder tow. That is, the presence of the binder tow shields the weft tows from experiencing tensile strain in their transverse directions. Instead, the load is concentrated at the free sections of the weft tows, causing a localised failure across the section of the tow. This happens initially in the uppermost and lowermost weft tows, but as they fail, the load is redistributed to the central weft tows, which fail in sequence. This failure mode

results in the failure of a localized region of the tow, but in a way that reduces the ability of the tow to transfer load from one side of the unit cell to the other. As a result, the load is transferred to the matrix, which fails rapidly having inferior properties to the tow.

In this model, failure was determined by reaching a mean strain of 10% in any of the material directions during the load distribution convergence iteration. This allowed the moduli in some directions to reduce to near-zero. Because of the highly directional nature of the failure in the material tested, the material is capable of reducing the modulus to zero in one direction, and sustaining a load in another. In this testing when the applied load was uniaxial, a simple failure criterion was used, but in a more complex loading situation (for example, incorporating such a micro-scale analysis in a larger structural analysis), more complex failure criteria may be appropriate, since failure of the material in one direction does not necessarily indicate failure of the component.

5.8 Conclusions

Experimental data from tensile, compressive and shear loading of a 3D weaved composite specimen have been compared to a numerical simulation to determine the models ability to predict the material response. The model uses a finite element representation of a repeating unit cell, and uses the asymptotic homogenization method to both localize the macro-scale loads, and to determine averaged properties over the unit cell. The damage is modelled using a continuum damage model resulting in a stiffness degradation. In the tow, the damage is modelled as orthotropic, using independent failure criteria in orthogonal directions. In the matrix, the damage is modelled as isotropic, using the von Mises failure criteria.

The conclusions reached from this study are that this method is capable of determining the modulus of the composite in the direction aligned with the warp tows. Additionally the fracture strength is determined well for compressive and tensile loading in this orientation. Closer examination of these results reveal that the primary damage mechanism resulting in loss of stiffness is transverse damage in the weft tows. Transverse damage begins to accumulate much earlier than longitudinal tow damage in the unit cell, even though it is the eventual rapid increase in longitudinal damage in the warp tow that causes the composite to ultimately fail.

The binder tows strongly influence load redistribution and the position of the stress concentrations. The position of the binder tows encourages the load to redistribute the load to fail the weft tows in sequence, leading to the ultimate failure of the unit cell. This information can be used to reposition or add extra reinforcement such that the load is carried by the unit cell in a more uniform fashion.

In the composite weave examined here, matrix failure does not play a big role in

the initiation of failure. When the tows fail, the load is redistributed, and the low failure strength of the matrix causes the majority of the load to be taken up by the surrounding tows. The matrix local to a failed tow fails soon after the tow.

The model is capable of making useful and accurate predictions on the behaviour of the composite with knowledge of the weave, and is an efficient method of gathering micro-scale damage response information to be homogenized and used in macro-scale finite element modelling.

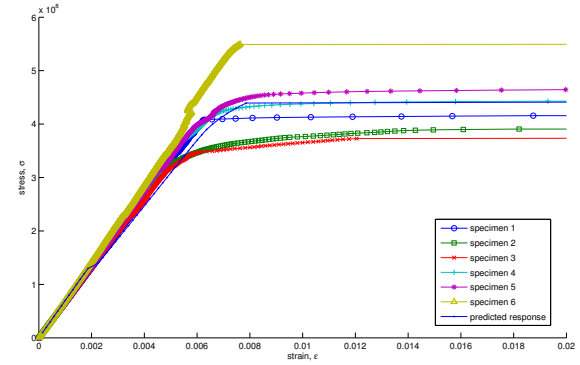

(a) tensile load

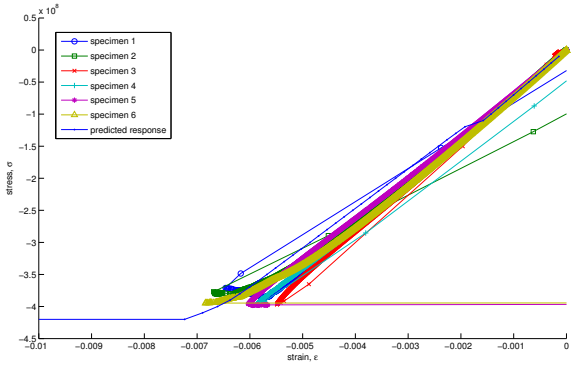

(b) compressive load

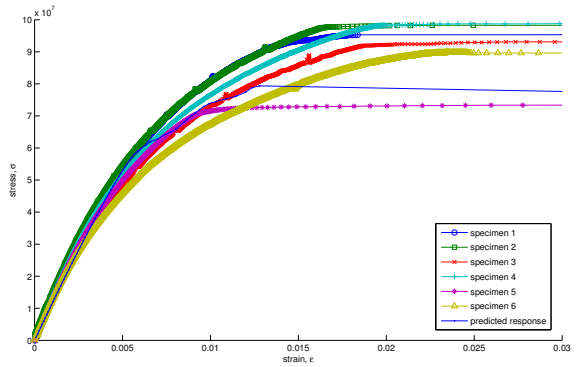

(c) tensile load on ±45 specimen

Figure 5.7: **Stress-strain plots for the various test types on each of the tested specimens**

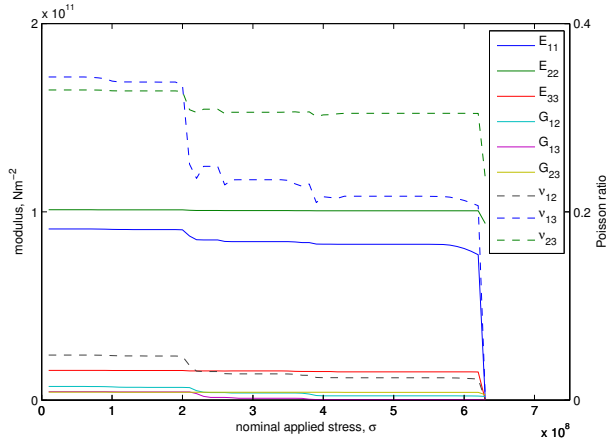

(a) tensile load

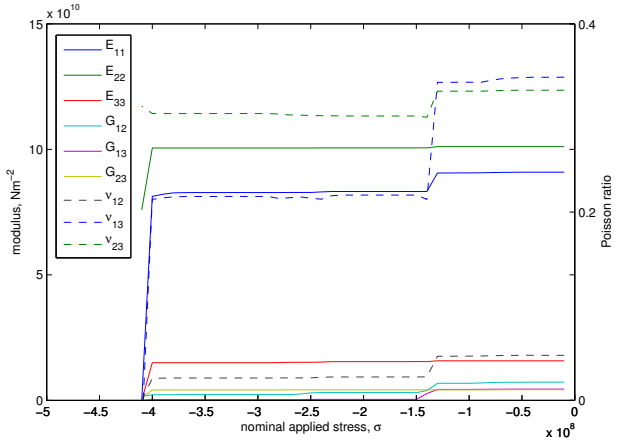

(b) compressive load

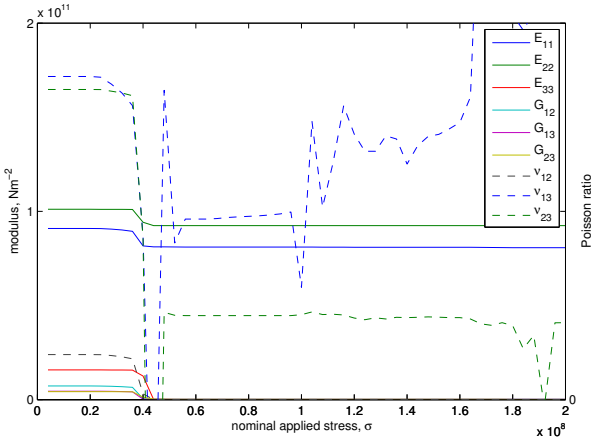

(c) tensile load on ±45 specimen

Figure 5.8: **Evolution of the material properties on application of load**

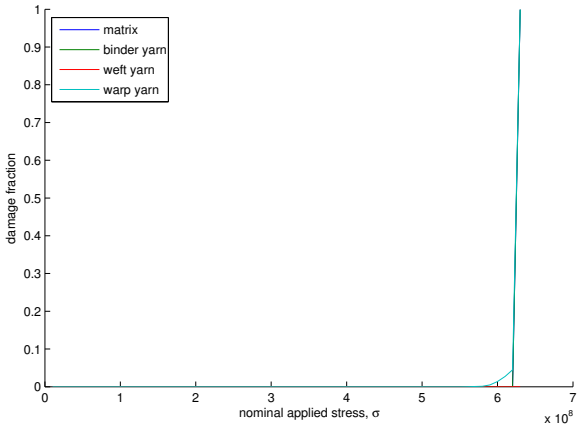

(a) damage in the tow longitudinal direction, or global x-direction (matrix)

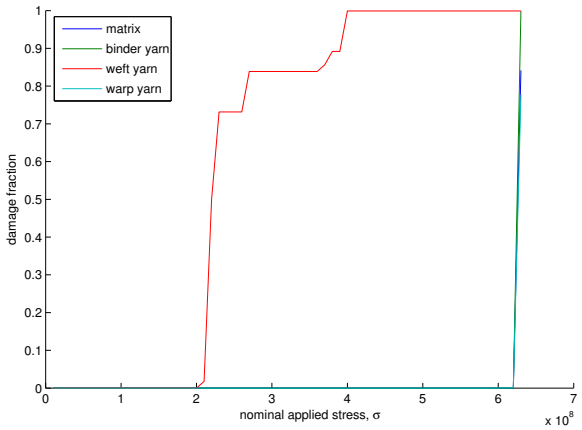

(b) damage in the tow transverse direction, or global y-direction (matrix)

Figure 5.9: **Proportion of damage in each of the constituent components of the composite**

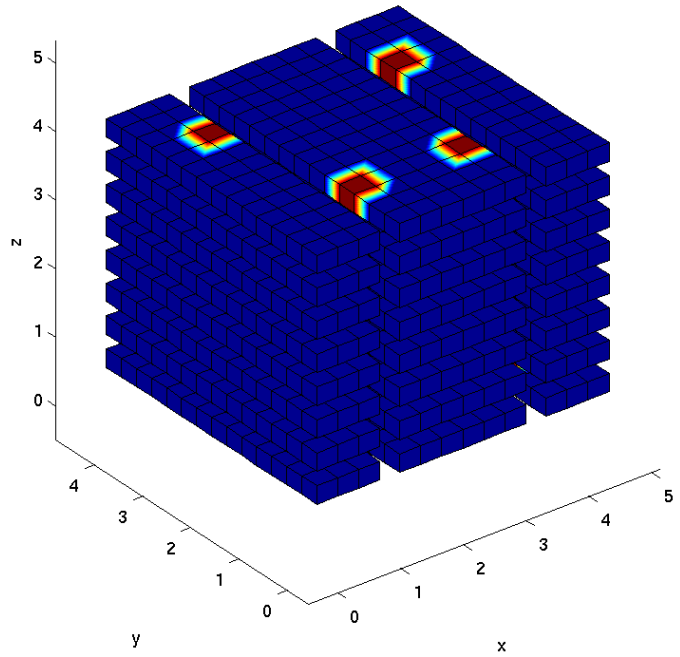

(a) 210MPa: the damage initiates at the locations on the weft tow that are able to deform without the constraint of the binder tows

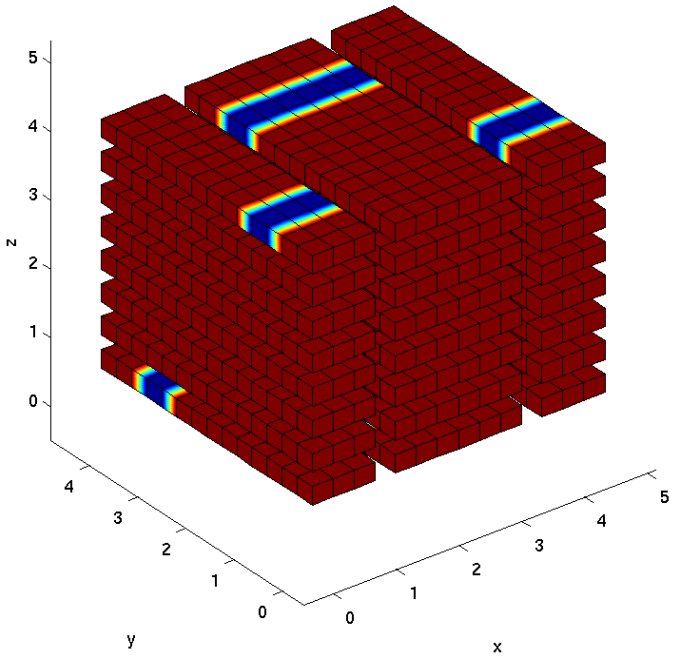

(b) 220MPa: the damage is widespread, the only remaining undamaged locations are those shielded by the binder tows

Figure 5.10: **Distribution of damage during tensile loading (at macro-scale load 210-220MPa).** Only weft tows are shown, coloured by the damage parameter d_2, representing transverse damage.

Chapter 6

A unified, multi-scale method for modelling damage

6.1 Introduction

The models presented in Chapter 3, Chapter 4 and Chapter 5 all address parts of the solution to the stated objective of this thesis, the simulation of the formation and effect of damage on 3D weaved composites. By combining these models, a general purpose multi-scale framework can be formed that has all the desirable characteristics of a practical solution to component scale analysis:

- A homogenization model to determine effective properties from a known tow architecture
- An equivalent single layer model used for efficiency, to determine gross displacements and low resolution stress data
- A ply resolution model to accurately determine inter-ply stresses
- An explicit damage model to simulate tow pullout and delamination
- A continuum model to simulate in-plane damage and material degradation

This section gives details on the process used to couple the models developed in the previous sections to produce a unified solution.

6.2 Aims

The aim of the method presented here is to couple the models developed in the previous sections to produce a unified multi-scale damage simulation process. The

key to a unified multi-scale simulation is the interaction and passing of data between models that operate on different scales, as illustrated in Figure 6.1.

The method outlines a framework to specify the order in which the models must be considered to ensure information on the material state is passed between the scales at the appropriate point to simulate the growth and effect of damage. The criteria to ensure the convergence of a solution must also be specified.

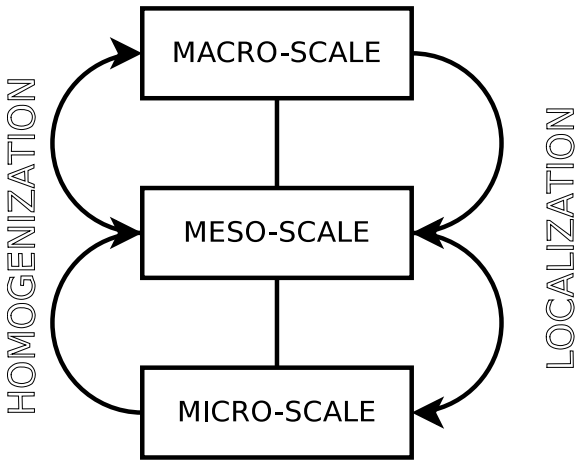

Figure 6.1: **Scale interaction in a multi-scale simulation**

6.3 Method

An outline of the method used is presented in Figure 6.2, and is described in this section.

The method is initiated by defining the micro-scale problem, i.e. the definition of the tow architecture used to produce the 3D weave. An accurate description of the weave is essential in simulating the 3D weaved material and its failure process because of the strong dependence of the macroscopic mechanical properties and the failure mechanisms on the arrangement of tows. The method presented in Chapter 5 is used to homogenize the tow information and produce effective macro-scale properties. At this point in the model, the homogenization can reduce the problem to an equivalent single layer model.

The mechanical properties derived from the homogenization process can the be applied to a component (or macro-) scale structural model, built using the method defined in Chapter 3. This brings the model to a scale that is of practical relevance to a design or analytical engineer since this is typically the scale at which loads are defined. Examples of such loads might be the pressure applied to a wing or aerofoil surface.

The value of this approach is that it enables a quick, low-cost evaluation of displacements, at the expense of accurate ply and tow resolution stress information. Though the stresses in such a model can be crude, they provide a valuable and reliable

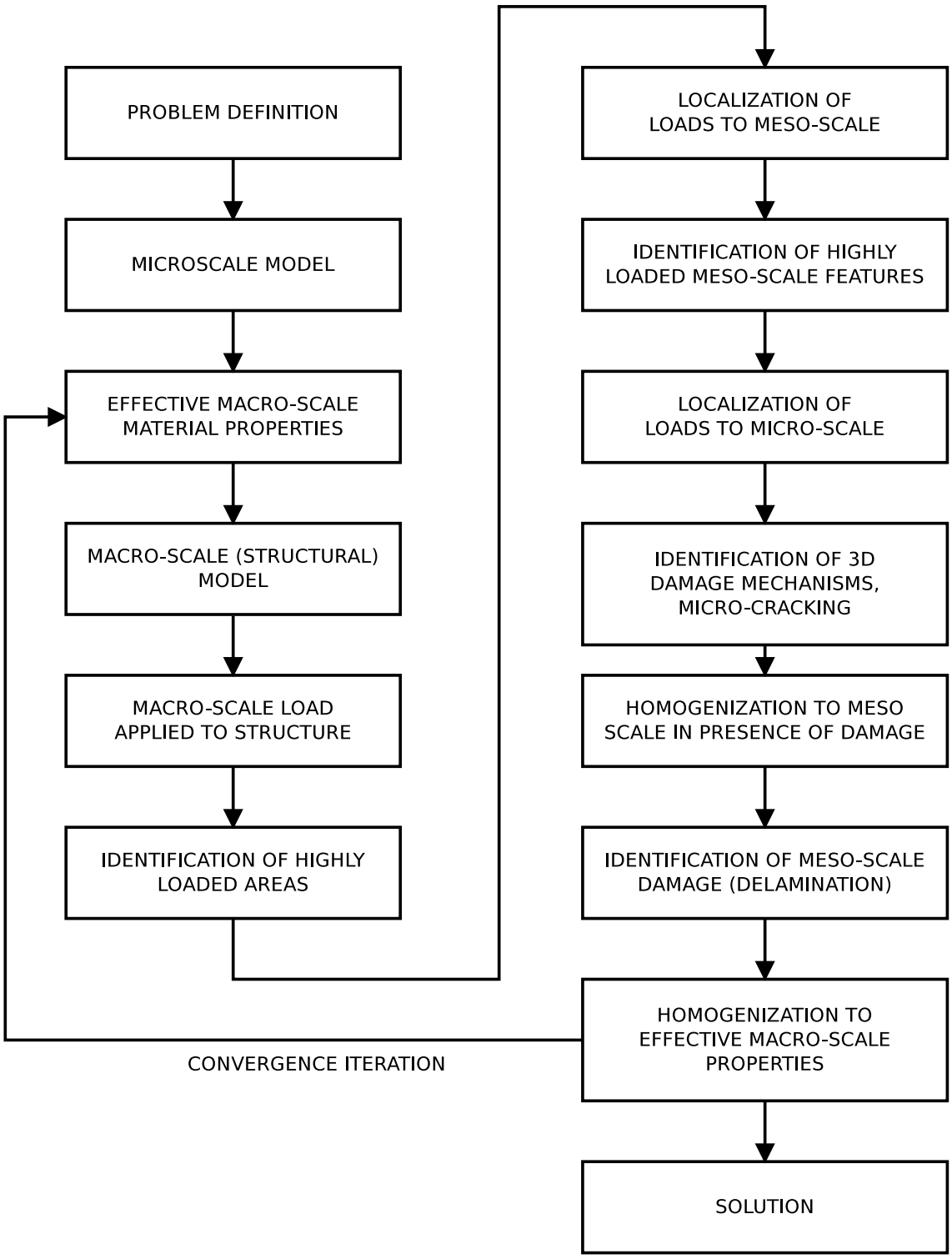

Figure 6.2: **Flow chart of the unified multiscale simulation process**

indicator of the regions in the model that would benefit from closer examination. Using a suitable criterion, e.g. an interactive stress exceedance value, the method in Chapter 3 allows the *in-situ* mesh refinement of a localized region to the meso-scale or a ply-resolution. Limiting the region in which the refinement takes place mimimizes the expense of the calculation.

The ply resolution data is sufficiently accurate to determine regions of both high-stress within the individual plies, and between the plies. In this model, peak values for point stresses in the ply stress state are taken and applied to micro-scale or tow resolution models using the method described in Chapter 5. Analysis using this method is able to localize the stresses to the matrix and the tow regions (accounting for tow geometry), and use appropriate degradation and failure criteria for the constituent components. Failure criteria for the constituents (tows, matrix) can be obtained from mechanical testing, and are low cost and well understood in comparison to composite failure criteria.

Once the degradation of the constituent materials has been determined, the unit cell can be homogenized to determine the effective properties at a larger scale in the presence of ply damage. While this can be done to an effective macro-scale (for use in as an ESL model), it is more useful to homogenize here to the ply resolution. This enables the meso-scale model to evaluate accurate interlaminar stresses. These can be used with the traction-separation simulation model developed in Chapter 4 to determine ply separation and tow pullout. Where significant interlaminar stresses are observed, a discontinuous dispacement field can be superimposed on the component scale model to simulate the load redistribution as a consequence of delamination.

The revised load distribution can be used in a convergence iteration with the micro-scale model to determine the micro-scale damage at a quasi-static state. Once the localized convergence is achieved, the effective macro-scale material properties can be determined using the method presented in Chapter 5, and these properties are used in a convergence iteration until equilibrium is acheived with the macro-scale loads.

6.3.1 Implementation of method

The model described in the previous section has been implemented in MATLAB, using the models developed in the earlier chapters. Some details of the steps required to implement the model are given in Appendix B.

While a complete implementation would allow for a completely automated specification of location of damage, the present implementation requires use of prior knowledge of interlaminar separation location.

6.3.2 Convergence and termination criteria

In the present implementation, a highly stressed region for automated mesh refinement in the two-scale layerwise method is arbitrarily defined as a region in which the any of the direct components of stress exceed 85% of the uniaxial failure load. The uniaxial failure load is a location dependent property, determined from the damage model developed in Chapter 5. The value is chosen to capture a region of peak stress and sufficient surrounding material to transition the refined zone into a less damaged elastic region where the displacements and stresses are of acceptable accuracy in the low resolution models.

Convergence in the continuum damage model is as described in Chapter 5. Convergence between the localized stresses and the traction separation model is conducted until successive iterations show less than 4% difference. This value was chosen from experience, considering a balance between computational cost (i.e. run time) and accuracy.

Convergence between the ply resolution stresses and the macro-scale applied loads was conducted until successive iterations showed less than 1% difference. This value was arbitrarily chosen.

6.4 Summary of method

A unified process covering the methods defined in Chapter 3, Chapter 4 and Chapter 5 is described. The order of models and the passing of data between the models is specified, as well as the requirements for convergence iterations. The values used for convergence criteria in the present implementation have also been specified.

6.5 Results

The method described in this chapter has been implemented in MATLAB, by amalgamating the models developed in Chapter 3, Chapter 4 and Chapter 5. To test the method, a model has been created and run.

The model is of a double cantilever beam, matching the specifications detailed in section 4.6.2. As in the previous models in Chapter 4, the path of the interlaminar separation is specified in the model input–as previously noted, this is a limitation of the current implementation. The tow structure is simulated using the model presented in section 5.6, representing the material produced by Qinetiq.

A contour plot of the through-thickness stresses in the model is shown in Figure 6.3. Figure 6.4 shows the end load versus the displacement at the tip of the DCB. The plot is comparable to Figure 4.9.

Table 6.1 gives the stress state at the centre of the DCB at a location approximately

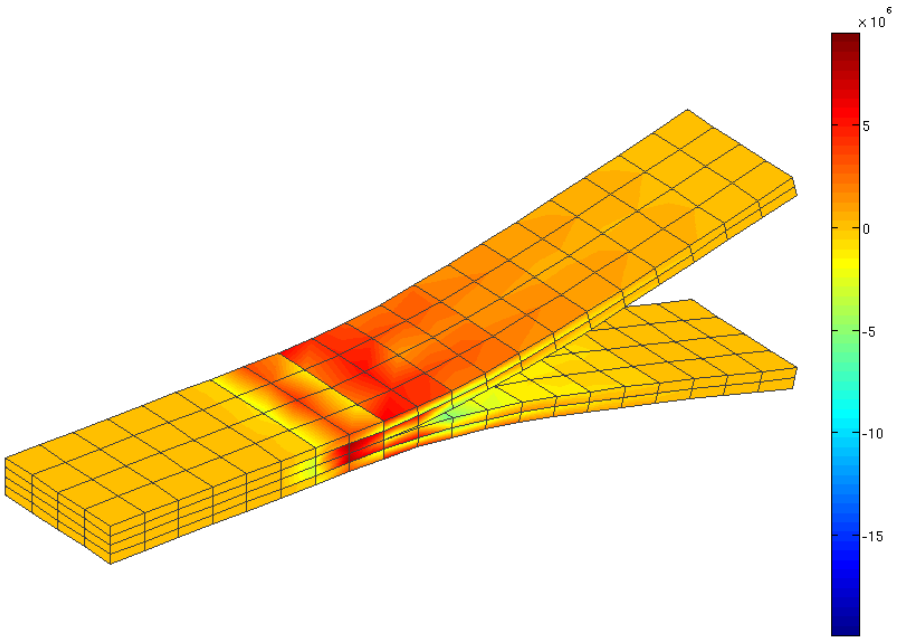

Figure 6.3: **Contour plot of through-thickness stresses (σ_{zz})in double cantilever beam model using unified method** . Contour values are in Pa.

property	value
σ_{xx}/ MPa	76.96
σ_{yy}/ MPa	31.39
σ_{zz}/ MPa	8.55
σ_{xy}/ MPa	9.9
σ_{xz}/ MPa	0
σ_{yz}/ MPa	0.31

Table 6.1: Stress state in the DCB ahead of the delamination front

2 elements from the tip of the delamination during the separation process. (The location is approximate as the cohesive model does not distinctly identify a crack tip.) This location has been chosen for illustration here since it is a location part-way through material degradation.

The point stress state specified in Table 6.1 is expanded into the unit cell model illustrated in Figure 6.5. This model illustrates the stresses in the fibre longitudinal direction. At the selected state, it is found that the most significant damage is found in the warp tows, followed by the binder tows. The damage variable d_{11} is plotted on the binder tow in Figure 6.6. The instantaneous effective material properties at this point of the loading are calculated and given in Table 6.2.

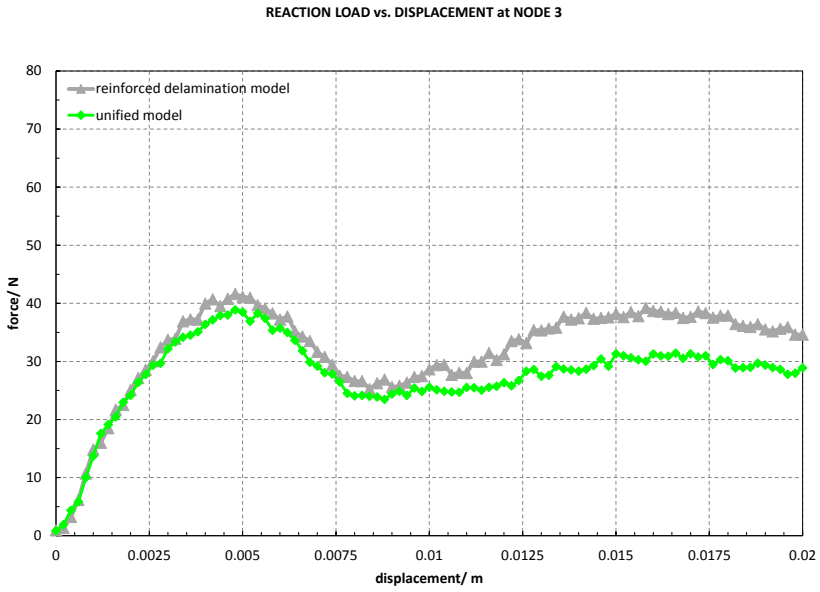

Figure 6.4: **Force vs. displacement data for separation of through-thickness reinforced laminate with continuum in-plane material degradation** . Applied force vs. vertical displacement at end of the double cantilever beam. Also shown are the results from the piecewise linear separation model developed in Chapter 4.

property	original values	degraded values
E_x/ GPa	61.6	54.2
E_y/ GPa	68.4	68.0
E_z/ GPa	12.9	12.5
G_{xy}/ GPa	7.2	3.2
G_{xz}/ GPa	4.5	2.3
G_{yz}/ GPa	4.2	4.2
ν_{xy}	0.048	0.048
ν_{xz}	0.34	0.22
ν_{yz}	0.33	0.32

Table 6.2: Effective degraded material properties ahead of the delamination front

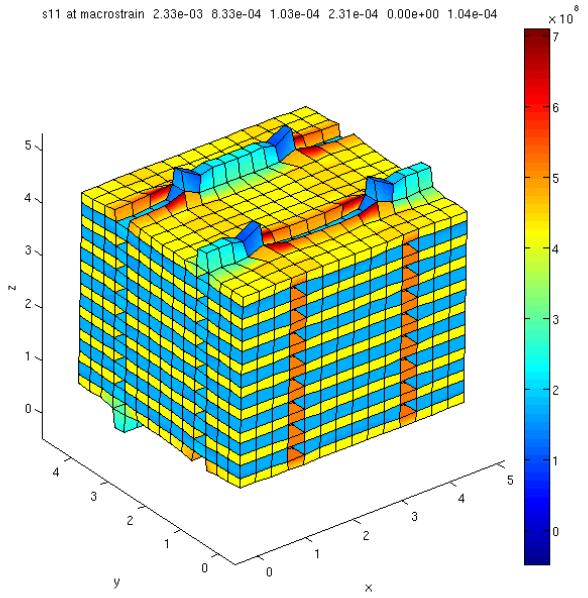

(a) all tows

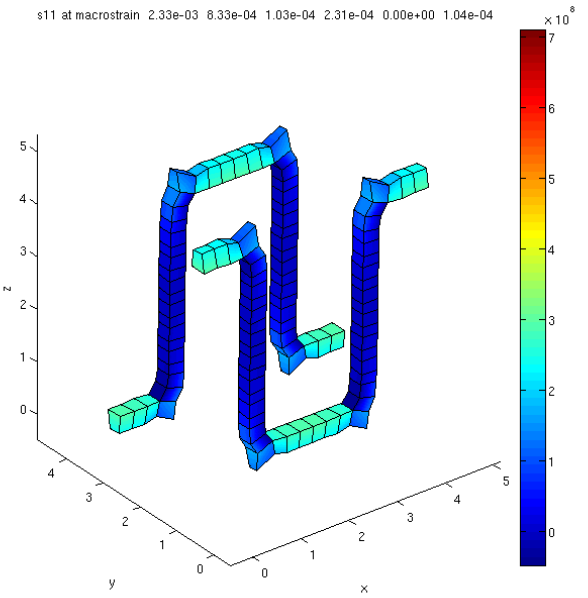

(b) binder tow

Figure 6.5: **Expansion of point stress state into tow architecture from double cantilever beam model** . Stress σ_{11} (longitudinal stress) is plotted in units of Pa. Elements that make up the matrix have been removed for clarity.

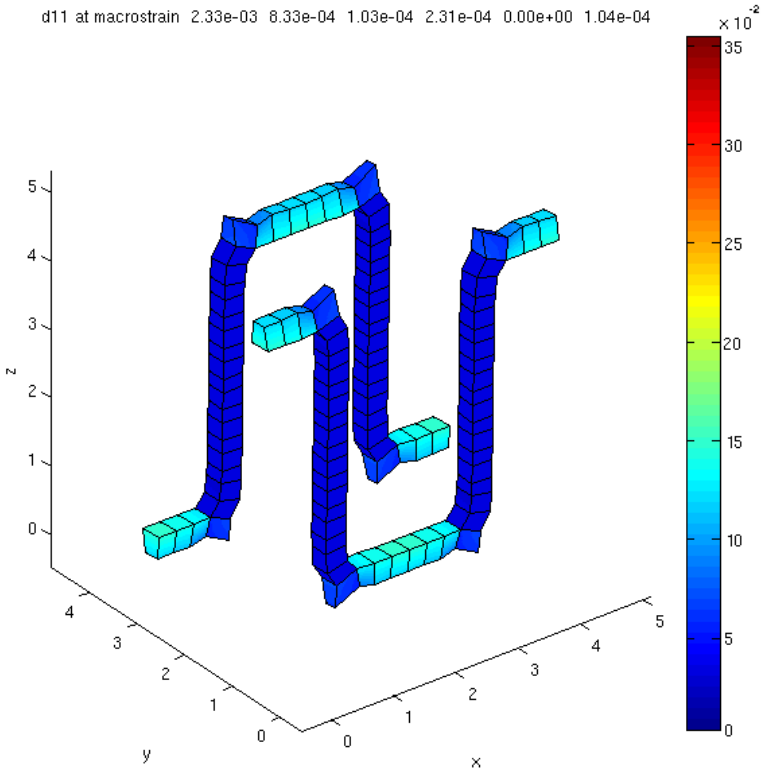

Figure 6.6: **Contour plot of continuum damage parameter d_{11} in the through-thickness binder tow**

6.6 Discussion

Figure 6.4 illustrates the applied load on the 3D weaved double cantilever beam versus the end displacement. The unified model is shown alongside the model developed in Chapter 4 for comparison. The difference between the models is the incorporation of in-plane damage from the micro-model developed in Chapter 5 into this model.

The response of the model is similar to the earlier model. The initial response is almost identical, a result that can be expected prior to damage accumulating in the tows.

The first notable deviation of this model from the previous model is the reduction in peak load. In this model, the peak is approximately 39N, a reduction of ∼5% from the model not considering tow-scale damage. This is likely to be a result of the degraded material ahead of the delamination. The peak load occurs at coinciding displacements between the two models, this is a result of the traction-separation law being defined as a function of the delamination separation.

Following the peak load, the load drops off as the end displacement increases. The rate at which this occurs is equal between the two models. Following this drop-off, the traction separation relationship simulates the transfer of load from the matrix to the through-thicknes reinforcing fibres. Where the model without tow degradation shows a reasonable degree of stiffening and reaches a second peak load almost equal to the initial load, the present model does not exhibit this to the same extent. Some degree of stiffening is apparent, as the load increases corresponding with the cantilever end displacement increaseing, however the response of the material is very flat, indicating a very low level of stiffness. The second peak is only ∼5N greater than the minimum load, after which the cantilever displacement rapidly increases–i.e. the delamination front rapidly progresses to final failure (defined here as complete delamination).

The additional data presented can give some indication of why this behaviour is observed. As expected, the contour plot in Figure 6.3 shows a high stress in the through-thickness direction ahead of the delamination front. Table 6.1 gives the full stress state at such a point, and it is notable that the greatest stresses are the bending stresses in the x-direction.

The process then uses the micro-model to determine how the load is distributed amongst the tows and matrix. Illustrated in Figure 6.5 is the micro-scale stress state. It is evident that the majority of the load is taken by the warp tows (the tows in the x-direction). Also of interest are the binder tows, which illustrate the peak stress they sustain is not in the through-thickness sections as might be expected, but in the in-plane sections as the tow loops over or under the weft tows (6.5(b)). Figure 6.6 confirms that the longitudinal damage parameter d_{11} in the binder tow shows a similar distribution.

At this point in the simulation, the effective material properties of the 3D weave can be recalculated for use in the component scale problem. The properties ahead of

the delamination front are given in Table 6.2. Notable here is the reduction of the longitudinal stiffness E_{xx} by ~10% and the reduction of Poisson ratio ν_{xz}, affecting the redistribution of load from the x-direction to the through-thickness direction. The remainder of the material properties are relatively unaffected.

Examining the results of the model as a whole, we can infer the sequence of events that lead to failure as follows: as the force on the cantilever beam increases, the warp tows take most of the load. They accumulate damage, reducing the effective stiffness of the 3D weaved composite in the x-direction. As it does this, the binder tows take on a larger portion of the load. Once the inter-ply matrix has failed, all the through-thickness load is taken by the binder tows. They continue to do so and accumulate damage, until failure in the 'flat' sections, at which point a second peak load is reached, and the tow begins the pullout phase, after which ultimate failure of the DCB specimen takes place.

Chapter 7

Summary and conclusions

7.1 Introduction

The model presented in Chapter 6 is the culmination of the research work conducted to address the aims presented in Chapter 1. This chapter contains the conclusions from this model and reflections on the research as a whole.

Also presented is a summary of the technical achievements and contributions of this work to the field of computational analysis of composite materials.

7.2 Conclusions on the multi-scale damage model

A model has been developed here to simulate the failure process of a 3D weaved component. It has been demonstrated on an example double cantilever beam component. In the example model, it is demonstrated how the application of loads on the macro- or component-scale are resolved into inter-ply loads and separated further into loads in individual tows in a representative repeating unit cell model. The tow scale loads are used to determine degree of damage in each of the constituents, and the system is re-homogenized so the component-scale response can be determined. The method by which this is done allows determination of exactly which of the constituents fail within the 3D weave, and in what order. This information can allow a 3D weave to be custom tailored for a specific application, helping to design components with a better performance.

The model shows efficiency compared to producing a tow-resolution model for the entire problem domain. Selected regions of a computationally inexpensive ESL model are enhanced where highly stressed regions are determined to resolve accurate interlaminar stresses, and point locations are used to determine tow scale damage and resulting degraded material properties. The current implementation is not completely automated, but it is possible to see how such a framework can be used to fulfil the requirement for a completely automatic tool for accurate, efficient multi-scale

simulation of damage initiation, growth and response of a 3D weaved composite material.

The model can be used at all stages of a design study, including understanding the failure mechanisms of a particular 3D weave architecture, understanding the interaction between a particular weave style and anticipated load conditions to optimize design, and determining the root cause of known failures.

7.3 Summary of thesis

This research set out with the intention of developing a framework of methods to simulate the initiation, growth and effect of damage in 3D weaved composites.

A framework has been presented in this work addressing different parts of the solution, and bringing these parts together to form a unified multi-scale simulation capable of efficiently achieving the original aims of the research.

The resulting model is composed of an extended finite element (XFEM) implementation of a coarse global laminate model with the ability to accurately and efficiently determine interlaminar stresses; an explicit damage model to simulate the delamination and tow pullout failure mechanisms on composite materials; and a tow resolution model using continuum damage in the composite constituents to determine the effective mechanical properties. The framework brings these models together in a way that relevant state information is passed between the model scales in both directions to determine a realistic behaviour.

The two-scale laminate model has been validated against analytical solutions for simple loaded plate systems and has been demonstrated to produce acceptable results at a much smaller computational expense than equivalent full 3D models.

The explicit damage simulation has been validated by comparison of the model output to published data from unidirectional double cantilever beam testing, and has been demonstrated to provide acceptable results. No analogous test data from 3D weaved testing is known to the author and it was not possible to generate the data as part of this research, so the 'pullout' simulation has not been validated, however simulation results have been presented.

The homogenization and continuum damage simulation has been validated by comparison to test data generated by monotonic loading of a 3D weaved composite in tension, compression and shear, and has been demonstrated to provide an acceptable determination of the macroscopic material properties throughout the degradation process.

7.3.1 Summary of technical achievements and novel contribution

The technical achievements and novel contributions of this work are as follows:

- The use of layerwise laminate models to simulate 3D weaved tow architecture is a novel approach in using the foundations of well established simple models to model a geometry that is far more complex than the laminates for which the models were originally developed.

- The use of extended finite element methods to apply extrinsic enrichment to the layerwise method to allow the superposition of any number of displacement field functions, and in any localized area (both in-plane and through-thickness) to a model. This approach has been published in:

  - S. L. Angioni, A. Visrolia, and M. Meo. A hierarchical multiple plate models theory for laminated composites including delamination and geometrical nonlinear effects. *Composite Structures*, 93:780–791, 2011. doi:10.1016/-j.compstruct.2010.08.003

  - S. L. Angioni, A. Visrolia, and M. Meo. Combining X-FEM and a multi-level mesh superposition method for the analysis of thick composite structures. *Composites: Part B*, 43(12):559–568, March 2012. doi:10.1016/-j.compositesb.2011.07.005

- The use of cohesive traction-separation models to simulate the degradation of a reinforced interface between plies, including simulation of the effect of binder tow pullout—a damage mechanism characteristic of the failure of 3D weaved composites—is novel.

- The coupling of a continuum damage model to a unit cell model analysed using the asymptotic expansion homogenization method to allow localization of loads to determine damage in composite constituents, and determination of the effect of local damage to the effective mechanical properties. This model has been published in:

  - A. Visrolia and M. Meo. Multiscale damage modelling of 3D weave composite by asymptotic homogenisation. *Composite Structures*, 95:101–113, 2013. doi:10.1016/j.compstruct.2012.07.018

Appendices

Appendix A

Further examples of the two-scale layerwise method

A.1 Introduction

To further demonstrate the capability of the two-scale layerwise method developed in Chapter 3, the results of the analyses of an unbalanced and unsymmetric laminate are presented here. This case is chosen to demonstrate the capability of the method to reproduce the coupling effects between in-plane deformation and out-of-plane bending.

A.2 Model details

The laminate modelled here is a four-layered laminate of ply orientations 0/45/30/90. The dimensions of the laminate are 0.1×0.1m, and the plies are each of 0.001m thickness.

The material properties are:

$$E_1 = 150\text{GPa} \qquad E_2 = E_3 = 11\text{GPa}$$
$$G_{12} = G_{13} = 6\text{GPa} \qquad G_{23} = 3.7\text{GPa}$$
$$\nu_{12} = \nu_{13} = 0.25 \qquad \nu_{23} = 0.45$$

Analyses of this laminate are conducted with two different load cases:

load case 1 : a uniform load of 1MPa is applied on one edge, while the laminate is clamped at the opposite edge.

load case 2 : the laminate is applied with a uniform transverse load of 1MPa while the edges are all clamped.

The laminate plate is meshed with 50×50 elements in-plane with a single linear out-of-plane expansion. Local enrichment of the out-of-plane expansion is conducted with the use of a four-part linear piecewise function in the regions 0.004m (i.e. 2 elements) from the edges and in the central 0.008m region (i.e. 4×4 elements). For comparison, the plate is also simulated using a full 3D finite element analysis with $50 \times 50 \times 4$ linear brick elements.

A.3 Results

Figure A.1 and Figure A.2 illustrate the deformation shape, stresses and through-thickness stress profiles for load cases 1 and 2. The through-thickness stress profiles are shown for the full 3D solution, and for the locally enriched model developed in this thesis.

A.4 Discussion

The computational cost of the models compared to the use of equivalent single layer models is summarized in Table A.1.

model	degrees-of-freedom	change from ESL
equivalent single layer	**5202**	
locally enriched model	**7727**	+48%
full 3D solid element	**13005**	+148%

Table A.1: Degrees of freedom, representing computational cost of different models

The through-thickness stress profiles illustrate that using the model developed here, and with the selected level of enrichment, the stresses are determined to a level of accuracy that is comparable to a computationally expensive full 3D solution – in this case, stresses are within 1%. This is achieved using a model with only approximately 60% of the number of degrees-of-freedom of the more expensive model. The example chosen here is an unsymmetric and unbalanced laminate for which the assumptions of the equivalent single layer (ESL) model would show significant deviation from the actual values, thus demonstrating the value of this model.

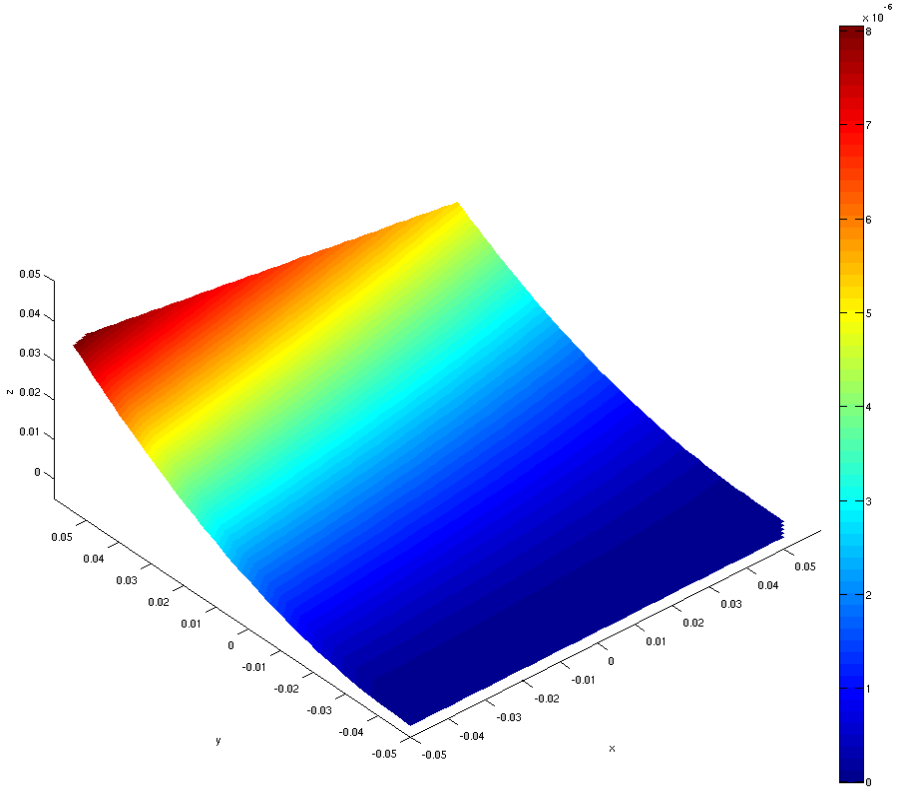

(a) Contour plot of transverse displacement w.

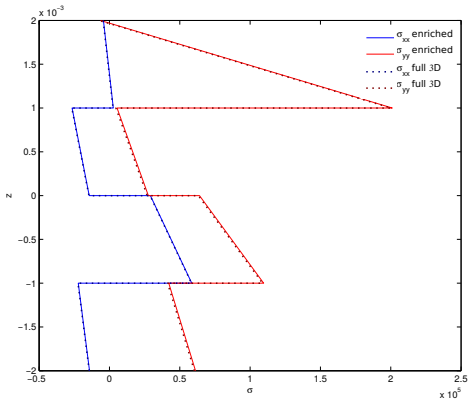

(b) In-plane stresses through the thickness at centre of plate

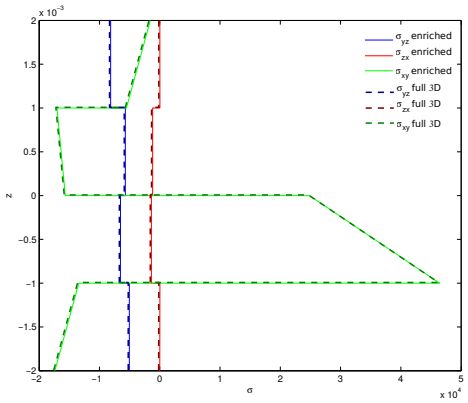

(c) shear stresses through the thickness at centre of plate

Figure A.1: **Load case 1** – in-plane load

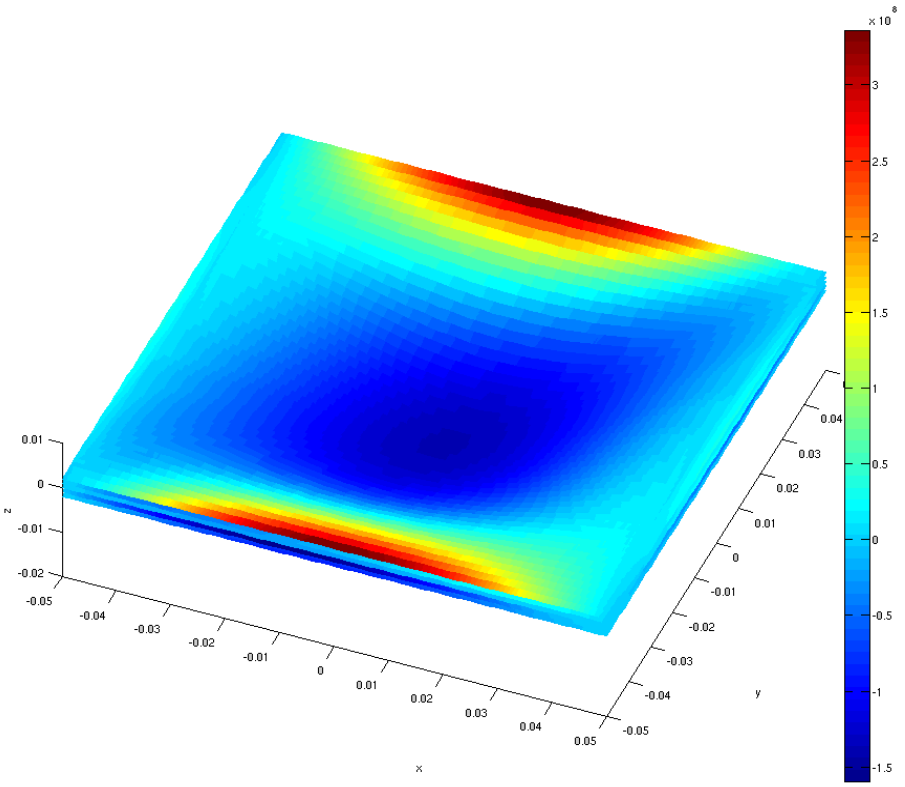

(a) Contour plot of in-plane stress σ_{yy}

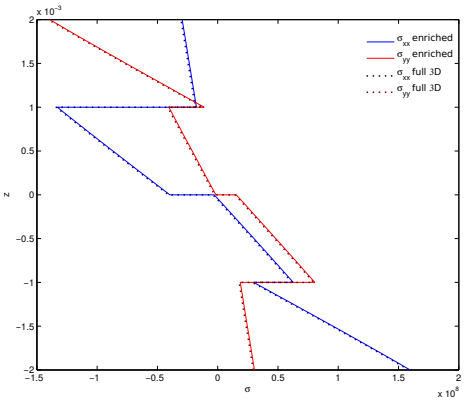

(b) In-plane direct stresses at centre of plate

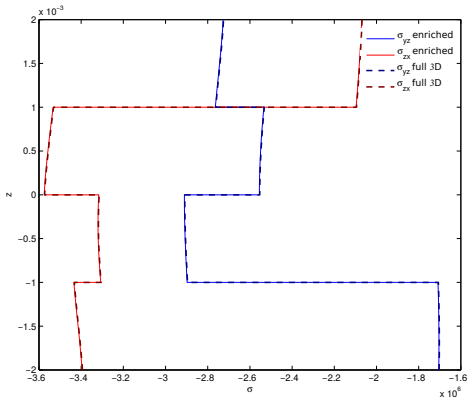

(c) Shear stresses σ_{yz} and σ_{zx} at centre of plate

Figure A.2: **Load case 2** – transverse load

Appendix B

Outline of the implementation of the unified method

B.1 Introduction

This appendix contains a brief summary of the implementation of the model described in this work. The model remains as described in the body of the thesis.

In practice, this model has been implemented in MATLAB, but the description here is given in terms to allow re-implementation within any computational environment.

B.2 Computational process

The overall process is as decribed in Figure 6.2. The following sections detail parts of Figure 6.2 by defining inputs, details of the process, and the resulting outputs.

B.2.1 Micro-scale model: determining effective macro-scale material properties

Inputs:

Repeating unit cell mesh A discretized description of the weave architecture within the composite. In the implementation produced here, this is produced by the software TexGen [135], and includes material orientation information for each of the elements.

Material properties Elastic constants for each of the constituents (the matrix and the yarns).

Process

1. The mesh is read from the TexGen file.

2. The material properties are read from a separate text file.

3. Looping over the elements in the mesh, the material stiffness matrices C are formed. For elements representing the orthotropic material properties of the yarns, the element stiffness matrices are rotated from the material coordinate system to a consistent global coordinate system.

4. Element stiffness and force matrices are formed using Equation 5.29 and Equation 5.30. Integration is conducted using Gaussian quadrature. Note, a key difference between the **F** matrix formed here and the equivalent vector formed in traditional structural finite element analysis is that **F** is a six-column matrix representing unit loading in each of the 6 (normal and shear) load directions.

5. The global stiffness and force matrices are assembled. This is done by mapping the element local nodes onto a global node list. Where a node is shared by multiple elements, the terms from the individual element stiffness and force matrices are summed.

6. Application of periodic boundary conditions is performed by identifying pairs of nodes on opposite faces, and summing the stiffness and force terms, and subsequently eliminating one set of degrees-of-freedom.

7. A single node at the corner of the mesh is applied constraints on all its degrees-of-freedom by replacing its terms in the global stiffness matrix by corresponding terms in an identity matrix of equal size, and the terms in the force matrix by zero. This prevents rigid body motion.

8. The system Equation 5.28 can then be solved. This is a straightforward, single step solve and can be performed with e.g. MATLAB's `mldivide()` function. This determines the correctors **X**.

9. The effective homogenized RUC stiffness matrix $\bar{C}$ is given by Equation 5.31. This requires differentiation of the corrector with respect to the micro-coordinate system, and is done using the shape function derivative matrix **B** at the points required by the Gaussian quadrature to conduct the volume integration.

Outputs:

Homogenized stiffness matrix for use in the meso/macro-scale model.

Micro scale corrector X as described in Equation 5.28.

B.2.2 Macro-scale structural model and identification of highly loaded areas

Inputs:

Homogenized stiffness matrix from the homogenization of the repeating unit cell.

2D mesh A discretization of the global model. This may be a series of overlapping meshes in regions where extra detail is required.

Through-thickness mesh A one-dimensional discretization of each of the 2D meshes. These define the particular Lagrangian functions used to determine the interpolation of the displacements in the z-direction for a given 2D region.

Loads applied to the global model (either displacement or traction boundary conditions).

Process

1. The model inputs are read from a custom text file format, and from the outputs of the previous stage.

2. Looping over the elements in each of the 2D meshes, the A, $\bar{A}$, $\bar{\bar{A}}$, B, $\bar{B}$ and D terms from Equation 3.21 are computed. The element stiffness matrix $\bar{c}$ is as derived from the micro-scale simulation in the previous stage. The integration in the z-direction is conducted by Gaussian quadrature of the Lagrange shape functions Equation 3.8.

3. The element stiffness matrices $\mathbf{k}$ are constructed. The individual terms k_{ij} are given by collecting the coefficients of the $\partial U_i / \partial x_j$ terms in the virtual work statement Equation 3.16. The A, $\bar{A}$, $\bar{\bar{A}}$, B, $\bar{B}$ and D terms computed in item 2 assist with this. Note, the stiffness matrix is a function of the current displacement vector, which at the beginning of the analysis will be zero.

4. The element tangent stiffness matrices are also calculated as $\partial k_i / \partial x_j$

5. The element force vector $\mathbf{f}$ are constructed as any standard structural finite element analysis.

6. The element matrices and vectors are assembled into global forms. This process is identical to that described in the micro-scale analysis stage, noting that any superimposed displacement fields are given their own independent degrees-of-freedom.

7. Boundary conditions are applied. In addition to typical finite element boundary conditions, it must be ensured that the superimposed displacement fields have a

set of common (or tied) degrees-of-freedom to form a single contiguous problem mesh. Degrees-of-freedom are tied as the periodic boundary conditions were applied in the micro-scale problem.

8. The model can be solved. As a non-linear problem, the solution cannot be computed in a single step. Prior to delamination, a process such as Newton's (or the Newton-Raphson) method can be used, which requires both the stiffness and tangent stiffness matrices to be formed at the beginning of the analysis and at every estimate of the solution during the iteration to convergence.

9. Post-processing of the converged solution is done by calculating the strains from the individual nodal displacement vectors using the shape function derivative matrix **B**. The strains are then used to determine the stresses, and areas of through-thickness stresses exceeding critical values are noted for delamination.

Outputs:

Displacements A vector of the nodal displacements as a function of position within the global model.

Delamination locations A decription of the locations in the model to position a delamination displacement field.

B.2.3 Macro-scale model and simulation of delamination

Inputs:

Displacements From the macro-scale model

Cohesive coefficients Coefficients to describe the cohesive law to use to model the separation at delamination.

Process

1. The identified delamination sites from the previous stage represent an additional displacement field. In common with the previous stage, the A, $\bar{A}$, $\bar{\bar{A}}$, B, $\bar{B}$ and D terms will be computed, for the delamination field and for the interaction of the delamination field with each of the continuous displacement fields.

2. The difference from the previous stage is that the through-thickness piecewise integration will be conducted assuming the displacement conforms to the discontinuous shape functions, Equation 4.10, rather than the Lagrange interpolations, Equation 3.8. Since the integration is piecewise with boundaries between the plies, Gaussian quadrature can be used for each of the 'pieces' (the through-thickness discretizations).

3. The extra stiffness terms are calculated. These are the terms K^{DD}, $K^{D\alpha}$ and $K^{\alpha D}$ from Equation 3.23, where D represents the present delamination field, and α each of the pre-existing displacement fields (which may themselves be delamination fields in the case of overlapping delaminations).

4. The extra stiffness terms are appended to the existing stiffness matrix, with each displacement field adding degrees-of-freedom representing displacements at the top and bottom of the laminate at each location in-plane.

5. The tangent stiffness matrix is re-formed, using the same process as before.

6. Boundary conditions are applied to the present delamination field. The only applicable boundary condition is to tie one side of the delamination to an existing displacement field. This is done in the same manner as the periodic boundary conditions were applied in the micro-scale problem, and will eliminate half the degrees-of-freedom in the newly added delamination field.

7. The model can be solved. In common with the previous stage, the dependence of the stiffness matrix on the current displacement means the system is non-linear and cannot be solved in a single step. Newton's method has convergence problems when the gradient (i.e. the tangent stiffness matrix) turns close to zero or negative as it does with delamination, so is not a suitable method to solve the problem. The method employed here is an implementation of Riks' arc-length algorithm (also known as the modified Riks method) which can deal with this class of problem.

8. Post-processing is done as in the previous stage. Instead of identification of delamination sites, all highly loaded locations should be identified as potential sites for micro-scale damage.

Outputs:

Displacements at equilibrium, in the presence of a partial or full delamination.

Damage sites indicating location where micro-scale damage may be present, and the point strain state at these locations.

B.2.4 Localization of loads to micro-scale and simulating the effect of micro-cracking

Inputs:

Macro-scale strains Point strain states from the macro-scale models.

Repeating unit cell corrector from the previous iteration of the micro-scale homogenization problem.

Threshold and critical damage energy release rates to determine degree of mateial degradation.

Process

1. For each of the highly loaded locations from the macro-scale problem, perform localization of the point strain state using Equation 5.32. This involves differentiating the corrector X using the shape function derivatives. This determines the stresses in each of the constituents of the RUC (i.e. the tows and the matrix).

2. When the stresses are known, the damage energy release rate Y can be calculated from Equation 5.39 using the current damaged compliance matrix $\hat{\mathbf{S}}$. Prior to damage initiation, this is the same as the initial compliance matrix.

3. The damage energy release rate is compared to the threshold and critical values to determine the damage parameter d using Equation 5.41. From this, the revised compliance matrix for each element, Equation 5.36 can be determined.

4. Once the revised compliance (and hence stiffness) matrix is known, the correctors and the effective homogenized properties for the RUC can be determined as before, but this time in the presence of micro-scale damage. These material properties will go on to be used in subsequent iterations of the model as the degree of damage increases.

Outputs:

Homogenized stiffness matrix A revised homogenized stiffness matrix in the presence of micro-scale damage.

B.2.5 Convergence iterations

Inputs:

Homogenized stiffness matrix The revised homogenized stiffness matrix from the previous iteration of the micro-scale model

Process

The process as described in the previous stages is repeated in a convergence loop. The loop convergence criteria is a minimal change in the material stiffness. When no (or very little) change in the stiffness is occurring, the steps within the iteration will solve

the displacements and stresses under the applied boundary conditions, and no further damage must be occurring.

Outputs:

Global model displacements at equilibrium The final displacements will be at equilibrium with the applied loads in the presence of all the damage that would accumulate upon application of the load.

Residual stiffness The resulting degraded material properties are also available to allow further analysis if required.

References

[1] Hexcel aerospace selector guide.

[2] S. L. Angioni, A. Visrolia, and M. Meo. A hierarchical multiple plate models theory for laminated composites including delamination and geometrical nonlinear effects. *Composite Structures*, 93: 780–791, 2011. doi:10.1016/j.compstruct.2010.08.003.

[3] S. L. Angioni, A. Visrolia, and M. Meo. Combining X-FEM and a multilevel mesh superposition method for the analysis of thick composite structures. *Composites: Part B*, 43(12):559–568, March 2012. doi:10.1016/j.compositesb.2011.07.005.

[4] A. Visrolia and M. Meo. Multiscale damage modelling of 3D weave composite by asymptotic homogenisation. *Composite Structures*, 95:101–113, 2013. doi:10.1016/j.compstruct.2012.07.018.

[5] G. Staab. *Laminar Composites*. Butterworth Heinemann, June 1999. ISBN 978-075067124-8.

[6] B. N. Cox and G. Flanagan. Handbook of analytical methods for textile composites. Technical Report NASA/CR-4750, NASA, Langley Research Center, March 1997. URL `http://ntrs.nasa.gov/archive/nasa/casi.ntrs.nasa.gov/19970017583_1997024417.pdf`.

[7] L. Tong, A. P. Mouritz, and M. K. Bannister. *3D Fibre Reinforced Polymer Composites*. Elsevier, November 2002. ISBN 978-008043938-9.

[8] B. N. Cox, M. S. Dadkhah, W. L. Morris, and J. G. Flintoff. Failure mechanisms of 3D woven composites in tension, compression, and bending. *Acta Metallurgica et Materialia*, 42(12): 3967–3984, 1994.

[9] A. P. Mouritz, M. K. Bannister, P. J. Falzon, and K. H. Leong. Review of applications for advanced three-dimensional fibre textile composites. *Composites: Part A*, 30(12):1445–1461, December 1999. doi:10.1016/S1359-835X(99)00034-2.

[10] R. McIlhagger, J. P. Quinn, A. T. McIlhagger, S. Wilson, D. Simpson, and W. Wenger. The influence of binder tow density on the mechanical properties of spatially reinforced composites. Part 1—Impact resistance. *Composites: Part A*, 38:795–801, 2007. doi:10.1016/j.compositesa.2006.09.002.

[11] R. McIlhagger, J. P. Quinn, A. T. McIlhagger, S. Wilson, D. Simpson, and W. Wenger. The influence of binder tow density on the mechanical properties of spatially reinforced composites. Part 2—Mechanical properties. *Composites: Part A*, 39:334–341, 2008. doi:10.1016/j.compositesa.2007.10.006.

[12] O. C. Zienkiewicz, R. L. Taylor, and J. Z. Zhu. *The Finite Element Method: Its Basis and Fundamentals*. Elsevier Butterworth-Heinemann, 6th edition, 2005. ISBN 978-075066320-5.

[13] M.-J. Pindera, H. Khatam, A. S. Drago, and Y. Bansal. Micromechanics of spatially uniform heterogeneous media: A critical review and emerging approaches. *Composites: Part B*, 40: 349–378, 2009. doi:10.1016/j.compositesb.2009.03.007.

[14] J. Byström, N. Jekabsons, and J. Varna. An evaluation of different models for prediction of elastic properties of woven composites. *Composites: Part B*, 31:7–20, 2000. doi:10.1016/S1359-8368(99)00061-X.

[15] P. Tan, L. Tong, and G. P. Steven. Modelling for predicting the mechanical properties of textile composites—A review. *Composites: Part A*, 28(11):903–922, 1997. ISSN 1359-835X. doi:10.1016/S1359-835X(97)00069-9.

[16] P. Tan, L. Tong, and G. P. Steven. A three-dimensional modelling technique for predicting the linear elastic property of opened-packing woven fabric unit cells. *Composite Structures*, 38(1-4): 261–271, May–Aug 1997. doi:10.1016/S0263-8223(97)00061-5.

[17] P. Tan, L. Tong, and G. P. Steven. Models for predicting thermomechanical properties of three-dimensional orthogonal woven composites. *Journal of Reinforced Plastics and Composites*, 18(2): 151–185, 1999. doi:10.1177/073168449901800204.

[18] B. N. Cox and M. S. Dadkhah. The macroscopic elasticity of 3D woven composites. *Journal of Composite Materials*, 29(6):785–819, 1995. doi:10.1177/002199839502900606.

[19] Z. J. Wu, D. Brown, and J. M. Davies. An analytical modelling technique for predicting the stiffness of 3-D orthotropic laminated fabric composites. *Composite Structures*, 56:407–412, 2002. doi:10.1016/S0263-8223(02)00024-7.

[20] B. N. Cox, M. S. Dadkhah, R. V. Inman, W. L. Morris, and J. Zupon. Mechanisms of compressive failure in 3D composites. *Acta Metallurgica et Materialia*, 40(12):3285–3298, 1992.

[21] B. N. Cox. Delamination and buckling in 3D composites. *Journal of Composite Materials*, 28(12): 1114–1126, 1994. doi:10.1177/002199839402801203.

[22] B. N. Cox, M. S. Dadkhah, and W. L. Morris. On the tensile failure of 3D woven composites. *Composites: Part A*, 27A:447–458, 1996. doi:10.1016/1359-835X(95)00053-5.

[23] P. J. Callus, A. P. Mouritz, M. K. Bannister, and K. H. Leong. Tensile properties and failure mechanisms of 3D woven GRP composites. *Composites: Part A*, 30(11):1277–1287, November 1999. doi:10.1016/S1359-835X(99)00033-0.

[24] J. P. Quinn, A. T. McIlhagger, and R. McIlhagger. Examination of the failure of 3D woven composites. *Composites: Part A*, 39(2):273–283, February 2008. doi:10.1016/j.compositesa.2007.10.012.

[25] A. Puck and H. Schürmann. Failure analysis of FRP laminates by means of physically based phenomenological models. *Composites Science and Technology*, 58(7):1045–1067, 1998. doi:10.1016/S0266-3538(96)00140-6.

[26] R. G. Cuntze and A. Freund. The predictive capability of failure mode concept-based strength criteria for multidirectional laminates. *Composites Science and Technology*, 64:343–377, 2004. doi:10.1016/S0266-3538(03)00218-5.

[27] M. J. Hinton, A. S. Kaddour, and P. D. Soden, editors. *Failure criteria in fibre reinforced polymer composites: The world-wide failure exercise*. Elsevier Ltd., 2004. ISBN 978-008044475-8. doi:10.1016/B978-008044475-8/50002-0.

[28] P. D. Soden, M. J. Hinton, and A. S. Kaddour. A comparison of the predictive capabilities of current failure theories for composite laminates. *Composites Science and Technology*, 58(7): 1225–1254, July 1998. doi:10.1016/S0266-3538(98)00077-3.

[29] M. J. Hinton, A. S. Kaddour, and P. D. Soden. A comparison of the predictive capabilities of current failure theories for composite laminates, judged against experimental evidence. *Composites Science and Technology*, 62(12-13):1725–1797, Sep-Oct 2002. doi:10.1016/S0266-3538(02)00125-2.

[30] A. S. Kaddour, M. J. Hinton, and P. D. Soden. A comparison of the predictive capabilities of current failure theories for composite laminates: additional contributions. *Composites Science and Technology*, 64(3-4):449–476, March 2004. doi:10.1016/S0266-3538(03)00226-4.

[31] A. C. Orifici, I. Herszberg, and R. S. Thomson. Review of methodologies for composite material modelling incorporating failure. *Composite Structures*, 86:194–210, 2008. doi:10.1016/j.compstruct.2008.03.007.

[32] L. Onal and S. Adanur. Modeling of elastic, thermal, and strength/failure analysis of two-dimensional woven composites—A review. *Applied Mechanics Reviews*, 60(1):37–39, January 2007. doi:10.1115/1.2375143.

[33] U. Icardi, S. Locatto, and A. Longo. Assessment of recent theories for predicting failure of composite laminates. *Applied Mechanics Reviews*, 60(2):76–86, March 2007. doi:10.1115/1.2515639.

[34] I. M. Daniel. Failure of composite materials. *Strain*, 43(1):4–12, 2007. doi:10.1111/j.1475-1305.2007.00302.x.

[35] C. G. Dávila, P. P. Camanho, and C. A. Rose. Failure criteria for FRP laminates. *Journal of Composite Materials*, 39(4):323–345, 2005. doi:10.1177/0021998305046452.

[36] S. T. Pinho, C. G. Dávila, P. P. Camanho, L. Iannucci, and P. Robinson. Failure models and criteria for FRP under in-plane or three-dimensional stress states including shear non-linearity. Technical Report NASA/TM-2005-213530, NASA, Langley Research Center, February 2005. URL `http://ntrs.nasa.gov/archive/nasa/casi.ntrs.nasa.gov/20050110223_2005093402.pdf`.

[37] F. P. van der Meer and L. J. Sluys. Continuum models for the analysis of progressive failure in composite laminates. *Journal of Composite Materials*, 43(20):2131–2156, 2009. doi:10.1177/0021998309343054.

[38] Y. S. N. Reddy, C. M. Dakshina Moorthy, and J. N. Reddy. Non-linear progressive failure analysis of laminated composite plates. *International Journal of Non-Linear Mechanics*, 30(5):629–649, 1995. doi:10.1016/0020-7462(94)00041-8.

[39] J. J. C. Remmers, R. de Borst, and A. Needleman. A cohesive segments method for the simulation of crack growth. *Computational Mechanics*, 31:69–77, 2003. doi:10.1007/s00466-002-0394-z.

[40] D. H. Robbins, Jr. and J. N. Reddy. Adaptive hierarchical kinematics in modeling progressive damage and global failure in fiber-reinforces composite laminates. *Journal of Composite Materials*, 42(2):143–172, 2008. doi:10.1177/0021998307086210.

[41] N. F. Knight, Jr. User-defined material model for progressive failure analysis. Technical Report NASA/CR-2006-214526, NASA, Langley Research Center, December 2006. URL `http://ntrs.nasa.gov/archive/nasa/casi.ntrs.nasa.gov/20070000534_2006259424.pdf`.

[42] J. Chen, M. A. Crisfield, A. J. Kinloch, E. P. Busso, F. L. Matthews, and Y. Qiu. Predicting progressive delamination of composite material specimens via interface elements. *Mechanics of Advanced Materials and Structures*, 6(4):301–317, January 1999. doi:10.1080/107594199305476.

[43] T. E. Tay, G. Liu, V. B. C. Tan, X. S. Sun, and D. C. Pham. Progressive failure analysis of composites. *Journal of Composite Materials*, 42(18):1921–1966, 2008. doi:10.1177/0021998308093912.

[44] X. S. Sun, V. B. C. Tan, G. Liu, and T. E. Tay. An enriched element-failure method (REFM) for delamination analysis of composite structures. *International Journal for Numerical Methods in Engineering*, 79:639–666, 2009. doi:10.1002/nme.2567.

[45] B. A. Bednarcyk and S. M. Arnold. A framework for performing multiscale stochastic progressive failure analysis of composite structures. In ABAQUS *Users' Conference*, 2006. URL `http://ntrs.nasa.gov/archive/nasa/casi.ntrs.nasa.gov/20070019696_2007019096.pdf`.

[46] I. Lapczyk and J. A. Hurtado. Progressive damage modeling in fiber-reinforced materials. *Composites: Part A*, 38:2333–2341, 2007. doi:10.1016/j.compositesa.2007.01.017.

[47] C. T. Key, S. C. Schumacher, and A. C. Hansen. Progressive failure modeling of woven fabric composite materials using multicontinuum theory. *Composites: Part B*, 38:247–257, 2007. doi:10.1016/j.compositesb.2006.03.006.

[48] E. A. D. Lamers. *Shape distortions in fabric reinforced composite products due to processing induced fibre reorientation*. PhD thesis, University of Twente, Netherlands, April 2004. URL `http://doc.utwente.nl/41422/`.

[49] D. H. Allen. Homogenization principles and their application to continuum damage mechanics. *Composites Science and Technology*, 61:2223–2230, 2001. doi:10.1016/S0266-3538(01)00116-6.

[50] J. Fish and S. Markolefas. The s-version of the finite element method for multilayer laminates. *International Journal for Numerical Methods in Engineering*, 33:1081–1105, 1992. doi:10.1002/nme.1620330512.

[51] J. W. Park, J. W. Hwang, and Y. H. Kim. Efficient finite element analysis using mesh superposition technique. *Finite elements in Analysis and Design*, 39:619–638, 2003. doi:10.1016/S0168-874X(02)00131-2.

[52] J. Fish and R. Guttal. The s-version of the finite element method for laminated composites. *International Journal for Numerical Methods in Engineering*, 39:3641–3662, 1996. doi:10.1002/(SICI)1097-0207(19961115)39:21<3641::AID-NME17>3.0.CO;2-P.

[53] D. H. Robbins, Jr. and J. N. Reddy. Variable kinematic modelling of laminated composite plates. *International Journal for Numerical Methods in Engineering*, 39:2283–2317, 1996. doi:10.1002/(SICI)1097-0207(19960715)39:13<2283::AID-NME956>3.0.CO;2-M.

[54] E. J. Barbero. *On a generalized laminate theory with application to bending, vibration, and delamination buckling in composite laminates*. PhD thesis, Faculty of the Virginia Polytechnic Institute and State University, 1989.

[55] E. J. Barbero and J. N. Reddy. Modeling of delamination in composite laminates using a layer-wise plate theory. *International Journal of Solids and Structures*, 28(3):373–388, 1991. doi:10.1016/0020-7683(91)90200-Y.

[56] E. J. Barbero and J. N. Reddy. Nonlinear analysis of composite laminates using a generalized laminated plate theory. *AIAA Journal*, 28(11):1987–1994, November 1990. doi:10.2514/3.10509.

[57] R. L. Actis, B. A. Szabo, and C. Schwab. Hierarchic models for laminated plates and shells. *Computer Methods in Applied Mechanics and Engineering*, 172:79–107, 1999. doi:10.1016/S0045-7825(98)00226-6.

[58] X. Li and D. Liu. Generalized laminate theories based on double superposition hypothesis. *International Journal for Numerical Methods in Engineering*, 40:1197–1212, 1997. doi:10.1002/(SICI)1097-0207(19970415)40:7<1197::AID-NME109>3.0.CO;2-B.

[59] T. I. Zohdi, J. T. Oden, and G. J. Rodin. Hierarchical modeling of heterogeneous bodies. *Computer Methods in Applied Mechanics and Engineering*, 138:273–298, 1996. doi:10.1016/S0045-7825(96)01106-1.

[60] Z. Yue. *Adaptive superposition of finite element meshed in linear and nonlinear dynamic analysis*. PhD thesis, University of Maryland, 2005. URL `http://hdl.handle.net/1903/3181`.

[61] Z. Yue and D. H. Robbins, Jr. Adaptive superposition of finite element meshes in non-linear transient solid mechanics problems. *International Journal for Numerical Methods in Engineering*, 72:1063–1094, 2007. doi:10.1002/nme.2067.

[62] J. Fish and K. Shek. Multiscale analysis of composite materials and structures. *Composites Science and Technology*, pages 2547–2556, 2000. doi:10.1016/S0266-3538(00)00048-8.

[63] N. Takano, Y. Uetsuji, Y. Kashiwagi, and M. Zako. Hierarchical modelling of textile composite materials and structures by the homogenization method. *Modelling and Simulation in Materials Science and Engineering*, 7:207–231, 1999. doi:10.1088/0965-0393/7/2/006.

[64] N. Takano, M. Zako, and M. Ishizono. Multi-scale computational method for elastic bodies with global and local heterogeneity. *Journal of Computer-Aided Materials Design*, 7:111–132, 2000. doi:10.1023/A:1026558222392.

[65] B. N. Cox, W. C. Carter, and N. A. Fleck. A binary model of textile composites—I. Formulation. *Acta Metallurgica et Materialia*, 42(10):3463–3479, October 1994. URL `http://www-mech.eng.cam.ac.uk/profiles/fleck/papers/61.pdf`.

[66] R. Talreja. Multi-scale modeling in damage mechanics of composite materials. *Journal of Materials Science*, 41(20):6800–6812, October 2006. doi:10.1007/s10853-006-0210-9.

[67] L. Mishnaevsky, Jr. and P. Brøndsted. Micromechanical modeling of damage and fracture of unidirectional fiber reinforced composites: A review. *Computational Materials Science*, 44: 1351–1359, 2009. doi:10.1015/j.commatsci.2008.09.004.

[68] L. Mishnaevsky, Jr. and P. Brøndsted. Micromechanisms of damage in unidirectional fiber reinforced composites: 3D computational analysis. *Composites Science and Technology*, 69: 1036–1044, 2009. doi:10.1016/j.compscitech.2009.01.022.

[69] F. V. Souza, D. H. Allen, and Y.-R. Kim. Multiscale model for predicting damage evolution in composites due to impact loading. *Composites Science and Technology*, 68:2624–2634, 2008. doi:10.1016/j.compscitech.2008.04.043.

[70] M. Sherburn. *Geometric and Mechanical Modelling of Textiles*. PhD thesis, University of Nottingham, July 2007. URL `http://etheses.nottingham.ac.uk/303/`.

[71] X. F. Wang, X. W. Wang, G. M. Zhou, and C. W. Zhou. Multi-scale analyses of 3D woven composite based on periodicity boundary conditions. *Journal of Composite Materials*, 41(14):1773–1788, July 2007. doi:10.1177/0021998306069891.

[72] O. O. Ochoa and J. N. Reddy. *Finite Element Analysis of Composite Laminates*. Kluwer Academic Publishers, 1992. ISBN 978-079231125-6.

[73] J. N. Reddy. *An introduction to the Finite Element Method*. McGraw-Hill, 1985. ISBN 978-007051355-6.

[74] J. N. Reddy. *Mechanics of Laminated Composite Plates and Shells: Theory and Analysis*. CRC Press, 2nd edition, 2003. ISBN 978-084931592-3.

[75] J. N. Reddy. *Mechanics of Laminated Composite Plates*. CRC Press, 1997. ISBN 978-084933101-5.

[76] J. N. Reddy. An evaluation of equivalent-single-layer and layerwise theories of composite laminates. *Composite Structures*, 25:21–35, 1993. doi:10.1016/0263-8223(93)90147-I.

[77] J. N. Reddy and D. H. Robbins, Jr. Theories and computational models for composite laminates. *Applied Mechanics Reviews*, 47(6):147–169, June 1994. doi:10.1115/1.3111076.

[78] D. H. Robbins, Jr. and J. N. Reddy. Modelling of thick composites using a layerwise laminate theory. *International Journal for Numerical Methods in Engineering*, 36(4):655–677, 1993. doi:10.1002/nme.1620360407.

[79] S. K. Kassegne. *Layerwise theory for discretely stiffened laminated cylindrical shells*. PhD thesis, Faculty of the Virginia Polytechnic Institute and State University, December 1992. URL `http://scholar.lib.vt.edu/theses/available/etd-07282008-134249/`.

[80] C. M. Dakshina Moorthy and J. N. Reddy. Modelling of laminates using a layerwise element with enhanced strains. *International Journal for Numerical Methods in Engineering*, 43(4):755–779, 1998. doi:10.1002/(SICI)1097-0207(19981030)43:4<755::AID-NME449>3.0.CO;2-N.

[81] E. Carrera and L. Demasi. Classical and advanced multilayered plate elements based upon PVD and RMVT. Part 1: Derivation of finite element matrices. *International Journal for Numerical Methods in Engineering*, 55(2):191–231, 2002. doi:10.1002/nme.492.

[82] E. Carrera and L. Demasi. Classical and advanced multilayered plate elements based upon PVD and RMVT. Part 2: Numerical implementations. *International Journal for Numerical Methods in Engineering*, 55(3):253–291, 2002. doi:10.1002/nme.493.

[83] H. Murakami. Laminated composite plate theory with improved in-plane responses. *Journal of Applied Mechanics*, 53(3):661–666, 1986. doi:10.1115/1.3171828.

[84] E. Carrera. Historical review of zig-zag theories for multilayered plates and shells. *Applied Mechanics Reviews*, 56(3):287–308, May 2003. doi:10.1115/1.1557614.

[85] E. Carrera. On the use of Murakami's zig-zag function in the modeling of layered plates and shells. *Computers and Structures*, 82:541–554, 2004. doi:10.1016/j.compstruc.2004.02.006.

[86] L. Demasi. Refined multilayered plate elements based on Murakami zig-zag functions. *Composite Structures*, 70:308–316, 2005. doi:10.1016/j.compstruct.2004.08.036.

[87] P. M. Mohite and C. S. Upadhyay. Region-by-region modeling of laminated composite plates. *Computers and Structures*, 85:1808–1827, 2007. doi:10.1016/j.compstruc.2007.04.005.

[88] K. Rohwer, S. Friedrichs, and C. Wehmeyer. Analyzing laminated structures from fibre-reinforced composite material—an assessment. *Technische Mechanik*, 25(1):59–79, 2005. URL `http://www.uni-magdeburg.de/ifme/zeitschrift_tm/2005_Heft1/rohwer.pdf`.

[89] E. Carrera. Evaluation of layerwise mixed theories for laminated plates analysis. *AIAA Journal*, 36(5):830–839, May 1998.

[90] R. de Borst and J. J. C. Remmers. Computational modelling of delamination. *Composites Science and Technology*, 66:713–722, 2006. doi:10.1016/j.compscitech.2004.12.025.

[91] T. E. Tay. Characterization and analysis of delamination fracture in composites: An overview of developments from 1990 to 2001. *Applied Mechanics Reviews*, 56(1):1–32, January 2003. doi:10.1115/1.1504848.

[92] G. Alfano and M. A. Crisfield. Finite element interface models for the delamination analysis of laminated composites: mechanical and computational issues. *International Journal for Numerical Methods in Engineering*, 50:1701–1736, 2001. doi:10.1002/nme.93.

[93] I. Scheider. Derivation of separation laws for cohesive models in the course of ductile fracture. *Engineering Fracture Mechanics*, 76:1450–1459, 2009. doi:10.1016/j.engfracmech.2008.12.006.

[94] H. S. Kim, A. Chattopadhyay, and A. Ghoshal. Characterization of delamination effect on composite laminates using a new generalized layerwise approach. *Computers and Structures*, 81 (15):1555–1566, July 2003. doi:10.1016/S0045-7949(03)00150-0.

[95] J. J. C. Remmers, G. N. Wells, and R. de Borst. A solid-like shell element allowing for arbitrary delaminations. *International Journal for Numerical Methods in Engineering*, 58(13):2013–2040, 2003. doi:10.1002/nme.907.

[96] G. N. Wells and L. J. Sluys. A new method for modelling cohesive cracks using finite elements. *International Journal for Numerical Methods in Engineering*, 50:2667–2682, 2001. doi:10.1002/nme.143.

[97] G. N. Wells, R. de Borst, and L. J. Sluys. A consistent geometrically non-linear approach for delamination. *International Journal for Numerical Methods in Engineering*, 54:1333–1355, 2002. doi:10.1002/nme.462.

[98] J. J. C. Remmers. *Discontinuities in materials and structures: A unifying computational approach*. PhD thesis, Technische Universiteit Delft, October 2006. URL `http://www.mate.tue.nl/mate/showabstract.php/8958`.

[99] R. de Borst, J. J. C. Remmers, and A. Needleman. Mesh-independent discrete numerical representaions of cohesive-zone models. *Engineering Fracture Mechanics*, 73:160–177, 2006. doi:10.1016/j.engfracmech.2005.05.007.

[100] J. J. C. Remmers, R. de Borst, and A. Needleman. The simulation of dynamic crack propagation using the cohesive segments method. *Journal of the Mechanics and Physics of Solids*, 56:70–92, 2008. doi:10.1016/j.jmps.2007.08.003.

[101] Y. Sun, Y. G. Hu, and K. M. Liew. A mesh-free simulation of cracking and failure using the cohesive segments method. *International Journal of Engineering Science*, 45:541–553, 2007. doi:10.1016/j.ijengsci.2007.03.004.

[102] T. O. Williams and F. L. Addessio. A general theory for laminated plates with delaminations. *International Journal of Solids and Structures*, 34(16):2003–2024, 1997. doi:10.1016/S0020-7683(96)00131-X.

[103] T. O. Williams and F. L. Addessio. A dynamic model for laminated plates with delaminations. *International Journal of Solids and Structures*, 35(1-2):83–106, 1998. doi:10.1016/S0020-7683(97)00055-3.

[104] T. O. Williams. A generalized multilength scale nonlinear composite plate theory with delamination. *International Journal of Solids and Structures*, 36:3015–3050, 1999. doi:10.1016/S0020-7683(98)00138-3.

[105] T. O. Williams and J. Aboudi. A generalized micromechanics model with shear coupling. *Acta Mechanica*, 138:131–154, 1999. doi:10.1007/BF01291840.

[106] T. O. Williams and J. Aboudi. A fully coupled thermo-mechanical micromechanics model. *Journal of Thermal Stresses*, 22:841–873, 1999. doi:10.1080/014957399280599.

[107] T. O. Williams. A new theoretical framework for the formulation of general, nonlinear, multiscale plate theories. *International Journal of Solids and Structures*, 45:2534–2560, 2008. doi:10.1016/j.ijsolstr.2007.12.006.

[108] P. P. Camanho and C. G. Dávila. Mixed-mode decohesion finite elements for the simulation of delamination in composite materials. Technical Report NASA/TM-2002-211737, NASA, Langley Research Center, June 2002. URL `http://ntrs.nasa.gov/archive/nasa/casi.ntrs.nasa.gov/20020053651_2002090610.pdf`.

[109] C. G. Dávila, P. P. Camanho, and A. Turon. Effective simulation of delamination in aeronautical structures using shells and cohesive elements. *Journal of Aircraft*, 45(2):663–672, Mar-Apr 2008. doi:10.2514/1.32832.

[110] C. G. Dávila, P. P. Camanho, and A. Turon. Cohesive elements for shells. Technical Report NASA/TP-2007-214869, NASA, Langley Research Center, April 2007. URL `http://ntrs.nasa.gov/archive/nasa/casi.ntrs.nasa.gov/20070018344_2007018901.pdf`.

[111] M. V. Cid Alfaro, A. S. J. Suiker, R. de Borst, and J. J. C. Remmers. Analysis of fracture and delamination in laminates using 3D numerical modelling. *Engineering Fracture Mechanics*, 76: 761–780, 2009. doi:10.1016/j.engfracmech.2008.09.002.

[112] M. L. Liu and J. Yu. Finite element modeling of delamination by layerwise shell element allowing for interlaminar displacements. *Composites Science and Technology*, 63(3-4):517–529, Feb-Mar 2003. doi:10.1016/S0266-3538(02)00218-X.

[113] F. Aymerich, F. Dore, and P. Priolo. Prediction of impact-induced delamination in cross-ply composite laminates using cohesive interface elements. *Composites Science and Technology*, 68: 2383–2390, 2008. doi:10.1016/j.compscitech.2007.06.015.

[114] M. Elices, G. V. Guinea, J. Gómez, and J. Planas. The cohesive zone model: advantages, limitations and challenges. *Engineering Fracture Mechanics*, 69(2):137–163, January 2002. doi:10.1016/S0013-7944(01)00083-2.

[115] Q. Yang and B. N. Cox. Cohesive models for damage evolution in laminated composites. *International Journal of Fracture*, 133:107–137, 2005. doi:10.1007/s10704-005-4729-6.

[116] M. Meo and E. Thieulot. Delamination modelling in a double cantilever beam. *Composite Structures*, 71(3-4):429–434, December 2005. doi:10.1016/j.compstruct.2005.09.026.

[117] A. Bensoussan, J.-L. Lions, and G. Papanicolaou. *Asymptotic analysis for periodic structures*. Studies in Mathematics and its Applications. North-Holland Publishing Company, Amsterdam, 1978. ISBN 978-044485172-7.

[118] J. Pinho da Cruz, J. A. Oliveira, and F. Teixeira-Dias. Asymptotic homogenisation in linear elasticity. Part I: Mathematical formulation and finite element modelling. *Computational Materials Science*, 45:1073–1080, 2009. doi:10.1016/j.commatsci.2009.02.025.

[119] A. L. Kalamkarov and A. V. Georgiades. Asymptotic homogenization models for smart composite plates with rapidly varying thickness: Part I – Theory. *International Journal for Multiscale Computational Engineering*, 2(1):133–148, 2004.

[120] A. V. Georgiades and A. L. Kalamkarov. Asymptotic homogenization models for smart composite plates with rapidly varying thickness: Part II – Applications. *International Journal for Multiscale Computational Engineering*, 2(1):149–172, 2004.

[121] V. G. Kouznetsova. *Computational homogenization for the multi-scale analysis of multi-phase materials*. PhD thesis, Technische Universiteit Eindhoven, Eindhoven, 2002.

[122] N. Takano and Y. Okuno. Three-scale finite element analysis of heterogeneous media by asymptotic homogenization and mesh superposition methods. *International Journal of Solids and Structures*, 41:4121–4135, 2004. doi:10.1016/j.ijsolstr.2004.02.049.

[123] N. Takano, M. Zako, and Y. Okuno. Multi-scale finite element analysis of porous materials and components by asymptotic homogenization theory and enhanced mesh superposition method. *Modelling and Simulation in Materials Science and Engineering*, 11:137–156, 2003.

[124] G. N. Praveen and J. N. Reddy. Transverse matrix cracks in cross-ply laminates: stress transfer, stiffness reduction and crack opening profiles. *Acta Mechanica*, 130:227–248, 1998. doi:10.1007/BF01184313.

[125] D. H. Robbins, Jr., J. N. Reddy, and F. Rostam-Abadi. Layerwise modeling of progressive damage in fiber-reinforces composite laminates. *International Journal of Mechanics and Materials in Design*, 2:165–182, 2005. doi:10.1007/s10999-006-9001-3.

[126] R. C. Pavan, G. J. Creus, and S. Maghous. A simplified approach to continuous damage of composite materials and micromechanical analysis. *Composite Structures*, 91:84–84, 2009. doi:10.1016/j.compstruct.2009.04.044.

[127] J. J. Skrzypek and A. Ganczarski. *Modeling of Material Damage and Failure of Structures*. Springer, Berlin, 1999. ISBN 978-354063725-7.

[128] J. Lemaitre and R. Desmorat. *Engineering Damage Mechanics*. Springer, Berlin, 2005. ISBN 978-354021503-5.

[129] D. H. Robbins, Jr., J. N. Reddy, and F. Rostam-Abadi. An efficient continuum damage model and its application to shear deformable laminated plates. *Mechanics of Advanced Materials and Structures*, 12:391–412, 2005. doi:10.1080/15376490500259202.

[130] P. P. Camanho and F. L. Matthews. A progressive damage model for mechanically fastened joints in composite laminates. *Journal of Composite Materials*, 33(24):2248–2280, 1999. doi:10.1177/002199839903302402.

[131] G. Z. Voyiadjis and T. Park. Anisotropic damage effect tensors for the symmetrization of the effective stress tensor. *Journal of Applied Mechanics*, 64:106–110, March 1997. doi:10.1115/1.2787259.

[132] E. J. Barbero, P. Lonetti, and K. K. Sikkil. Finite element continuum damage modeling of plain weave reinforced composites. *Composites: Part B*, 37:137–147, 2006. doi:10.1016/j.compositesb.2005.06.001.

[133] P. Maimí, P. P. Camanho, J. A. Mayugo, and C. G. Dávila. A continuum damage model for composite laminates: Part I – Constitutive model. *Mechanics of Materials*, 39(10):897–908, October 2007. doi:10.1016/j.mechmat.2007.03.005.

[134] P. Maimí, J. A. Mayugo, and P. P. Camanho. A three-dimensional damage model for transversely isotropic composite laminates. *Journal of Composite Materials*, 42(25):2717–2745, 2008. doi:10.1177/0021998308094965.

[135] Texgen.